THE DEVELOPMENT OF SUITABLE CYCLIC LOADING AND BOUNDARY CONDITIONS FOR BALLAST BOX TESTS

T.C.U. JIDEANI

THE DEVELOPMENT OF SUITABLE CYCLIC LOADING AND BOUNDARY CONDITIONS FOR BALLAST BOX TESTS

by

TIMOTHY CHIMNYERE UCHECHUKWU JIDEANI

A dissertation submitted in partial fulfilment of the requirements for the degree of

MASTER OF ENGINEERING (TRANSPORTATION ENGINEERING)

In the

Department of Civil Engineering

Faculty of Engineering, Built Environment and Information Technology

UNIVERSITY OF PRETORIA

May 2018

SUMMARY

THE DEVELOPMENT OF SUITABLE CYCLIC LOADING AND BOUNDARY CONDITIONS FOR BALLAST BOX TESTS

Timothy Chimnyere Uchechukwu Jideani

Supervisor: Professor P. J. Gräbe

Department: Civil Engineering

University: University of Pretoria

Degree: Master of Engineering (Transportation Engineering)

Laboratory tests on ballast give insight into the behaviour and performance of the ballast layer under passenger and heavy haul traffic. It is important, however, to ensure that the simulation of train loads on the ballast layer in the laboratory represents in situ loading conditions. With adequate, representative loading in the laboratory, the settlement, stiffness, modulus and overall performance of the ballast layer can be estimated and predicted in the future. However, a review of current laboratory tests on ballast reveals that these do not employ the approximate in situ loading conditions. Furthermore, adequate ballast confinement in laboratory tests should model the confinement along the track as this gives an indication of an ideal response of the ballast layer in situ as well as its impact on track structure deterioration.

The objective of this study was therefore to develop suitable cyclic loading and boundary conditions for ballast box tests in the laboratory which would represent similar conditions in the field. Literature studies reveal the typical train loading pattern at the rail seat (referred to as the Field loading (FL) pattern) which comprises of four load pulses with frequency depending on the wheel configuration. The FL pattern was compared with four alternative haversine loading patterns namely Laboratory Loading (Lab. L), Impulse Haversine Loading (IHL), Haversine Loading (HL) and Adjusted Haversine Loading (AHL) patterns. As a result of the complex shape of the FL pattern, a suitable alternative loading pattern was determined by comparing the rates of axial deformation caused by the FL pattern and an alternative loading pattern. It was found that the AHL pattern caused a similar rate of strain accumulation as the FL pattern. Furthermore, increasing the rest period interval between load cycles decreases the rate of ballast settlement.

Suitable boundary conditions for the ballast layer were assessed by varying the level of lateral confinement while monitoring the rate of strain accumulation and the degree of ballast breakage. A fully confined ballast layer (100 % lateral confinement) produced limited axial deformation and less ballast breakage in comparison to a ballast layer with no lateral confinement. Ballast settlement increased by 150 % when the lateral confinement in the ballast box tests were reduced from 100 % to 0%. The changes in vertical pressure at the base of the ballast layer were investigated at different levels of confinement. Average vertical pressures of ~4800 kPa was observed for 0 % laterally confined ballast, while average vertical pressures of ~3800 kPa was observed for a fully confined ballast layer.

The laboratory loading pattern developed in this research could provide accurate predictions of the long term behaviour of ballast as well as aiding the planning for subsequent ballast maintenance interventions based on realistic and accurate laboratory test results.

ACKNOWLEDGEMENT

Firstly, I thank God, my creator, for the physical and spiritual strength He gave me and His unfailing presence throughout the journey leading up to the completion of this dissertation. I am so thankful and blessed. I wish to express my sincere gratitude and appreciation to the following persons and organisations who made this dissertation possible:

a) My supervisor Prof. Hannes Gräbe for granting me this unique opportunity to further my studies and contribute to the Railway Engineering library; for your patience and understanding, for the exposure to the Railway Industry and for sharing your wealth of knowledge. I could not ask for a better supervisor.

b) Transnet Freight Rail for their financial support and assistance during this study.

c) The lecturers at the Civil Engineering department for taking interest and shedding more light on complex areas of this study.

d) The University of Pretoria for the use of laboratory facilities during the study.

e) The Civil Laboratory staff: Johan Scholtz and Daniel Motloung for their assistance during the study.

e) Lynda Araujo of Afrisam Aggregate for the ballast donation.

f) Aveng Infraset for the supply of railway sleepers for the experiments conducted in this study.

g) Rick Vandoorne for the crash course in Matlab and review of this dissertation.

h) Mario Schultz and Horacio Mones Ruiz for their constant moral support, motivation and helpful suggestions to see that this dissertation is a success.

i) To Mum and Dad for their prayers and motivation; my older brothers Josiah and Paul for their prayers and support during my Masters studies.

j) To the Deeper Life Campus Fellowship, University of Pretoria and its members for their support and spiritual counselling, motivation and encouragement during this study.

k) My best friend Deborah Jegede for her assistance while constructing the ballast box used in this study, for her prayers, motivation and support.

TABLE OF CONTENTS

LIST OF TABLES

LIST OF FIGURES

PAGE

1 INTRODUCTION

The increasing demand and supply of naturally occurring raw materials and other commodities from one geographical location to another continues to pose challenges on heavy haul railway lines and railway agencies. The structural integrity of heavy haul tracks determines the operation capacity required to transport these raw materials and other products. Factors that affect the structural integrity of heavy haul track include higher axle loads, variation in track stiffness due to differential settlement at different layers of the track, ballast fouling and degradation and inadequate lateral confinement of the ballast shoulder.

Laboratory tests on track components are conducted to investigate factors that affect the condition of the track structure in a short time frame. Furthermore, laboratory tests provide an avenue to assess factors that could improve the performance of railway lines. Laboratory ballast box tests provide various ballast layer responses which are used to predict the long term behaviour of track ballast subjected to train loading. However, simulated train loads and boundary conditions as used in laboratory tests on ballast material often do not correlate well with real train loading. It is therefore important to review current laboratory practices to ensure that reasonable and practical conclusions are drawn based on the long-term conditions of a railway track.

This study seeks to review current laboratory practices conducted on railway ballast. It seeks to provide suitable loading and boundary conditions for laboratory ballast box testing to represent field conditions.

1.1 OBJECTIVES OF THE STUDY

The objectives of this study were to develop suitable loading and boundary conditions for laboratory testing with the ballast box to accurately reflect field conditions. Further investigations conducted under each objective are outlined as follows:

1. Development of a suitable alternative loading pattern in the laboratory to reproduce an approximate rate of ballast strain accumulation as experienced in the field. This was done by studying different haversine loading patterns.
    - Analyse the modulus of the ballast layer under the different haversine loading patterns.
    - Investigate the effect of rest periods between load cycles on the permanent settlement of the ballast layer.

2. Develop suitable boundary conditions using ballast box tests by varying the level of lateral confinement of the ballast layer.
    - Investigate the effect of varying levels of lateral confinement on the permanent strain and breakage of the ballast layer.
    - Investigate the effect of varying levels of lateral confinement on the vertical stress at the bottom of the ballast layer.

1.2 SCOPE OF THE STUDY

This experiment simulated the region below the rail seat using a small box test as well as a half full-scale test considering a portion of a heavy haul track consisting of half a sleeper and the ballast shoulder. The test box for the full-scale test was adjustable to account for changes in boundary conditions. It also followed the track design requirements specified by Transnet, South Africa. Only the ballast layer was considered in this experiment. The loading conditions were based on heavy haul railway lines.

To develop a suitable loading pattern for laboratory box tests, four ballast samples were subjected to 500 000 cycles of alternating loading patterns. Properties of each loading pattern and their influence on ballast axial strain, stiffness and modulus were examined.

To develop suitable boundary conditions for laboratory box tests, the developed loading pattern was used to assess the axial strain and breakage of ballast particles with varying levels of confinement. Furthermore, the vertical stress at the base of the 300 mm ballast layer was assessed for varying levels of lateral confinement.

1.3 METHODOLOGY

The methodology followed is described below:

Suitable Loading Pattern

The typical loading pattern of ballast in situ was assessed from literature. This loading pattern, termed as the Field Loading (FL) pattern in this study, served as a control to compare the four alternative loading patterns. Four ballast samples were used, each subjected to 500 000 load cycles of alternating loading patterns of Field Loading and an alternative loading pattern. The rates of strain accumulation from both loading patterns were compared for each sample. The loading pattern which produced a strain rate closest to the Field Loading was identified as the suitable loading pattern.

Suitable Boundary Conditions

The suitable loading pattern was used to investigate the effects of varying levels of lateral confinement on ballast permanent strain and breakage. Five levels of lateral confinement were used for this experiment namely 100 %, 75 %, 50 %, 25 % and 0 % lateral confinements. Each ballast sample was compacted at 100 % lateral confinement, after which a portion of the ballast shoulder was added depending on the level of confinement required. To quantify the degree of ballast breakage, ballast particles were painted and placed at 100 mm and 300 mm depths of the ballast layer. Sieve analysis and weight measurements were performed before and after testing for each level of lateral confinement. Each ballast sample was subjected to 325 000 load cycles.

1.4 ORGANISATION OF THE REPORT

This dissertation consists of the following chapters:

- Chapter 1 discusses the importance, the scope and methodology of this study.
- Chapter 2 contains a literature study explaining track loading, ballast layer performance and factors affecting ballast layer behaviour as well as previous ballast box tests conducted in the laboratory.
- Chapter 3 describes the test materials and equipment used for the experiment.
- Chapter 4 presents the results. Further analysis and discussion of results and validation are also outlined in this chapter.
- Chapter 5 provides a summary of results, the conclusions drawn from the study and recommendations for future studies.
- A list of references is included at the end of this dissertation.

2 LITERATURE REVIEW

A synopsis of different railway track structures and their components will be discussed briefly in this chapter.

This chapter will focus mainly on previous literature studies and research on some key aspects relating to heavy haul (ballasted) railway track structures. These aspects include track loading conditions, load and stress distribution, deformation of the ballast layer and particle breakage.

Laboratory loading patterns and the effect of load rest periods on ballast permanent deformation are reviewed from previous research. Furthermore, material properties and requirements such as gradation, compaction, appropriate densities and moisture content for individual track layers will be highlighted.

2.1 TRACK STRUCTURE

Railway track structures are divided into two types: ballasted and ballastless track. Recent literature on railway tracks show that ballastless track could be more economical than ballasted track. This is the case when their life cycle cost and the extent of traffic disruption during maintenance, are taken into consideration.

2.1.1 Ballasted Track

Ballasted track, also called conventional track or 'classical track' is divided into the track superstructure and the track substructure. The track superstructure consists of a system of components supported by the ballast. These components include the rail, resilient rail pads, the sleeper and the fastening system. These components support train loads by decreasing the high concentrated stresses at the wheel-rail interface to a level bearable for the track substructure layers. The track substructure consists of the ballast, subballast and subgrade which collectively serve as a foundation to support the track superstructure. Figure 2-1 shows the components that constitute a ballasted track structure. The track superstructure is separated from the track substructure by the sleeper-ballast interface.

Rails are longitudinal high-strength steel members that guide and support the passing train wheels. The stiffness of rails must provide enough support to transfer concentrated train loads without excessive deflection between sleepers (Selig and Waters, 1994). Improvements in the connection of steel rail sections by using continuous welded rails (CWR) have resulted in significant savings through reduced maintenance costs, improved riding quality, reduced wear

on rolling stock and limited damage of the substructure; as opposed to rail connections using fish-plated joints or bolted joints. The discontinuity of bolted rail joints causes additional dynamic impact loads and vibrations which damage rail joints. Other functions of the rail highlighted by Esveld (2001) include its ability to conduct electricity and signal currents as well as distributing acceleration and braking forces by means of adhesion.

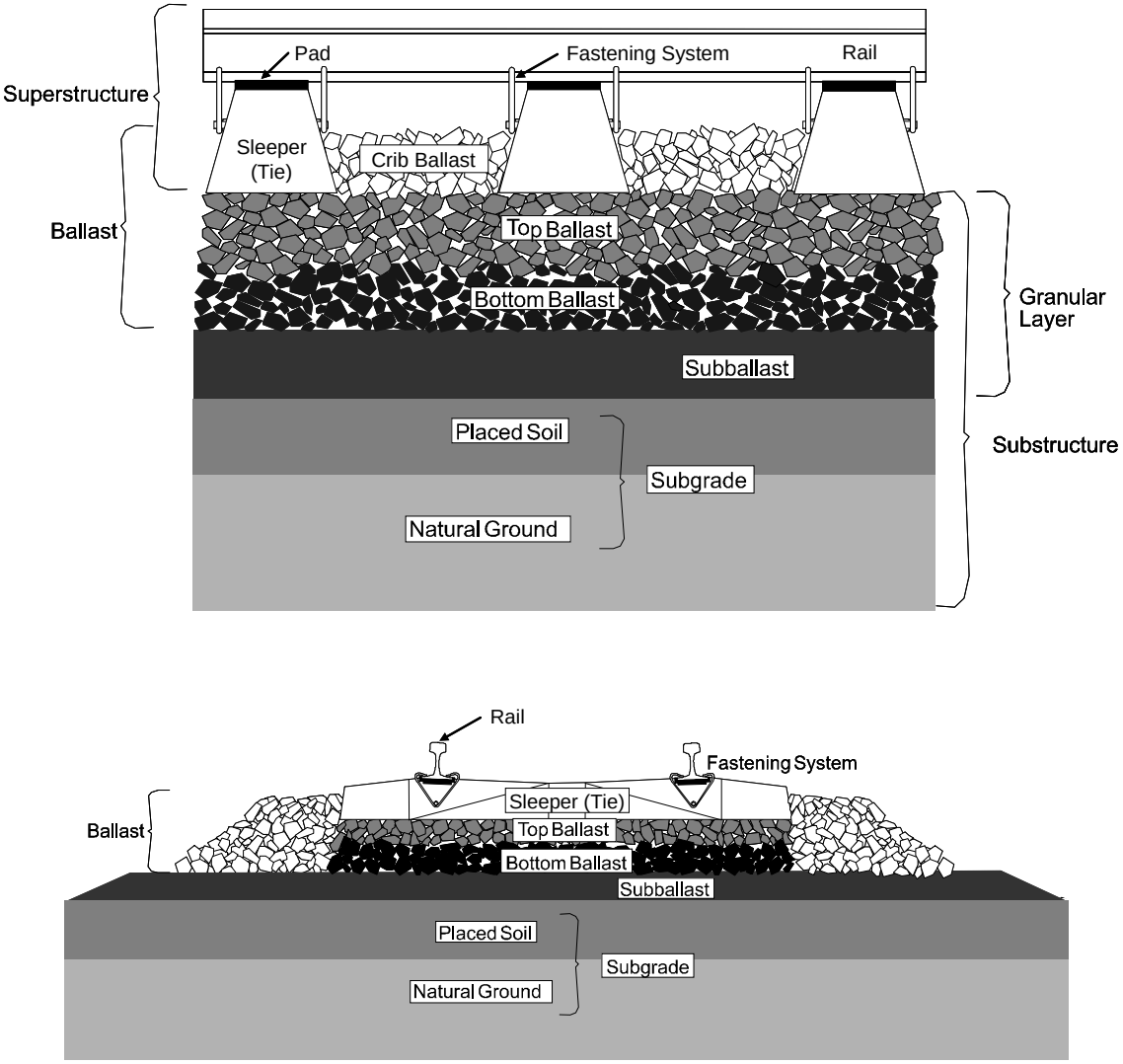

Figure 2-1: Ballasted track structure and associated components (Selig and Waters 1994)

The purpose of the fastening system is to retain the rails against the sleepers and to resist vertical, lateral, longitudinal and overturning moments of the rail. The connections between the sleeper and the rails have disparities as the choice of the fastening system depends on the properties and structure of the sleeper. Rail pads, placed at the rail-sleeper interface, are responsible for the insulation of sleepers against electrical current. Most heavy haul lines in South Africa use

elastic fasteners (Figure 2-2), such as Fist or Pandrol fasteners, which are suitable for concrete sleepers. For wooden/timber sleepers, steel plate and cut spike fasteners are commonly used.

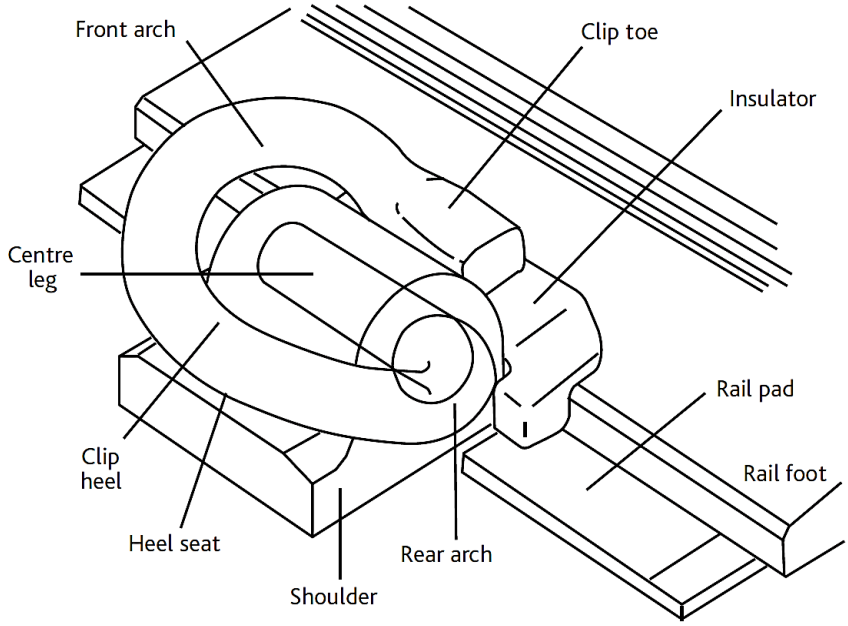

Figure 2-2: Components of a Pandrol 'e' series clip (Infraset 2009)

Sleepers serve as a support for the rails and fastening system. They can be made from timber, concrete, steel and in limited cases from composites or plastic. Wooden sleepers are mostly common in the United States, often because of lower cost compared to other sleeper types, and their resilient behaviour (Li et al., 2015). However, wooden sleepers are susceptible to rot and decay which tend to inhibit proper drainage. Most heavy haul lines use concrete sleepers which provide a much stiffer and secure fastening system. Esveld (2001) states specific advantages of concrete sleepers such as:

- Heavy weight (200 – 300 kg) - useful in connection with stability of CWR track
- Long service life - if fastenings are good or can be replaced easily
- High freedom of design and construction
- Relatively simple to manufacture

Some disadvantages of concrete sleepers include:

- Less elastic and resilient than wood
- Susceptible to corrugation and poor quality welds
- Risk of damage from impacts
- Dynamic loads and ballast stresses can be up to 25 % or more

Steel sleepers are expensive compared to other sleeper types and are only used in special conditions. A greener concept of manufacturing sleepers has led some companies to offer sleepers made of recycled plastic material. Plastic sleepers are suitable in harsh climate conditions and are environmentally friendly. Due to their imperviousness, they have an extended service life compared to wooden sleepers. Like wooden sleepers, recycled plastic sleepers exhibit properties such as damping of impact loads, lateral stability and sound absorption. However, plastic sleepers have gained limited acceptance due to the speed of mass production of stronger concrete sleepers (Indraratna et al., 2011).

Ballast forms the top layer of the track substructure. The sleepers are embedded in the ballast (referred to as boxing – a term used to describe the behaviour of the shoulder and crib ballast). Good ballast materials are angular, crushed hard stones and rocks, uniformly graded, free of dust and dirt, and not liable to cementing action. The most important functions of ballast include (Li et al., 2015):

- Supporting the rail-fastener-sleeper track panel by providing adequate vertical, lateral, and longitudinal resistance
- Transmitting train loads to the foundation
- Facilitating surface and lining operations (i.e. adjusting the track geometry)
- Providing immediate drainage of water
- Providing resilience and damping of dynamic wheel-rail forces

The general performance of ballast under train loading is characterised by the physical properties of individual ballast materials. These physical properties include particle size, shape, angularity, hardness, surface texture and durability. In addition, to fulfil the ballast functions, there must be adequate ballast layer thickness, proper particle size and gradation.

The subballast layer is located between the ballast and the subgrade. It acts as a separation layer by preventing interpenetration of subgrade and ballast. It sheds water and permits drainage of water from the ballast and subgrade respectively. Subballast materials comprise of broadly-graded gravel and sand, and are durable to satisfy the filter/separation requirements for ballast and subgrade. Other materials exist that can provide similar subballast functions, e.g. cement, lime, asphalt concrete layers and geosynthetic materials such as geomembranes, geogrids and geotextiles (filter fabrics).

The subgrade (or formation) is the platform on which the track structure is placed. It may consist of either soil or rock. Its main function is to provide a uniform, adequate and stable foundation for the subballast and ballast layers. Occasionally, the subgrade may be divided into two categories; namely natural ground (formation) and placed soil (fill) especially when replacement of an unsuitable existing soil layer is required and/or to raise the subgrade level to the required

elevation. Requirements of the subgrade include sufficient bearing capacity, reasonable settlement behaviour and providing adequate drainage of rain and ground water (Esveld 2001).

The main advantages of ballasted track are (Indraratna et al., 2011):

- Relatively low construction cost and use of indigenous construction materials
- Ease of maintenance works
- High hydraulic conductivity (drainage) of the track structure
- Simplicity in design and construction
- Good elasticity and good damping of noise

Notable disadvantages of ballasted track also stated by Indraratna et al. (2011) are:

- Degradation and fouling of ballast requires frequent track maintenance and routine checks
- Disruption of traffic during the maintenance operation
- Reduction in drainage capabilities due to the clogging of voids by crushed particles and infiltrating fines from the ballast and subgrade respectively
- Pumping of subgrade clay- and silt-size particles
- A ballasted track structure is generally thicker and heavier than a ballastless structure, which requires a stronger and larger foundation in cases of viaducts and bridges (Michas 2012; Esveld 2001).

2.1.2 Ballastless Track

There are several reasons for the deviation from the conventional track design to alternative track designs. One reason is the low cost of maintenance (up to 20 % to 30 % of the maintenance cost of ballasted track) owing to the absence of ballast deterioration, increased service life and reduced structural height and weight. Ballastless or slab track is mostly used for high-speed lines and light rail structures (such as trams). It uses concrete, gravel or asphalt support in place of the standard ballasted support.

Esveld (2001) outlined two different approaches of slab superstructure design; these are discrete rail support and continuous rail support. Slab track systems vary in stiffness. The choice of track stiffness (low or high flexural) totally depends on the bearing capacity and stiffness of the soil. For soft soils, which deform easily under pressure, a high flexural slab system is suitable to act as a bridge across weak spots and local deformations in the track bed.

2.2 TRACK LOADING

The design of a resilient railway track considers the wheel load and load transmission through the track structure as essential parameters which must be understood and quantified. Loads on a rail track are unevenly distributed and are divided into static and dynamic loads.

2.2.1 Static Loading

Static loading on a railway track is divided into two components: 1) live load, which is the train weight and 2) dead load, which represents the weight of the track components, layers and the subgrade. The dominant component of the static load is the train weight (equally distributed to each wheel). Esveld (2001) refers to static loads as quasi-static. Quasi-static loads take into account the static wheel load, the increase in wheel load on the outer rail in curves due to centrifugal force and the increase in wheel load due to wind (Equation 1).

$$F_{quasi-static} = F_{static} + F_{centrifugal} + F_{wind} \quad (1)$$

where F_{static} = static wheel load

$F_{centrifugal}$ = increase in wheel load on outer rail in curves due to non-compensated centrifugal force

F_{wind} = increase in wheel load due to cross winds

The design of the track foundation is commonly based on train axle load and wheel spacing, especially for heavy haul freight trains which generate significant stresses in the track structure. Table 2-1 shows the particulars of heavy haul freight trains around the world. The length of a train (number of wagons) and frequency of trains are important aspects of train loading required for determining the cumulative effect of cyclic loading on a track structure and its performance.

Table 2-1: Typical heavy haul freight trains around the world (modified from Li et al., 2015)

Country	Axle load (tonnes)	Train length (number of wagons)
South Africa	26 – 36	200 –342
United States and Canada	33	130 – 140
Australia	35 – 40	200 – 240
Brazil	27.5 – 32.5	330
Sweden	30	68
China	25 – 27	210

2.2.2 Dynamic Loading

Dynamic loads occur as either short duration forces or long duration forces. Short duration forces are typically high frequency impact loads arising from wheel discontinuities (such as flat wheels or out of round wheels) or rail discontinuities (such as dipped joints, rail corrugations and misaligned joints). Long duration forces are produced by track geometry irregularities possibly due to stiffness variations in the track substructure.

The dynamic load component of a wheel is roughly estimated by multiplying the static wheel load with a dynamic amplification factor (also known as dynamic impact factor - DIF) (Esveld, 2001). Jeffs and Tew (1991) listed major factors that affect the magnitude of dynamic loads, which are:

- Speed of train
- Static wheel load and wheel diameter
- Vehicle unsprung mass and vehicle condition
- Track condition (e.g. track joints, track geometry and track modulus)
- Track construction aspects and properties of ballast and subballast

Empirical formulae exist for determining the design vertical dynamic wheel load and are used by different railway organisations. Transnet Freight Rail in South Africa employs the Eisenmann's approach to determine the magnitude of the impact factor. Eisenmann (1972) suggested that the rail bending stress and deflection are normally distributed, and the mean values can be calculated from the beam on elastic foundation (BOEF) model. This normal distribution is illustrated in Figure 2-3 for both rail stress and rail deflection values.

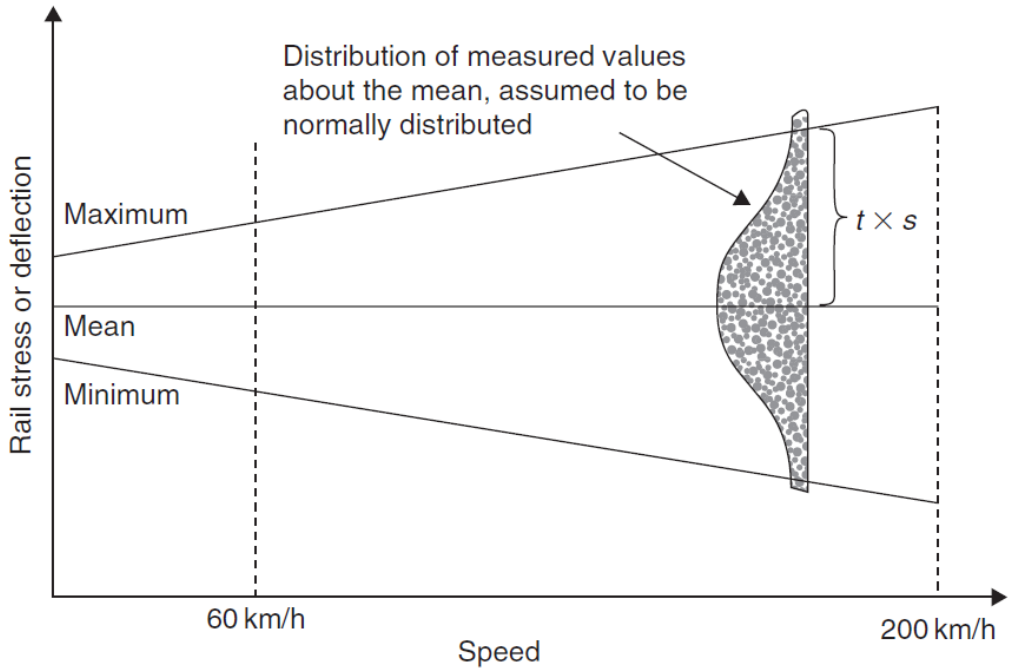

Figure 2-3: Normal distribution of rail bending stress and deflection with speed effect (adopted from Indraratna et al. 2011)

The mean rail stress ($\bar{x}$) and its corresponding standard deviation (s) can be expressed as:

$$s = \bar{x}\delta\eta \tag{2}$$

where δ = track condition factor, and η = vehicle speed factor

The value of δ is determined based on the track quality, with values 0.1, 0.2 and 0.3 representing a very good track, good track and a poor track condition respectively.

The value of η is based on the vehicle speed, V (km/h), with $\eta = 1$ for a vehicle speed less than 60 km/h. For a vehicle speed between 60 and 200 km/h, Equation 3 is suggested to calculate the η value:

$$\eta = \left(1 + \frac{V - 60}{140}\right) \tag{3}$$

The product of δ and η is referred to as the coefficient of variation. The corresponding maximum applied load (or rail deflection) is given by:

$$X = \bar{x} + st \tag{4}$$

where X = maximum applied load or deflection, and t = value depending on the upper confidence limits (UCL) which define the probability that the maximum applied load will not be exceeded, with values ranging from 0 to 3.

Considering the assumed linearity between the applied load and rail stress, the maximum rail stress (or rail deflection), X can be defined by the simple relationship:

$$X = \varphi \bar{x} \tag{5}$$

Combining Equation 2 and 4 and comparing with Equation 5, the dynamic impact factor (φ) is expressed as:

$$\varphi = 1 + \delta \eta t \tag{6}$$

Other methods for determining the dynamic impact factor (DIF) are shown in Table 2-2 below. The envelope defined by Eisenmann's curve of impact factor for good and very good track conditions incorporates both the American Railway Engineering and Maintenance-of-Way Association (AREMA) and the Office of Research and Experiments (ORE) impact factor curves that have been derived for average track conditions. Consequently, Eisenmann's dynamic impact factor is more reliable as it takes into account more track parameters. However, the use of this formula in practice is only reliable when the parameters are accurately known (Sadeghi, 2008). Hence, more simplified equations used in America - AREMA (2006), South Africa - Fröhling (1995), etc. which consider only train speed and/or wheel diameter are used to determine the dynamic impact factor as shown in Figure 2-4. Typical impact factors for heavy haul freight lines range from 1 to 1.9 depending on the track condition and confidence limit.

2.2.3 Cyclic Loading

Cyclic loading, from a railway viewpoint, is characterised by the shape, duration, magnitude of loading pulse, time interval between consecutive pulses (a reflection of wheel spacing) and the total number of load pulses. Further characterisation of cyclic (or repeated) loading can be done by conducting cyclic loading tests (using an hydraulic actuator or triaxial apparatus) in the laboratory to evaluate material properties and quantify the track structure performance (Li et al., 2015).

Powrie et al. (2007) and Li et al. (2015) suggest that, to determine the number of cyclic loading applications for a laboratory test, a common practice is to assume that two axle loads from a bogie are considered to produce one load cycle for the ballast layer and four axles from two bogies are considered to produce a single load cycle for the subgrade layer. Powrie et al. (2007) concluded that both magnitude and the number of load cycles during train passage reduce with depth. Equation 7 presented by Selig and Waters (1994) provides a conversion factor to convert the number of load cycles to gross tonnage.

Table 2-2: Equations for Dynamic Impact Factor (modified from Sadeghi 2008)

Standard	Equation
AREMA (2006)	$\varphi = 1 + \frac{5.21V}{D}$
Eisenmann (1970)	$\varphi = 1 + \delta\eta t$
ORE (1987), UIC (2004a)	$\varphi = 1 + \alpha' + \beta' + \gamma'$
DB (Doyle 1980), German	$\varphi = 1 + \frac{V^2}{30000}, \quad \varphi = 1 + \frac{4.5V^2}{10^5} - \frac{1.5V^3}{10^7}$
BR (Fredrick and Newton 1977), British	$\varphi = \frac{8.784(\alpha_1 + \alpha_2)V}{P_s}\left[\frac{D_j P_u}{g}\right]^{1/2}$
India (Saxena and Arora 2004)	$\varphi = 1 + \frac{V}{58.14\,k^{0.5}}$
South Africa (Fröhling 1995)	$\varphi = 1 + \frac{1.492V}{D}$
Clarke (1957)	$\varphi = 1 + \frac{19.65V}{(DK^{1/2})}$
WMATA (Doyle 1980), Washington	$\varphi = (1 + 3.86 \times 10^{-5}\,V^2)^{0.67}$
Sadeghi (Sadeghi and Yoldashkhan 2005, Sadeghi 2008), Iranian	$\varphi = -3.6(10^{-11})V^4 + 3.6(10^{-8})V^3 - 6(10^{-6})V^2 + 6(10^{-4})V + 1.2\,, \quad \varphi = 1 + \frac{4.73V}{D}$

NB: UIC, Union Internationale des Chemins de Fer; DB, German Railway Research; BR, British Railway Research; WMATA, Washington Metropolitan Area Transit Authority; V, velocity of train (km/h); D, diameter of the wheel (mm); δ, factor dependent upon the track quality; η, vehicle speed factor; t, factor related to the chosen upper confidence limits (UCL); α' and β' relate to mean value of the impact factor and γ' to the standard deviation of the impact factor; $(\alpha_1 + \alpha_2)$, total rail joint dip angle (radian); P_s, static wheel load; D_j, track stiffness at the joints (kN/mm); P_u, unsprung weight at one wheel (kN); g, the gauge width (mm); k, track modulus (MPa); K, modulus of the rail support system (MPa).

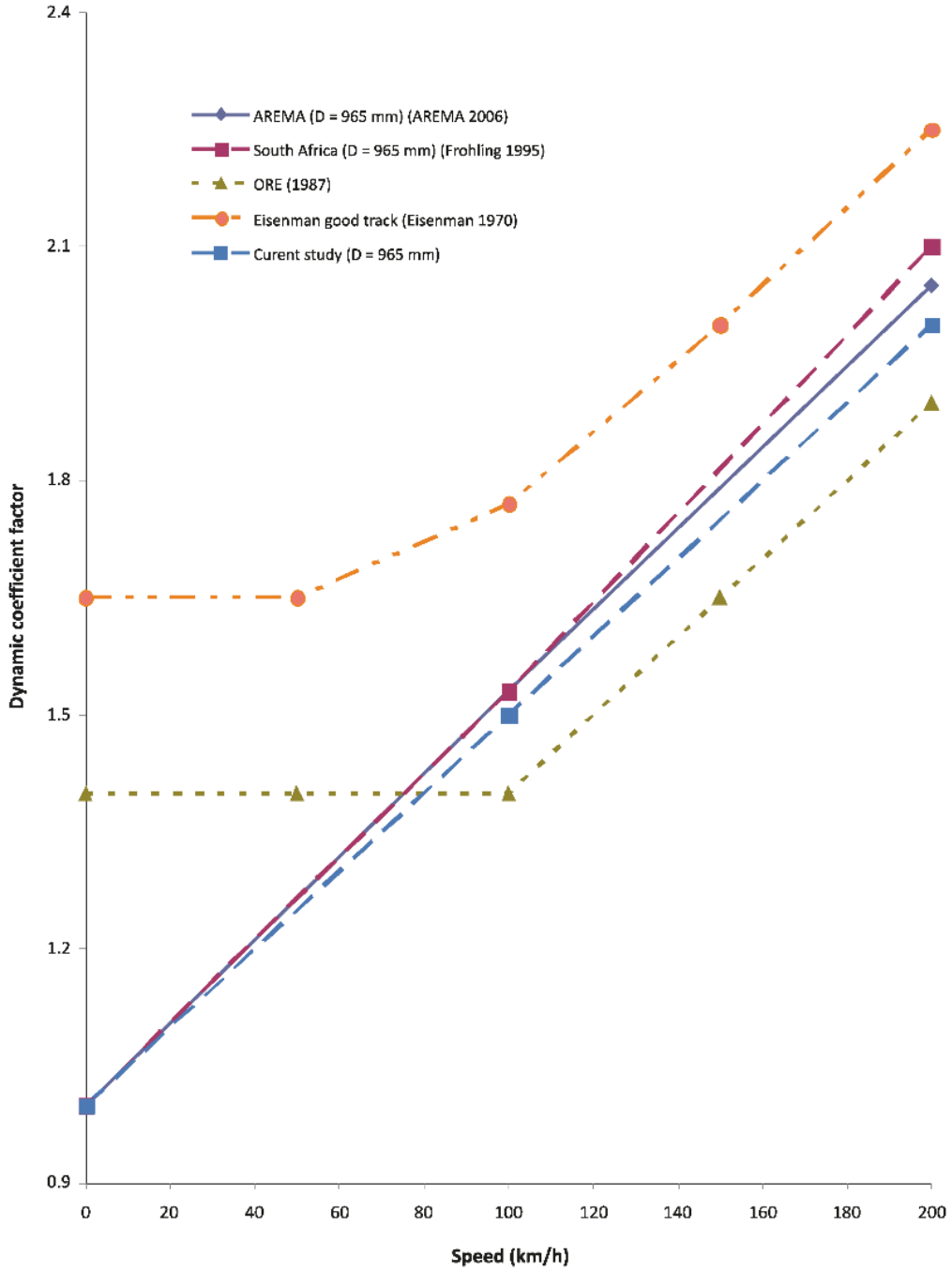

Figure 2-4: Graphical comparison of DIF from different methods and standards (Sadeghi 2008)

$$C_m = \frac{10^6}{A_t N_a} \tag{7}$$

where C_m is the number of load cycles per million gross tonne (MGT); A_t is the axle load in tonnes, and N_a is the number of axles per load cycle.

However, the above practice and equations vary depending on the coupler/axle spacing of the train under consideration. Axle spacing and bogie length affect the deflection and influence

depth (in terms of stresses) of a track structure. As the distance between two bogies increases, the total deflection of the track decreases due to the absence of overlapping stress influence lines induced by the wheel loads on the track (Li et al., 2015).

Cyclic loads are characterised by the shape and the duration of load pulses applied to the material under consideration. Two types of load (or stress) pulses are used in a cyclic loading tests. They are the haversine pulse and the trapezoidal pulse. Figure 2-5 shows a haversine loading function. Huang (1993) pointed out that the type and duration of cyclic loading should simulate the actual occurring loading pattern in the field and recommended the use of a stress pulse in the form of haversine or triangular loading. A study by Li (1994) suggested that the loading pulse by a single axle can be approximately represented by a haversine pulse for a track structure. However, for two axles under the same wagon or four axles under two adjacent wagons, the loading pulse shape is similar to a trapezoidal pulse.

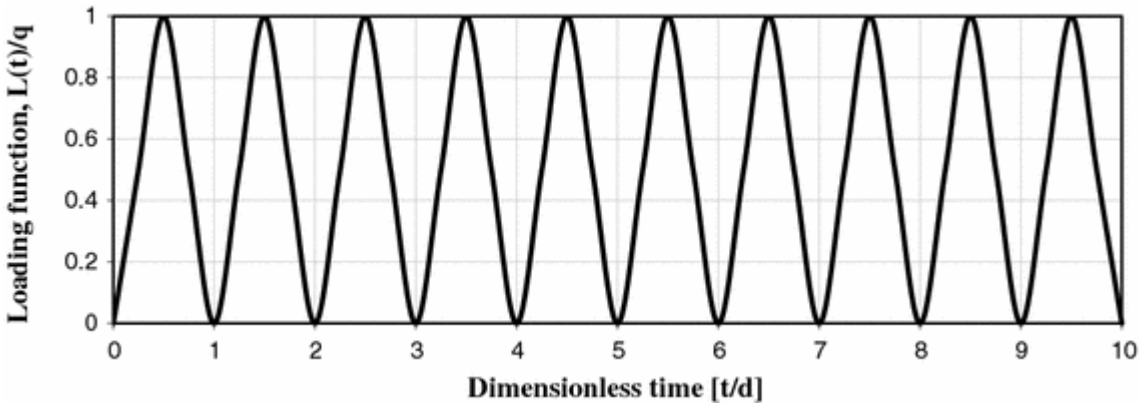

Figure 2-5: Haversine loading function (Huang 1993)

2.2.4 Load and Stress Pulse

The magnitude as well as the shape of load and stress pulses on a railway track depend on the track component conditions, geometry of the train (such as the wheel spacing per bogie, bogie pair spacing) and axle load. Figure 2-6 shows a load pulse of a bogie obtained from a load cell installed on the rail seat of a concrete sleeper during a field investigation by Zakeri and Sadeghi (2007), Sadeghi (2008) and Sadeghi and Shoja (2012). The geometry of the passing freight train consisted of 1800 mm wheel spacing per bogie and 920 mm wheel diameter.

Powrie et al. (2007) investigated the stress changes in the ground below a ballasted railway track during train passage using ABAQUS and concluded that the stress changes, in response to individual axle loads, decrease with depth. Yang et al. (2009) also conducted a study to investigate the vertical dynamic stress changes in the subballast layer and the subgrade during

the passage of a three-wagon freight train, by means of a 2-dimensional dynamic finite-element analysis. It was concluded that the passing of each axle is apparent in the subballast layer, while the effect of each adjoining pair of bogies are evident on the surface of the natural ground.

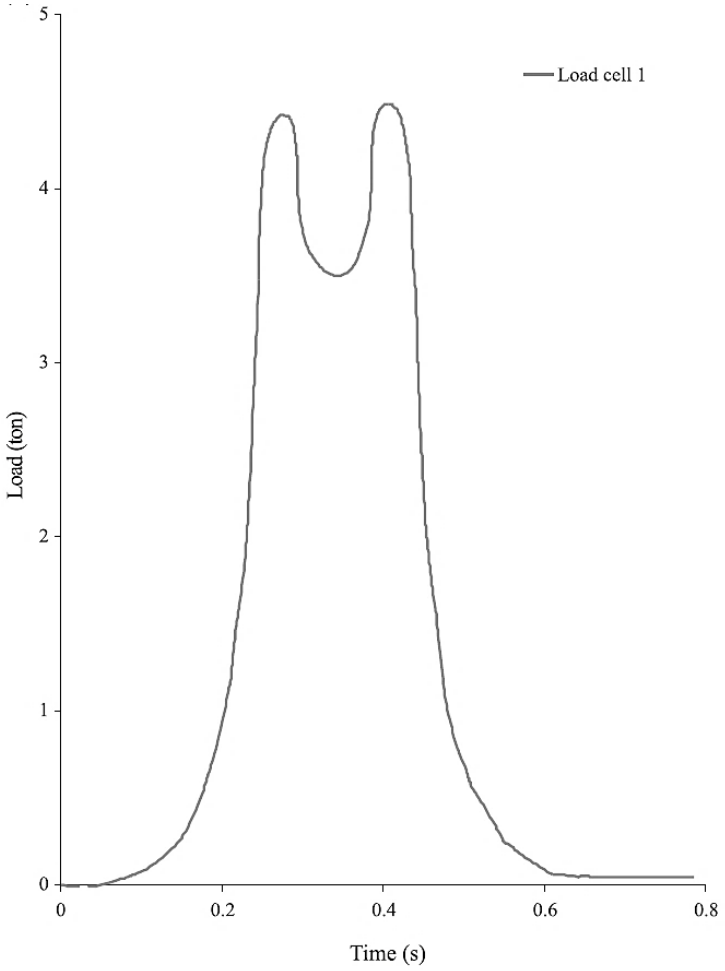

Figure 2-6: Measurements from a load cell embedded in a sleeper at the rail seat (Sadeghi 2008)

Field measurements of vertical dynamic stresses induced by axle loads were measured by Gräbe et al. (2005). Five in-situ total stress (pressure) cells were placed on top of each layer (the subballast layer being the first), at the centre of the track. Figure 2-7 (a) and (b) show the position of the in-situ pressure cells and the plotted stress (or pressure) data at each layer induced by 4-axle loads from 2 wagons respectively. The stress pulses in Figure 2-7 (b) agree with the conclusions made by several researchers regarding the shape or waveform of load and stress pulses. The load and stress pulse on subgrade layers can be represented by a single trapezoidal or haversine wave consisting of 4-axle loads (depending on the train configuration) due to the less prominent influence of axle loads with depth.

(a)

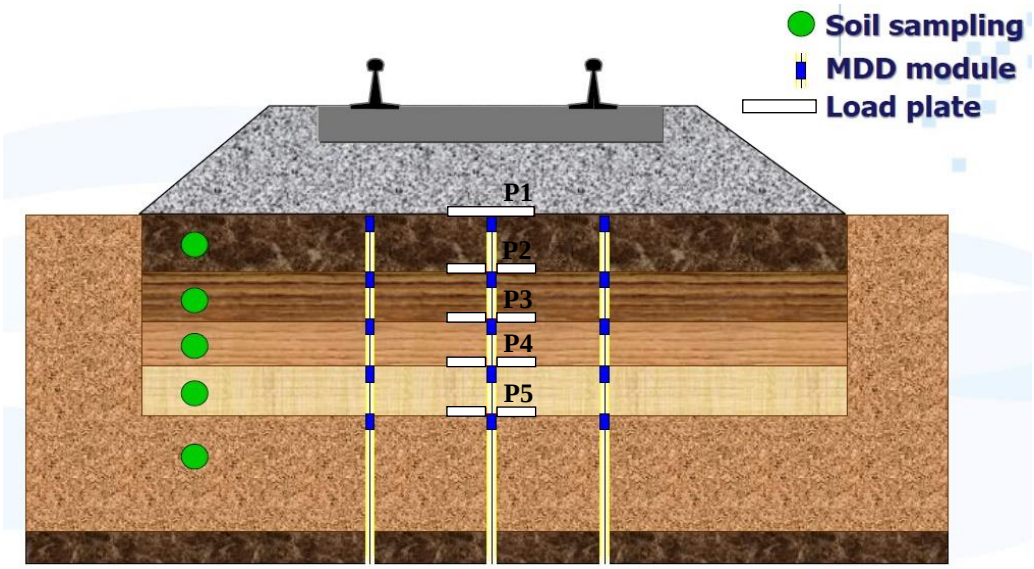

(b)

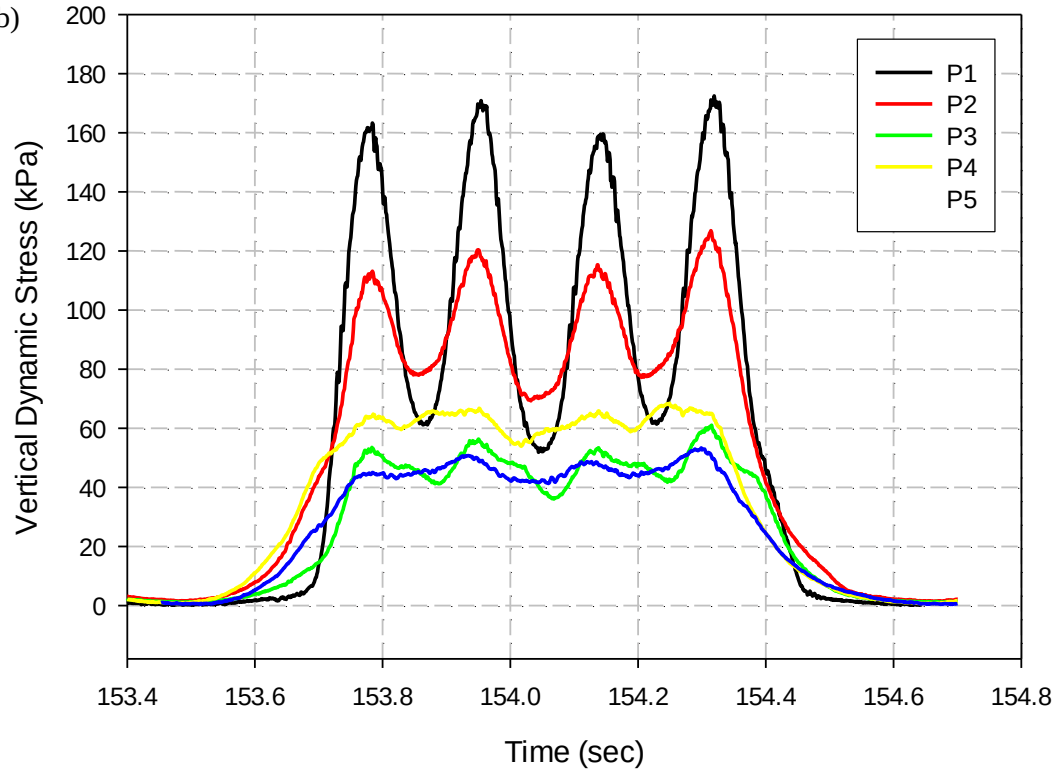

Figure 2-7: (a) Position of in-situ pressure cells and (b) vertical stress plots at each layer of the track substructure (modified from Gräbe et al. 2005)

It can therefore be concluded haversine or sinusoidal loading patterns are appropriate for subgrade tests in the laboratory (Li and Selig, 1996; Liu and Xiao, 2010; Priest et al., 2010; Li et al., 2015; Razouki and Schanz, 2011).

2.2.5 Loading Frequency, Rest Periods and Amplitude

According to Li et al. (2015), the effect of the loading frequency (i.e. the rate of loading) on the strength and stiffness properties of granular materials (ballast and subballast) is minimal, unless the granular materials are saturated and under undrained conditions. The consideration of loading rate effects is generally meaningful for subgrade soils only. Frequency of loading is dependent on the train speed. Typical loading frequency of traffic on the track is normally 8 Hz - 10 Hz (depending on the specified design speed of the railway line and the axle wheel spacing) according to Aursudkij et al. (2009). Several studies have been conducted to investigate the effect of the frequency of loading on ballast behaviour. Shenton (1978) carried out cyclic loading tests with varying frequencies from 0.1 Hz to 30 Hz while the confining pressure and load amplitude were constant. Shenton concluded that the frequency of loading does not significantly affect the deformation behaviour of ballast. Sun et al. (2014) conducted cyclic triaxial tests to investigate the effect of loading frequency on particle breakage and volumetric strain of latite basalt aggregates (Figure 2-8). As observed from Figure 2-8, as the load frequency increases, the particle breakage and volumetric strain of ballast increases. This leads to rearrangement of ballast particles and further permanent deformation. Yang et al. (2009) and Powrie & Priest (2011) assessed the effects of train speed on the load-deformation response of a track foundation using finite element analyses and field measurements. It was concluded that the stress and deflection of each layer increase as train speed increases.

Rest periods in field train loading is a function of axle wheel spacing and train speed (loading frequency). At a constant speed, the rest period for a wider wheel spacing will be greater than the rest period of a narrow wheel spacing. Furthermore, considering a fixed wheel spacing, the rest period for a train moving at low speed will be greater than the rest period of a fast-moving train. The fixed wheel spacing is a common scenario employed in laboratory ballast tests. Qian et al. (2011) concluded that rest time between dynamic load pulses had a major influence on ballast settlement.

Although heavy haul trains often operate at low frequencies (train speeds, $V \leq 80$ km/h), the wheel loads still have a significant effect on particle breakage as well as volumetric strain. Hence, the effect of loading amplitude has been studied. Stewart (1986) and Selig and Waters (1994) performed a series of tests where the load amplitude was varied to investigate the effect on ballast deformation. Ballast permanent strain increases significantly with an increase in load

amplitude. However, at low cyclic stress levels, the rate of plastic deformation of ballast is negligible (i.e. the response of ballast below this stress level becomes almost elastic, known as 'shakedown') (Suiker, 2002).

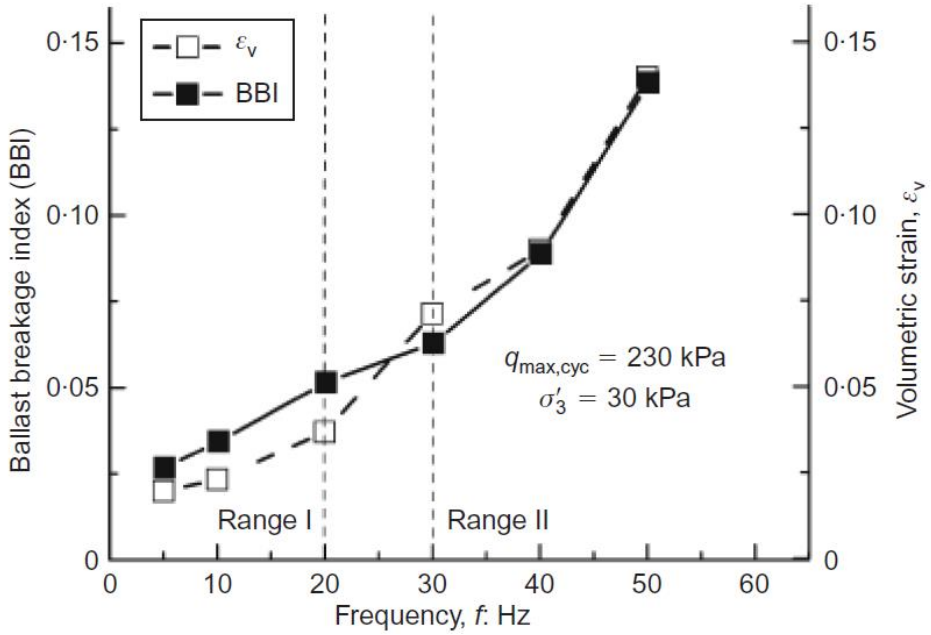

Figure 2-8: Breakage and volumetric strain behaviour of ballast as a function of loading frequency after 500 000 cycles (Sun et al., 2014)

Although a continuous haversine (or sinusoidal) load pulse is commonly applied in cyclic triaxial and box tests, according to Huang et al. (2009), the actual dynamic loading may have different loading patterns of varying pulse shapes with rest periods (according to the wheel spacing, car length and train speed) which may directly affect the vibration and deformation of the track structure.

2.2.6 Load Distribution

The transfer of wheel loads, stresses and strains to/on the track foundation depends on the strength and stiffness properties of the track substructure. Li et al. (2015) used GEOTRACK, a three-dimensional (3D) multilayer model, to illustrate the distribution of a single wheel load from the wheel-rail interface to the subgrade layer. It was observed that the wheel load influence extends only to the fourth sleeper. The track, consisting of concrete sleepers, had a reduced maximum vertical stress at the ballast surface due to its load spreading ability over a

considerable distance as opposed to a wooden sleeper. Furthermore, the distribution of vertical stress across the track at different depths is more uniform for a concrete sleeper track.

An estimate of the wheel load on an individual sleeper was computed in previous publications and recommendations by railway authorities (e.g. Network Rail, Standards Australia) using the beam on elastic foundation (BOEF) model. The outcome of this work reveals that the transfer of 50 % of the total load onto a sleeper, directly below an axle, is a reasonable assumption for the static case (Abadi et al., 2016). Aursudkij et al. (2009) used the loading pattern of Awoleye (1993) which simulated a train running over three sleepers with 50 % of the wheel load on the middle sleeper and 25 % of the wheel load on the adjacent sleepers. However, Watanabe (Profillidis, 2000) conducted a finite-element analysis showing that the sleeper under the wheel load carried up to 40 % of the total load, 23 % by the adjacent sleepers and 7 % by the outermost sleepers. These load distributions are shown in Figure 2-9.

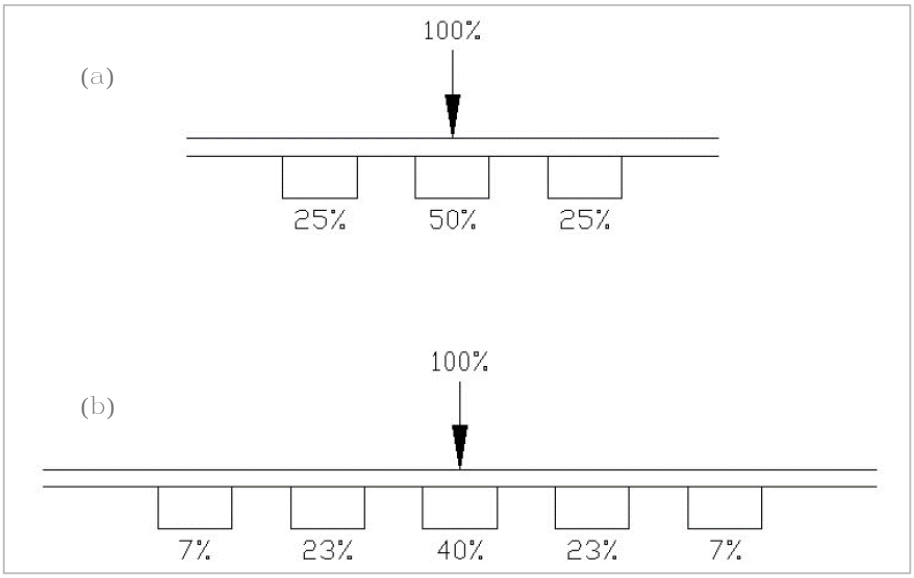

Figure 2-9: Wheel load distribution suggested by (a) Awoleye (1993) and Watanbe (Profillidis 2000)

Sadeghi (2008) conducted a comprehensive field investigation to assess the accuracy of the assumptions of current methods of railway sleeper analysis and design. A model was proposed to calculate the rail seat load based on the design wheel load and sleeper spacing (Equation 8).

$$q_r = 0.474(1.27S + 0.238)P; \qquad P = \varphi P_s \tag{8}$$

where q_r is the maximum rail seat load (where the axle is directly above a sleeper) (kN); S is the sleeper spacing (m); P is the design wheel load (kN); P_s is the static wheel load (kN); and φ is the dynamic coefficient factor.

A summary of load distribution models to calculate the maximum rail seat load is presented in Table 2-3. These models are based on the properties of the rail, sleeper spacing and sleeper support stiffness, which combine to define the track modulus.

Table 2-3: Comparison of various rail seat load models

Maximum rail seat load (kN)	Proportion of total load (%)	Model/Methods
$q_r = 0.50p$	50	Three adjacent sleeper method (Talbot 1933; Awoleye 1993)
$q_r = 0.57p$	57	Load-cell embedded sleepers (Sadeghi 2008)
$q_r = 0.43p$	43	Beam on Elastic Foundation formula (760 mm sleeper spacing)
$q_r = 0.60p$	60	AREMA method (760 mm sleeper spacing)
$q_r = 0.65p$	65	ORE method (760 mm sleeper spacing)
$q_r = 0.31p$	31	GEOTRACK (Li et al. 2015)

2.2.7 Vertical Stress Distribution

Several solutions (models) have been established to calculate the vertical stress distribution as a function of ballast depth. These solutions are essential to know how the vertical stresses induced by sleeper loadings are distributed through the ballast layer onto the formation (Doyle 1980). Table 2-4 shows the types of vertical stress solutions and their equations.

Boussinesq's elastic theory (also referred to as single-layer elastic theory) assumes that the ballast and subgrade layers form a semi-infinite, elastic, homogeneous and isotropic half space. It considers the rail seat load to be uniformly distributed over a circular area equivalent to the assumed contact area at the sleeper-ballast interface. Eisenmman's theory determines the increase in vertical stress at any location under a sleeper. This theory is based on Mohr circle stress considerations, with the sleeper considered as a uniformly loaded strip of infinite length.

Semi-empirical solutions are based on load spread methods. Clark (1957) assumed that the load is distributed vertically with a load spread slope of 45° and a uniform stress distribution at any given plane below the surface. Schramm (1961) used a method based on the angle of internal friction of ballast which is the actual load spread angle of ballast material. Typical friction angles for wet and dry ballast are approximately 30° and 40° respectively.

Empirical solutions relate the vertical pressure σ_z at depth z (m) to the uniform contact pressure, P_a at the ballast-sleeper interface. Talbot's equation was developed for a 2 642 × 230 mm sleeper and is relevant to standard and broad-gauge tracks. Furthermore, it agrees moderately

with observed field results except for ballast depths less than 200 mm or greater than 760 mm. Equations of Horikoshi and Okabe (1961) were developed by the Japanese National Railway (JNR) for narrow gauge track conditions (with a sleeper length of 2100 m).

Table 2-4: Types of solutions to calculate the vertical pressure distribution with ballast depth (modified from Doyle 1980)

Type of solution	Method	Equation (vertical stress)	Reference
Theoretical	Simplified for case of a circular area	$\sigma_z = P_a\left[1 - \frac{z^3}{(a^2+z^2)^{1.5}}\right]$	Boussinesq (1885)
	Strip Load	$\sigma_z = \frac{P_a}{\pi}\left[\theta_2 - \theta_1 - \frac{1}{2}(\sin 2\theta_2 - \sin 2\theta_1)\right]$	Eisenmann (1970)
Semi-empirical	Load Spread	$\sigma_z = 2P_a\left[\frac{BL}{(B+2z)(L+2z)}\right]$	Clarke (1957)
	Load Spread	$\sigma_z = P_a\left[\frac{1.5(l-g)B}{\{3(l-g)+B\}\, z\tan\theta}\right]$	Schramm (1961)
Empirical	Field experiment	$\sigma_z = P_a\left(\frac{1}{5.9z^{1.25}}\right)$	Talbot (1919)
	Empirical	$\sigma_z = P_a\left(\frac{58}{10+(100z)^{1.35}}\right)$	Horikoshi (JNR)
	Laboratory experiment	$\sigma_z = P_a\left(\frac{350}{240+(100z)^{1.60}}\right)$	Okabe (1961) – Broken Stone Ballast
	Laboratory experiment	$\sigma_z = P_a\left(\frac{125}{50+(100z)^{1.50}}\right)$	Okabe (1961) – Gravel Ballast

NB: σ_z, vertical stress (kPa); P_a, average uniform pressure over loaded area (kPa); z, ballast depth (m); a, radius of circular loaded area (m); θ_1 and θ_2, angles (degrees); B, width of sleeper (m); L, effective length of sleeper under the rail seat (m); l, sleeper length (m); g, distance between rail centres (m); θ, angle of internal friction of ballast (degrees).

McHenry (2013) measured the actual pressure distribution at the ballast-sleeper interface characterised by individual ballast particle contact points and non-uniform pressures using Matrix Based Tactile Surface Sensors (MBTSS). Results from laboratory ballast box tests revealed conservative estimates of peak pressure under a typical wheel load on new ballast averaged 9 997 kPa and 4 688 kPa on fouled ballast. These estimates are termed conservative due to the addition of rubber protection needed for the MBTSS system. Thus, it is likely that higher pressures would be measured without a rubber protection layer. Figure 2-10 shows typical pressure distributions for different ballast gradings subjected to a 45 kN applied load.

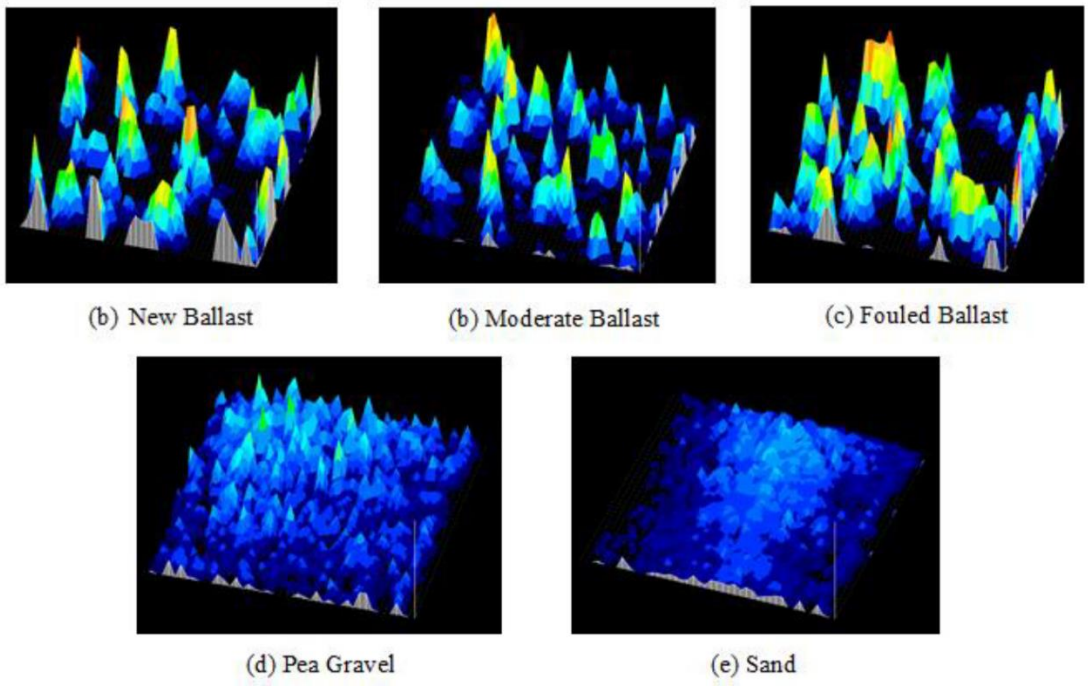

Figure 2-10: Typical pressure distribution of different ballast gradings under a 45 kN applied load (McHenry 2013)

2.2.8 Principal Stress Rotation

Principal stresses are normal stresses (perpendicular to the plane of the particle) where the shear stress is equal to zero. The principal stresses rotate to resist the applied load of a moving wheel, hence the term "principal stress rotation". As a result of the rotation of principal stresses, shear stresses develop on the horizontal and vertical planes. These shear stresses reverse direction after the train wheel moves away from the particle. This reversal action of shear stress tends to affect the soil behaviour. However, the magnitude of these stresses varies with depth, as explained earlier in Section 2.2.4. Following this, the influence of the change in shear stress does not affect the subgrade layer significantly as compared to the ballast layer (Li et al. 2015).

Studies conducted by Gräbe (2001) and Gräbe and Clayton (2003, 2009) discussed the effects of principal stress rotation (PSR) on the permanent deformation behaviour of track formations. The study revealed that PSR increases the rate of permanent strain and has a significant and harmful impact on the permanent deformation of certain foundation materials. It was also concluded that the use of more realistic testing methods such as the cyclic hollow cylinder apparatus is required to provide good estimates of the long-term performance of a rail track foundation. Further research by Gräbe and Clayton (2013) investigated the effect of PSR on the resilient behaviour of track foundation materials and concluded that PSR reduces the

resilient modulus of the test material to a greater extent, compared to cyclic loading without PSR. The degree to which PSR affects the resilient modulus is dependent on the stress state, soil type and the physical state of the soil under consideration.

Ishikawa et al. (2011) concluded that the ballast cumulative settlement caused by single-point loading is much smaller than the cumulative settlement caused by a moving-wheel load mainly because of the absence of principal stress rotation. However, Lim (2004) noticed the absence of principal stress rotation for ballast particles near sleepers. Due to traffic loads being more concentrated near the sleeper, the major principal stress of the ballast near sleepers suddenly increases as the wheel is directly above the sleeper and rapidly decreases as the wheels move away from the sleeper. However, the principal stress rotation tends to increase with depth depending on the load spreading capacity of the ballast.

2.3 SUBSTRUCTURE MATERIAL REQUIREMENTS

This section will review the properties and specifications of railway ballast. Various tests to verify ballast properties (such as strength and durability among others) as well as compaction requirements for heavy haul freight lines will be discussed.

2.3.1 Tests and Specifications for Ballast

Tests and specifications exist to ensure good ballast quality for proper performance of the railway track and to determine the mechanical and physical properties of the ballast particle. In South Africa, the S406 specification for the supply of stone (Transnet Freight Rail, 1998) is used to select the appropriate ballast material, which complies with the SABS 1083 standard. Ballast grading curve specifications, with lower and upper limits, for heavy haul lines (in South Africa) are shown in Figure 2-11. The limits specified by the SABS 1083 standard for other ballast particle properties are outlined in Table 2-5.

Common measures of gradation are the uniformity coefficient (C_u) and the coefficient of gradation (or curvature) (C_c) The uniformity coefficient is a measure of how the material will compact and how stable it will be in place. It is defined as the ratio of D_{60} to D_{10} (Equation 9). Soil is classified as well graded when C_u is greater than 4, and uniformly or poorly graded when C_u is less than 4. The coefficient of gradation can be obtained using Equation 10. A well graded soil has a C_c value between 1 and 3.

$$C_u = \frac{D_{60}}{D_{10}} \tag{9}$$

$$C_c = \frac{(D_{30})^2}{D_{60} \times D_{10}} \tag{10}$$

where D_{10} is the particle size at 10 % finer; D_{30} is the particle size at 30 % finer; and D_{60} is the particle size at 60 % finer.

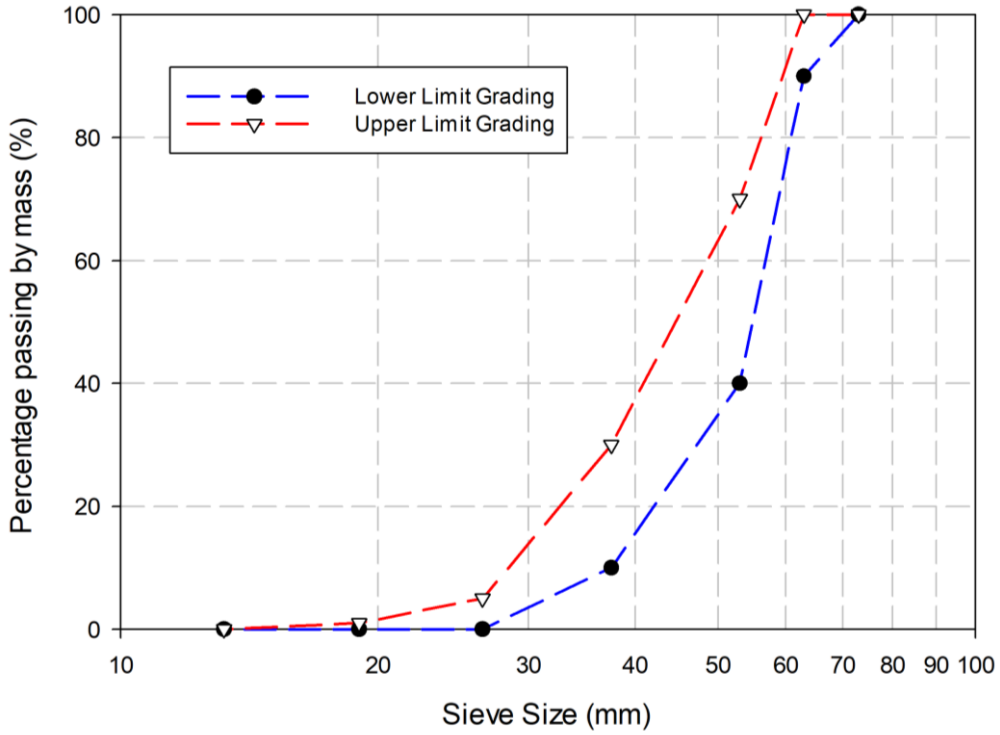

Figure 2-11: S406 ballast grading specification for heavy haul lines

Table 2-5: S406 Specification for ballast material properties

Ballast property	Transnet limits	Standard
Weathering (Soundness)	Loss in mass should not exceed 5 % after 20 cycles	
Los Angeles Abrasion (LAA)	≤ 22 %	ASTM C131 – 89 grading B
Plasticity index of fines from LAA	< 6	
Flakiness index	≤ 30 %	SABS 1083
Voids	≥ 40 %	SABS 1083
Relative density	≥ 2.5	
Mill Abrasion	≤ 7 %	Mill abrasion Test

2.4 PROPERTIES OF THE BALLAST LAYER

Ballast layer performance is defined in relation to a limiting deformation criterion. The deformation of the ballast layer develops from the combination of different deformation modes of ballast particles such as settlement and particle rearrangement, ballast fracture or crushing and ballast fatigue (Li et al. 2015). Cyclic loading behaviour is one of the primary factors that affect ballast performance and will be addressed later in this study. Figure 2-12 shows the Mohr's circle and Mohr-Coulomb failure envelope. The ultimate strength of ballast can be related to its friction angle. Table 2-6 shows the typical friction angle range and other properties of clean ballast.

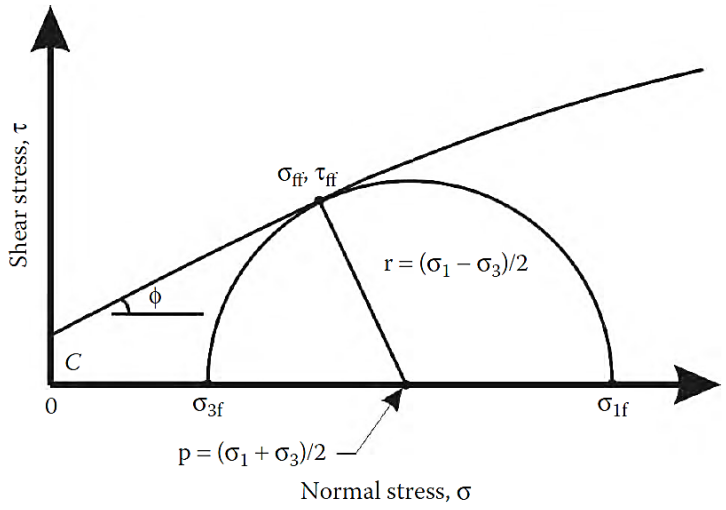

Figure 2-12: Mohr's circle and Mohr-Coulomb failure envelope

Table 2-6: Properties of clean ballast (Li et al., 2015)

Ballast properties	
Friction angle, ϕ	40° – 55°
K_0	1 – 10
Resilient modulus, M_R	140 – 550 MPa
Poisson's ratio	0.3

The Mohr-Coulomb failure envelope is tangent to the Mohr's circle at failure. Equation 11 shows the relationship between the normal stress and shear strength.

$$\tau_f = c + \sigma \tan \varphi \tag{11}$$

where τ_f is the shear strength; σ is the applied normal stress; φ is the soil friction angle; and c is the soil cohesion.

The ratio of lateral stress to vertical stress in the ballast is known as the coefficient of lateral earth pressure (K_0). The magnitude of residual stresses in the ballast layer relates to the cohesion intercept in a Mohr Coulomb diagram which is typically zero for ballast due to its non-cohesiveness. However, after compacting ballast to achieve a more dense material, interparticle forces are induced by cyclic loading which generates a cohesive component. Selig and Waters (1994) states that an increase in the residual stress can produce a K_0 value of 10 or greater.

2.5 BALLAST FOULING

Ballast fouling is the term used to describe the coarse and fine particles (0.075 mm to 19 mm) that fill up the void spaces, usually expressed as a percentage of the clean ballast material. Ballast life can be defined in terms of the amount of traffic that produces ballast mechanical wear and generation of foul material which fills up the ballast voids. The most common source of fouling material is the breakdown of ballast from cyclic loading and tamping. Other common sources include (Selig and Waters 1994 and Li et al. 2015) foreign material shipped or mixed with the ballast while it is handled or installed, material dropped or spilled on the track during train passage, windblown material, soil penetrating the ballast from the subgrade and sleeper wear or deteriorating track materials. Fouled ballast is gap-graded and the fouled material contributes to ballast drainage problems, ballast settlement (Figure 2-13, with the fouling category defined as follows: 0% - clean; 10% - moderately clean; 20% - moderately fouled; 30% - fouled; 40% - highly fouled), high rates of track geometry degradation and increased track maintenance.

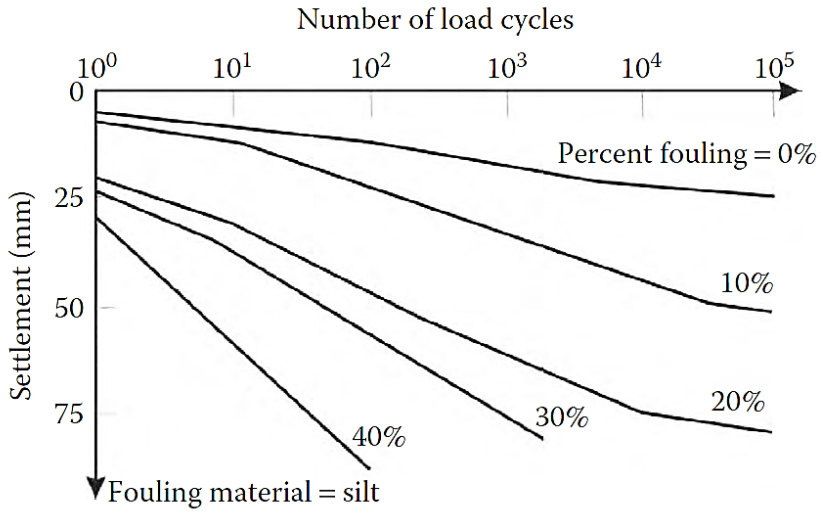

Figure 2-13: Effect of ballast fouling levels on the rate of ballast settlement (Han and Selig 1997)

2.6 BEHAVIOUR OF THE BALLAST LAYER UNDER CYCLIC LOADING

The deformation of the ballast layer under one cycle of traffic loading is characterised by a recoverable (resilient) deformation and a residual (permanent) deformation (Figure 2-14). The ballast layer strain develops rapidly and partially recovers to its original position after being exposed to the first load cycle. The continuous application of load cycles contributes to more increments of plastic/permanent strain. The magnitude of the plastic strain increment generally decreases with the number of cycles as the ballast layer densifies (Selig and Waters 1994). Previous research (Ionescu 2004; Sun et al. 2014; Sun et al. 2016) has shown that the ballast layer on a railway line exhibits time-dependent elasto-plastic behaviour which is independent on the test conditions, grain characteristics and level of compaction. This section discusses the factors that affect the permanent strain of the ballast layer.

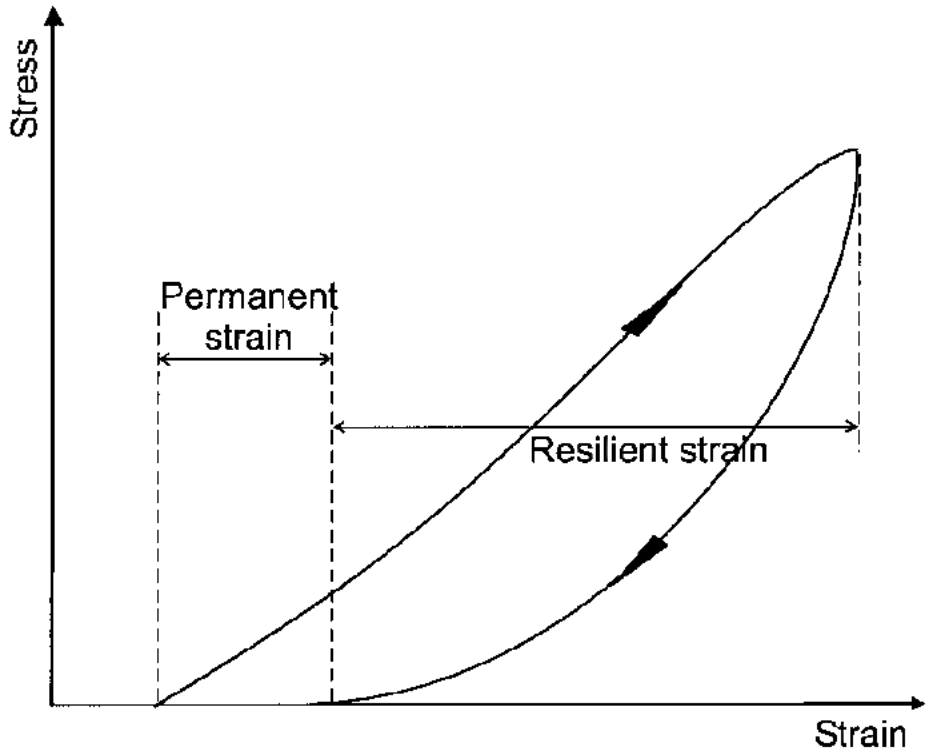

Figure 2-14: Strain in ballast layer during one cycle of traffic loading (Lekarp et al. 2000)

Permanent deformation of ballast in a rail track is in the form of settlement attributable to particle rearrangement, abrasion, and particle breakage. Previous research has investigated the factors that promote the accumulation of permanent strain in granular layers under cyclic loading. These factors (among others) are stress level, principal stress rotation, number of load applications, moisture content, stress history, density and load frequency.

2.6.1 Stress Level

The cumulative plastic deformation characteristics of ballast is mostly affected by the magnitude of the vertical and lateral applied stresses. Permanent deformation of ballast is a function of the cyclic deviator stress and confining pressure (Knutson 1976; Selig and Waters 1994). Permanent strain accumulated after several cyclic loads is directly related to the ratio of deviator stress (q) to confining stress (σ) (known as the stress ratio), where a stress ratio of 60/15 causes larger permanent strain than a 20/5 stress ratio even though both correspond to a ratio of 4 (Figure 2-15).

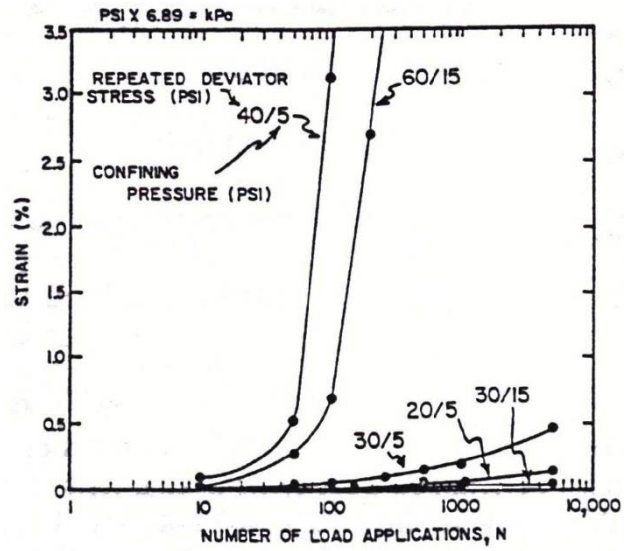

Figure 2-15: Effect of increasing stress ratio on permanent strain (Selig and Waters 1994)

2.6.2 Principal Stress Rotation

According to Lekarp et al. (2000), the effect of principal stress on granular materials is still unclear. However, several researchers (Section 2.2.8) concluded that samples subjected to principal stress rotation show an increased rate of permanent strain compared to samples where principal stress rotation is non-existent.

2.6.3 Number of Load Applications

The number of load applications is also considered as a very important factor when analysing the growth of permanent deformation in granular materials under cyclic loading, as each load cycle contributes a small increment to the accumulation of plastic strain. Barksdale (1972) and Shenton (1984) observed that permanent deformation is a linear function when plotted against the logarithm of the number of load cycles. However, the rate of permanent strain accumulation has generally been found to decrease with increasing number of load cycles. This stabilization is only achieved when low stress levels are applied (Lekarp and Dawson 1998). However, high stress levels cause a continuous increase in permanent strain.

2.6.4 Load Frequency

Shenton (1984) found that loading frequency has no effect on permanent deformation of ballast. However, Indraratna et al. (2010a) and Sun et al. (2014) conducted cyclic triaxial tests to understand the long-term response of railway ballast under different load frequencies (between 5 Hz and 60 Hz) and concluded that three different deformation mechanisms exist according to loading frequencies (Table 2-7).

Table 2-7: Different deformation mechanisms with increasing cyclic frequency (Sun et al. 2014)

Range	Deformation mechanisms	Load frequencies
I	Plastic shakedown	$f \leq 20\ Hz$
II	Plastic shakedown and ratcheting	$30\ Hz \leq f \leq 50\ Hz$
III	Plastic collapse	$f \geq 60\ Hz$

Furthermore, it was noted that as the frequency and number of load applications increased, the ballast permanent strain, particle breakage, and volumetric strain increased also (Figure 2-16 and Figure 2-17).

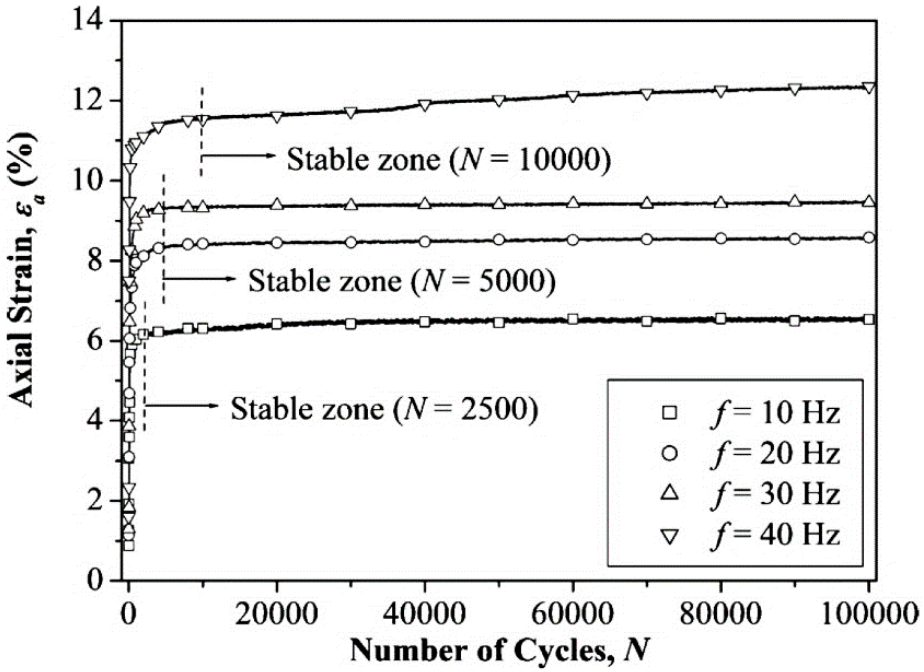

Figure 2-16: Axial strain at various frequencies with increasing number of load cycles (Indraratna et al. 2010a)

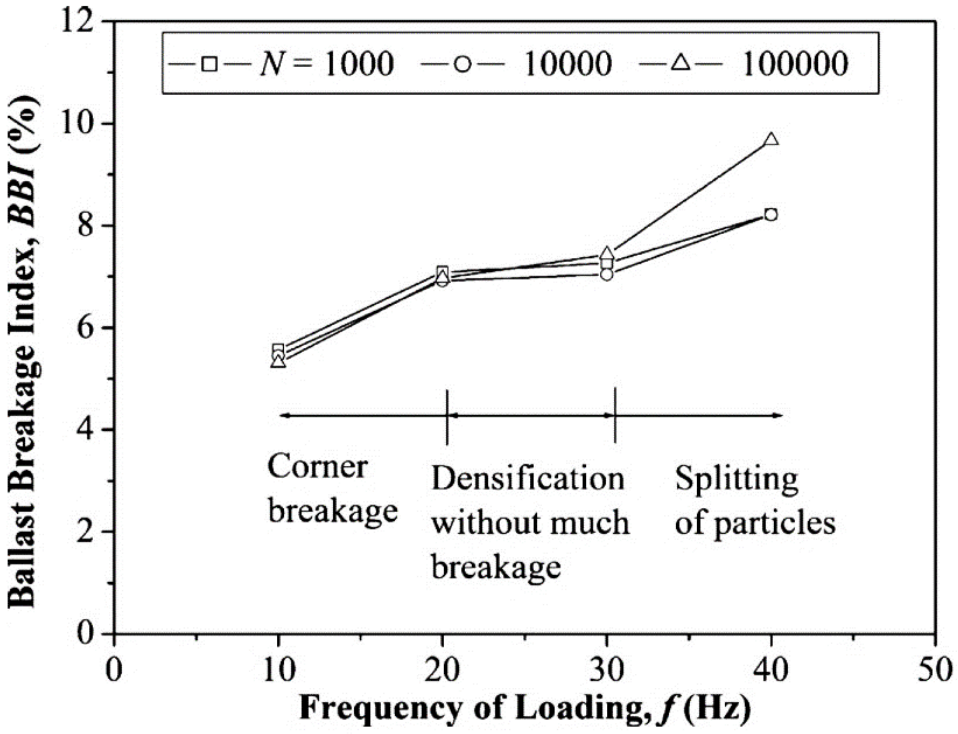

Figure 2-17: BBI for various frequencies at specific number of load cycles (Indraratna et al. 2010a)

2.7 MODELS FOR PERMANENT DEFORMATION BEHAVIOUR

Ballast permanent strain (deformation) under cyclic loading often accounts for the largest portion of track settlement of all layers that make up the track substructure. Therefore, ballast settlement usually controls the need for regular track geometry checks and maintenance. The ability of ballast to retain a stable track geometry depends mainly on material quality, physical state and load magnitude. Based on numerous studies, the relationship between the number of load applications and settlement of ballast has been found to be non-linear. According to Selig and Waters (1994) and Li et al. (2015), the fundamental equation (Equation 12) used for vertical ballast plastic strain is:

$$\varepsilon_N = \varepsilon_1 N^b \tag{12}$$

where ε_N is the plastic strain after N load cycles; ε_1 is the first cycle plastic strain and b is a constant exponent. This power equation (Equation 12) was obtained as a best fit to ballast strain data from field and laboratory tests. It indicates a rapid initial settlement followed by a gradual reduction in the rate of settlement with increasing number of load cycles.

Another common mathematical model for calculating the permanent deformation of ballast was developed by Alva-Hurtado and Selig (1981). The permanent strain (ε_N) after a number of cycles (N), can be closely related to the permanent strain after one cycle (ε_1), by Equation 13:

$$\varepsilon_N = \varepsilon_1(1 + C \log N) \tag{13}$$

where C is a dimensionless constant controlling the rate of deformation. Selig and Waters (1994) suggested typical values for C ranging from 0.2 to 0.4.

Hettler (1984) observed that the settlement of ballast was proportional to the logarithm of the number of load cycles and expressed the results by the lognormal model as follows (Equation 14):

$$S_N = S_1(1 + c' \ln N) \tag{14}$$

where the factor c' has values between 0.25 and 0.55. Although, the initial settlement (S_1) might be a non-linear function of the load amplitude (F_l), from measurements, S_1 was estimated from Equation 15:

$$S_1 = sF_l^{1.6} \tag{15}$$

where s is a scaling factor and the settlement after many load cycles is dependent on the settlement of the first cycle. This model (Equation 14) is comparable to Alva-Hurtado and Selig's model, however Hettler's model is expressed in terms of settlement instead of strain.

Shenton (1984) suggested a settlement law based on field and laboratory experiments (Equation 16) where the settlement of ballast is proportional to the fifth root of the number of load applications, which corresponds well with site measurements up to 10^6 load cycles.

$$S_N = K_1 N^{0.2} + K_2 N \tag{16}$$

where constants K_1 and K_2 are selected to make the second term become significant only for values of load cycles (N) larger than 10^6. These constants depend on axle load, rail section, sleeper spacing and track and foundation stiffness.

Thom (2006) established a relationship between settlement and load cycles based on laboratory test results from the full-scale Railway Test Facility (RTF) at the University of Nottingham. Equation (17) was found to be a reasonable fit to the RTF data.

$$S_N = (\log_{10} N - 2.4)^2 \tag{17}$$

where N represents the number of load cycles of the track. Additionally, Thom (2006) proposed that the settlement at any load level and variation in subgrade can be described according to Equation (18a):

$$S_N = (\log_{10} N - 2.4)^2 \times \left(\frac{\sigma}{160}\right) \times \left(\frac{47}{k}\right) \quad (18a)$$

where σ is the stress under the sleeper; k is the modulus of subgrade reaction, which is the constant of proportionality between the contact pressure of a foundation (P_c) and the settlement of the foundation (S), defined as:

$$k = \frac{P_c}{S} \quad (18b)$$

Apart from modelling granular permanent deformation with respect to number of load cycles, other research focusing on the relationship between permanent deformation and stress condition as well as the granular shakedown effect, have been conducted.

2.8 PARTICLE BREAKAGE AND QUANTIFICATION

McDowell et al. (1996) stated factors that govern the survival probability of a particle in an aggregate subjected to a one-dimensional compressive load. These factors are applied macroscopic (external) stresses, size of the particle and coordination number (i.e. number of contacts with neighbouring particles). An increase in external applied stress will increase the probability of particle fracture. Variations in soil particle strength exist due to the dispersion of internal flaw sizes. McDowell and Bolton (1998) proposed that yielding of a particle subjected to one-dimensional compression was due to the commencement of particle fracture. Furthermore, the yield stress of an aggregate is proportional to the average tensile strength of the constituent grains. The probability of fracture will decrease with a decrease in particle size, as larger particles will exhibit a low average tensile strength due to more and larger internal flaws. Angular particles break easily because stresses tend to concentrate along weak areas (Hardin 1985 and Lade et al. 1996).

A higher coordination number (number of surrounding particle contacts) will decrease the chances of particle fracture. Figure 2-18 illustrates the effect of higher coordination number in reducing the induced tensile stress for a round particle and an angular particle. According to McDowell et al (1996), a higher coordination number will effectively reduce the induced tensile stress for a rounded particle and the opposite for an angular particle.

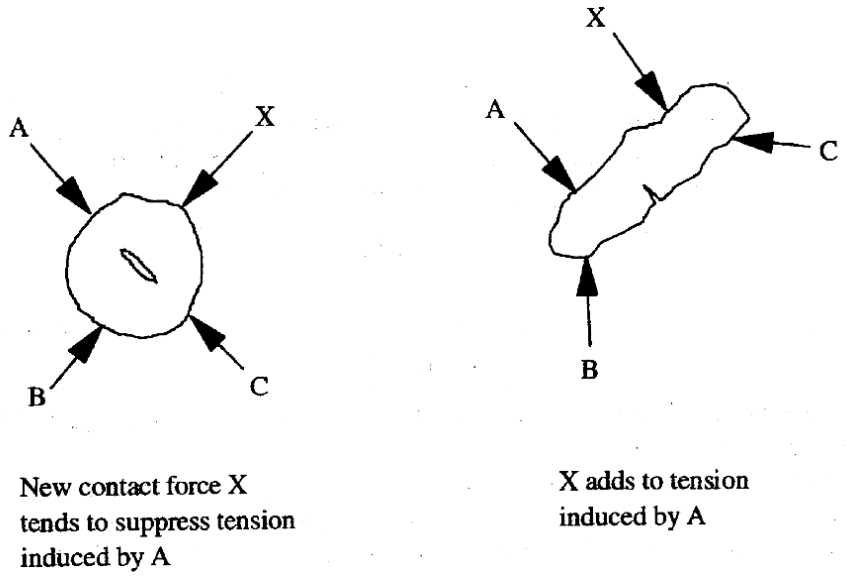

Figure 2-18: Effect of coordination number on particle shape (McDowell et al. 1996)

Shahin et al. (2007) summarised the main factors that influence ballast breakage which are ballast properties that are related to parent rock characteristics (such as hardness, toughness, specific gravity, grain texture, mineral composition and internal bonding etc.), physical properties associated with individual ballast particle and other factors relating to the assembly of particles and loading conditions.

Lade et al. (1996) summarized the most widely used particle breakage indices. All breakage indices are based on changes in particle size after loading. Some indices are based on change in a single particle size, while others are based on changes in overall grain-size distribution.

Marsal (1967) proposed an index of particle breakage (B_g) after conducting large-scale triaxial tests on rockfill materials. This method is based on the difference in percentage retained $(\Delta W_k = W_{ki} - W_{kf})$ on each sieve before and after a test, where W_{ki} is the percentage retained on a specific sieve before the test and W_{kf} is the percentage retained on the same sieve after the test for a given ballast sample. Marsal's breakage index, B_g, is represented by the sum of positive ΔW_k values, expressed as a percentage. This breakage index has a lower limit of 0 % indicating no ballast breakage and an upper limit of 100 % indicating that all particles are broken down to sizes below the smallest sieve size used.

Indraratna et al. (2005) and Lackenby et al. (2007) introduced a new Ballast Breakage Index (BBI) specifically for railway ballast, to quantify the extent of degradation by evaluating the change in area of particle size distribution before and after testing as illustrated in Figure 2-19. Using a linear particle size axis, the BBI can be determined from Equation 19:

(19)

$$BBI = \frac{A}{A + B}$$

where A is a shift in the PSD curve after testing and B is the potential breakage or area between the arbitrary boundary of maximum breakage and the final PSD defined in Figure 2-19.

Lee and Farhoomand (1967) proposed a breakage indicator expressing the change in a single particle size (D_{15}) during an investigation on the effects of particle crushing on the plugging of dam filters. Hardin (1985) introduced a relative breakage index B_r ($= B_t/B_p$) consisting of two quantities: the breakage potential B_p and total breakage B_t, based on changes in grain-size distribution. This particle degradation indicator requires a numerical integration technique for computing B_t and B_p. Miura and O-hara (1979) used the changes in grain surface area (ΔS) as an indicator of particle breakage. This was based on the idea that new surfaces could be generated as the particles were broken, hence, the changes in surface area could be used as a measure of particle breakage. The specific surface area for each particle size (i.e. sieve size) is computed assuming all grains are perfectly spherical. Sieving data before and after the test and specific surface area can be used to calculate changes in surface area, ΔS.

Ballast breakage in a box test usually occurs in the area beneath the sleeper during cyclic loading. Ballast degradation tests conducted by Lim (2004) in a box test showed that ballast degradation in areas away from the sleeper area was negligible. Selig and Waters (1994) dyed the ballast under the sleeper to aid ballast breakage detection. According to Abadi et al. (2016), the degree of grain breakage was not sufficiently significant to detect by comparing PSDs before and after dynamic loaded tests. Therefore, the ballast below the sleeper was painted, and weighed prior to and after testing to determine the percentage weight loss due to ballast breakage.

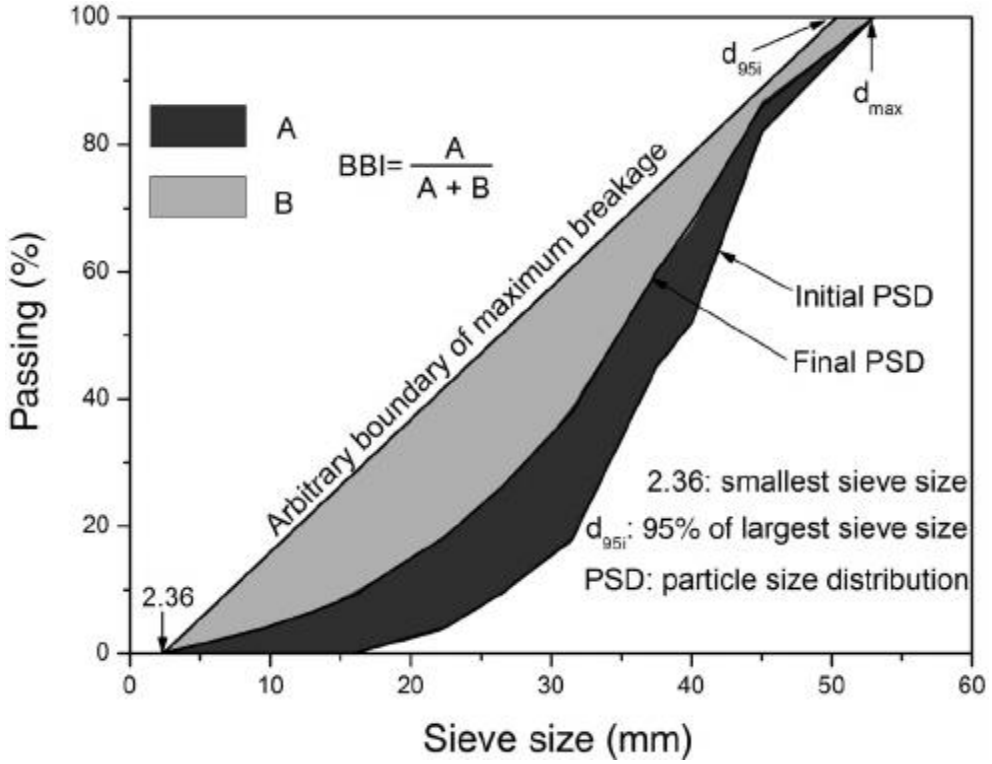

Figure 2-19: Ballast Breakage Index (BBI) (Indraratna et al. 2005)

2.9 EFFECT OF CONFINING PRESSURE ON BALLAST BREAKAGE AND DEFORMATION

The effect of confining pressure on the behaviour of ballast is not considered as a significant factor in rail track design. Figure 2-20 shows the effect of confining pressure on particle degradation using the ballast breakage index (BBI). Indraratna et al. (2005) and Lackenby et al. (2007) divides the ballast degradation behaviour into three zones (Figure 2-20) following a series of triaxial tests. These zones are the (I) Dilatant Unstable Degradation Zone (DUDZ), (II) Optimum Degradation Zone (ODZ), and (III) Compressive Stable Degradation Zone (CSDZ).

The confining pressure is low ($\sigma_3' < 30$ kPa) in DUDZ where rapid and considerable axial and expansive radial strains acted on the sample, which leads to an overall volumetric increase or dilation as shown in Figure 2-21. Considerable degradation occurs via shearing and attrition of angular projections. Due to the application of small confining pressures, specimens in this degradation zone are characterised by a limited co-ordination number as well as relatively small particle-to-particle contact area. Most degradation in this zone is due to breakage of angular corners or projections, with very little particle splitting observed.

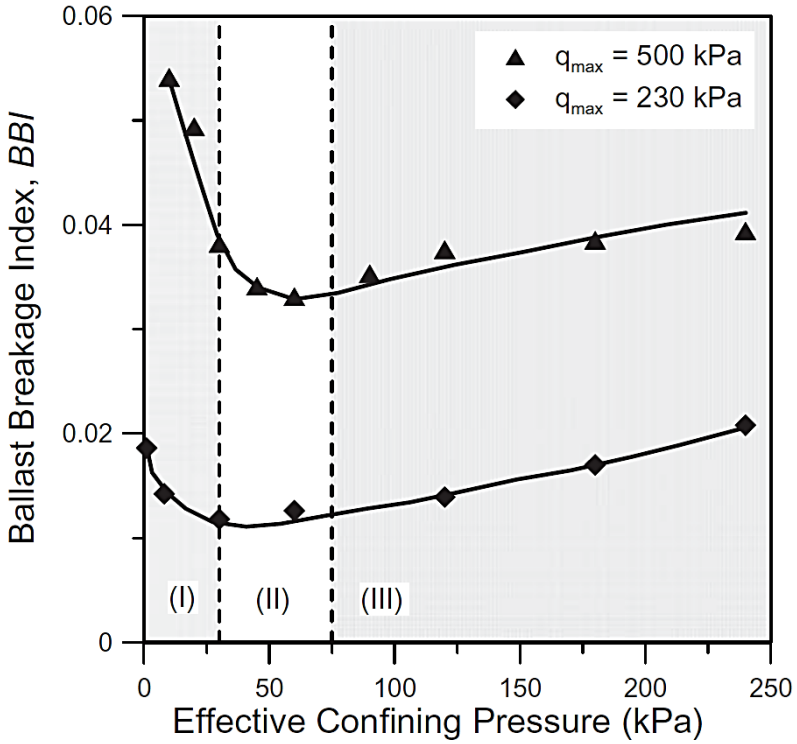

Figure 2-20: Effect of confining pressure on particle breakage, with degradation zones (Indraratna et al. 2005; Lackenby et al. 2007)

The axial strain rate is considerably decreased due to an apparent increase in stiffness as the confining pressure approached the optimum zone (ODZ: 30 kPa $< \sigma_3' <$ 75 kPa). The overall volumetric behaviour is slightly compressive. In this zone, particles are held together with sufficient lateral confinement to allow for an optimum distribution of contact stress and increased inter-particle contact areas. This would decrease the risk of breakage associated with stress concentration. A further increase in confining pressure towards the CSD zone ($\sigma_3' >$ 75 kPa), forces particles toward each other, with limited space for sliding and rolling. Some particle splitting takes place through planes of weakness such as microcracks and other flaws and the fatigue of particles are prominent.

Although there is no direct measure of in-situ confining pressure, it is expected that the effective ballast confining pressure is less than 20 kPa (DUDZ). To prevent rapid settlement and promote a high degree of uniform track stiffness, track confinement can be increased by:

- Reducing the sleeper spacing
- Increasing the height of shoulder ballast
- Including a geosynthetic layer (geocell) at the ballast-subballast interface
- Widening the sleepers at both ends (winged concrete sleepers)
- Using intermittent lateral restraints at various track sections

- Decreasing the ballast shoulder slope (Abadi et al. 2016).

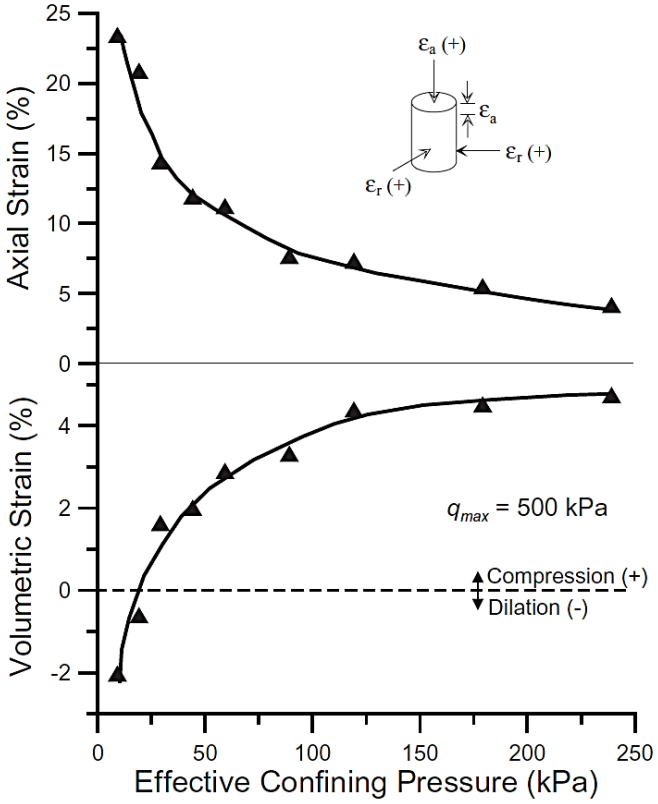

Figure 2-21: Variation of axial and volumetric strains with confining pressure (Lackenby et al. 2007)

2.10 BALLAST COMPACTION

The process of ballast compaction involves the interlocking of ballast particles into a firmer arrangement with increasing number of load cycles. This is done to increase the ballast layer stiffness by increasing the particle interlock, hence limiting the stress transmitted to underlying track layers. Furthermore, proof rolling is a common practice performed during construction of railway lines and buildings to compact the old exposed formation layer on which the new track will be constructed. This is done to reveal weak spots that require excavation, replacement, reinforcement or drainage. Proof rolling is also performed to ensure adequate compaction in railway applications such as heavy haul and high-speed lines, as well as critical locations (e.g. bridge transitions) (Li et al. 2015).

According to Selig and Waters (1996), two different methods of compaction are available: 1) lateral and vertical track vibration using a Dynamic Track Stabilizer, and 2) crib and shoulder surface compaction. The Dynamic Track Stabilizer is designed specially to provide quick on-

track ballast compaction following ballast tamping. The stabilizer grips the track laterally, applies a vertical force (up to 356 kN) and vibrates the track horizontally at a frequency of 25 Hz – 45 Hz to rearrange and compact the ballast. However, the amount of compaction - determined by the amplitude and frequency of vibration and the magnitude of vertical force provided by the stabilizer - is not generally known and is difficult to estimate (Li et al. (2015). Selig and Waters (1996) reported that one pass of the track stabilizer is equivalent to the trafficking compaction effects of between 100 000 and 700 000 tonnes of normal traffic, to restore vertical track stability. Sussmann et al. (2003b) also reported that the compaction using the track stabilizer is generally more uniform and controlled compared to ballast compaction from traffic.

Surface compactors apply a vertical vibratory force to pads pressed down onto the ballast surface by a vertical static force. Ballast in the cribs are compacted in the zones penetrated by the tamping tools. Pressure plates are often used on the ballast shoulder slopes to prevent lateral flow of the ballast during vibration. Surface compactor parameters are static down force, generated dynamic force, vibration frequency and duration, with values ranging from 7.6 kN to 9.8 kN, 4.9 kN to 30.7 kN, 25 kN to 75 Hz and 2 to 4 seconds respectively.

Many researchers have used the density (or void ratio) to quantify ballast initial compaction condition in the field to obtain an appropriate ballast settlement behaviour during laboratory tests. Tutumluer et al. (2011) reported that an appropriate and convenient method to quantify the ballast compaction level or density in the field is not readily available. However, a detailed approach was established to assess the initial compaction condition (void ratio) of a newly constructed ballast layer to accurately predict field settlements using Discrete Element Modelling. It was found that the void ratio for field compacted ballast was between 37 % and 44 %.

2.11 LABORATORY TESTS ON BALLAST

Laboratory tests provide room for controlling test and material variables as opposed to field testing. It also provides an avenue to access the influence of these variables and establish detailed relationships between various ballast parameters and expected performance. Laboratory tests produce results in the shortest time possible by accelerated testing of construction materials. These results are validated with field test results. Several laboratory tests on ballast have been performed to investigate different factors that tend to affect the behaviour of ballast. Laboratory testing techniques such as box tests and triaxial tests – the most common tests conducted on railway ballast – are discussed briefly in this section.

2.11.1 Ballast Box Tests

A box test simulates ballast behaviour and performance under field conditions for a track section. Various boxes have been created for laboratory tests to simulate the sleeper-ballast interface. Al-Saoudi and Hassan (2014) summarised previous laboratory box tests conducted on ballast as shown in Table 2-8. The dimensions of the box for laboratory testing are usually determined based on the simulation area of the track section as illustrated in Figure 2-22.

Table 2-8: Ballast box test setups (modified after Al-Saoudi and Hassan, 2004)

Reference	Model/Box size (mm)	Material type and size (mm)	Setup
Panuccio (1979)	482 diameter and 305 high	Crushed limestone ranges (20-38)	127 mm diameter surface plate
Morgan and Markland (1981)	1200 × 1200 × 700 deep	Crushed limestone, 19 single size grading	Vibrating table equipment
Harry et al. (1985)	300 × 600 × 475 deep	Angular traprock, Conform to AREA No.4 gradation	Laboratory box testing device
Dave (1998)	900 × 200 × 330 deep	Rounded denstone ceramic particle, 3 single size grading	193.5 cm2 air pressure loading piston
William et al. (2000)	1000 × 800 × 600 deep	Angular medium gravel, 50 single size	Sine wave loading-unloading cycle between (2.1-18.2) kN
Lim (2004)	700 × 300 ×450 deep	Granodiorite and granite, conform to (RT/CE)	Sleeper sin wave load of 40 kN on box-test
Khawla (2007)	600 × 300 × 450 deep	Limestone, conform to (IRR 2000)	Repeated loading
Du Plooy (2015)	2408 × 600 × 400 deep	Quartzite, conform to S406 specifications	Laboratory box test, sine wave loading of 260 kN

Bennett et al. (2011) investigated the influence of the box type, material and associated measurements to ensure that the influence of significant parameters can be measured within the limitations of the box. It was suggested that a bigger box is generally suitable to limit the influence of the box edges. This however, will require more sample preparation, setup, and applied load (Li et al. 2015). In addition, ballast box designs must consider the stiffness and

frictional resistance of the sides to ensure reasonable conformity with field performance observations.

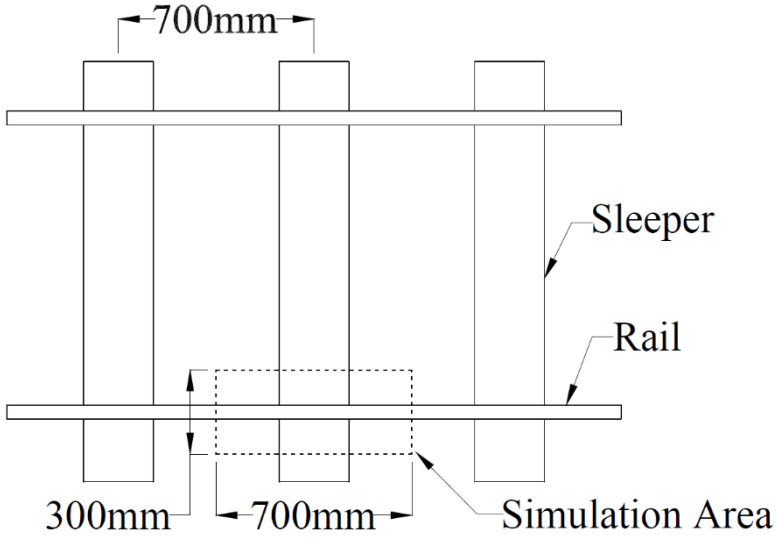

Figure 2-22: Track section represented by test box dimensions (Lim 2004)

Box tests are also adaptable as different results can be obtained such as sleeper settlement (ballast deformation), ballast stiffness, ballast modulus, horizontal stresses in the ballast and ballast breakage. The sleeper settlement (ballast deformation) is commonly measured using a Linear Variable Differential Transducer (LVDT). Ballast stiffness, K, can be calculated by dividing the applied deviator stress by the resilient displacement of ballast per cycle (Equation 20):

$$K = \frac{\sigma_{max} - \sigma_{min}}{\delta_{max} - \delta_{min}} \tag{20}$$

where σ_{max} and σ_{min} are the maximum and minimum applied stress, respectively, and δ_{max} and δ_{min} are the maximum and minimum sleeper displacement, respectively. The ballast stiffness obtained from ballast box tests is comparable to the resilient modulus.

Selig and Waters (1994) and Abadi et al. (2016) measured the horizontal stress in the ballast by installing stress sensors along the inside wall. Selig and Waters observed that both horizontal stresses of ballast at the loaded and unloaded states (at maximum and minimum load cycles, respectively) eventually reach 30 kPa. Furthermore, Abadi et al. observed that the constant horizontal stress in any test varies between 15 kPa and 32 kPa.

According to Li et al. (2015), although ballast box tests provide evidence that hanging sleepers damage track and cause more settlement than well supported sleepers, the real benefit of box

tests is that it provides the ability to quantify damage. This damage assessment and quantification can support the planning and support for maintenance of railway lines.

2.11.2 Triaxial Tests

Triaxial tests closely resemble the load environment and failure mechanisms of ballast in track. Cyclic triaxial loading tests are recommended for ballast evaluation that consider ballast performance parameters relating to strength such as stiffness and deformation. Furthermore, triaxial tests are used to characterize ballast in terms of strength, which provides both the friction angle and stiffness of the ballast. Drainage conditions can be controlled during triaxial testing.

However, most triaxial tests do not consider the effect of wheel configuration when employing a loading pattern (Indraratna and Ionescu, 2000; Ebrahimi et al. 2012). The loading pattern commonly used in triaxial tests are based on pavement loading (haversine). Furthermore, testing large granular materials in a conventional triaxial apparatus can lead to vague results caused by disparity between equipment size and the particles being tested. Therefore, tests involving large aggregates are done in a large-scale triaxial apparatus. It is recommended that the diameter of the aggregate sample being tested should be at least 2.5 – 3 times greater than the largest individual particle size according to ASTM standards (Li et al. 2015).

2.12 SUMMARY

This chapter focussed primarily on ballasted (conventional) track. Although ballastless track do exist, the conventional track to date is by far the most common and economical track utilized. The design of railway track is commonly based on axle loads and wheel spacing. Reducing the wheel spacing causes the influence lines from each wheel load to overlap, causing higher stresses, thus increasing the vertical deflection of the track. Therefore, the length of a train and wheel configuration are important factors to consider when determining the cumulative effect of cyclic loading on a track structure, especially when conducting laboratory test simulations.

According to research conducted (Powrie et al, 2007; Li et al., 2015), the loading magnitude and shape of loading pulses changes with depth. Consequently, the loading pattern (or shape) and influence of individual train wheel load is more prominent on the ballast layer. However, current laboratory tests use a single load cycle comprising 4 wheel loads to simulate train loading on the ballast layer which is contrary to the fact that the load shape and influence of individual wheel loads diminish significantly at the subgrade – where a single load cycle comprises 4 wheel loads which take the shape of a single trapezoidal load (Figure 2-7).

Most laboratory tests on ballast, either box or triaxial tests, employ haversine loads to simulate train wheel loads. However, the effect of wheel spacing, loading impulse (area under loaded curve) and wheel load overlap are not considered when choosing a loading pattern. Common practice for laboratory tests on ballast is to assume that a single haversine load cycle represents the 2 wheel loads or 4 wheel loads depending on the wheel configuration – which does not depict field loading conditions. Haversine loading was used for subgrade materials in previous research publications. Current ballast loading practices use haversine loading without applying a controlled number of load pulses. This loading condition for ballast laboratory testing needs to be evaluated and compared with multiple load pulse per load cycles which is identical to field loading conditions, as there are no test procedures or protocols addressing appropriate loading patterns for a given train configuration. Furthermore, factors affecting ballast particle breakage include applied macroscopic stresses, particle size and coordination number. Assessing the effect of confining pressure on ballast breakage from a ballast box test perspective has not yet been investigated.

In conclusion, although researchers have performed box tests using haversine loading patterns, a closer look at the effect of loading pattern and impulse on the rate of ballast degradation and establishment of a suitable cyclic loading pattern – which considers train wheel configuration for laboratory box tests, is important. Also, a review of the effect of lateral confinement on the ballast layer behaviour using a ballast box apparatus is also an area for investigation.

3 EXPERIMENTAL MATERIALS AND SETUP

A series of box tests were conducted to address the objectives of this study. This section of the dissertation focuses on the assumptions made during the design of the test box to complement field loading and boundary conditions. The materials required for the experiment, the equipment and measuring devices to simulate train loading and record deflection data respectively as well as the experimental setup are discussed.

3.1 MATERIALS

This section lists and explains materials used in the experiments conducted. Design aspects related to the materials and other experimental components are discussed with reference to their influence on the experimental precision and accuracy.

3.1.1 Ballast

The ballast used in the laboratory tests was obtained from Ferro quarry (operated by Afrisam), situated in the northern region of Pretoria, 10 km from the University of Pretoria. The ballast material is quartzite - a non-foliated metamorphic rock. Fine particles around the surface of the ballast stones were removed by washing the ballast prior to particle size distribution determination and other tests. This was done to eliminate the influence of fouled material on the behaviour of the ballast material during cyclic loading (Tennakoon et al. 2014).

The particle size distribution was compared with the lower and upper limit of the S406 Ballast Specification as shown in Figure 3-1. Generally, the ballast material fell within the specified grading envelope, therefore complying with the S406 ballast specification for grading. The coefficient of uniformity, C_u and coefficient of curvature (shape of PSD curve), C_c of the ballast, were assessed. The graded ballast is uniformly graded with a C_u value of 1.60 (< 4) and well-graded with a C_c value of $1.03 \approx 1$ ($1 < C_c < 3$). Durability, specific gravity, voids and flakiness index tests were conducted and their results comply with the S406 ballast specification.

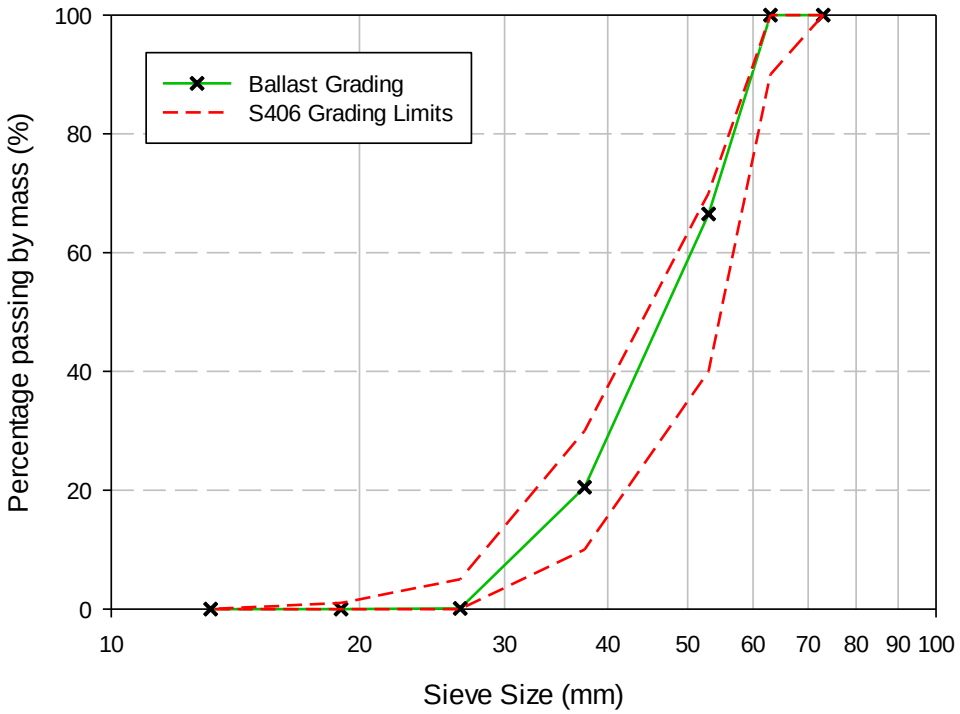

Figure 3-1: Particle size distribution of ballast compared with S406 specification grading limits

3.1.2 Steel Box

To simplify the test setup and retain a high level of practicality, a steel box was built to represent half a single sleeper bay of a typical railway track. The design of the steel box was based on the track dimensions of the Coal Line in South Africa. Only half a sleeper was modelled due to longitudinal track symmetry. In this study, a uniform stress distribution was assumed to occur at the base of the sleeper (Figure 3-2).

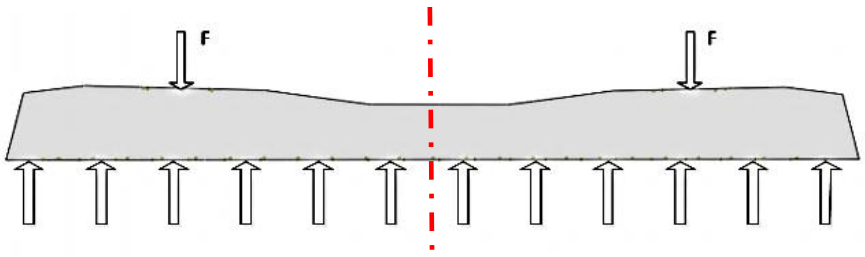

Figure 3-2: Uniform ballast-sleeper contact pressure (Talbot 1933)

The steel box was designed according to the minimum requirements of the ballast layer for a 1065 mm gauge track, specified by Spoornet (2000). A ballast shoulder slope of 1:1.5 was incorporated into the design length of the steel box. The design width of the steel box is

650 mm, which represents the sleeper spacing on the South African Coal Line. The design height of the steel box is 450 mm consisting of a ballast height of 300 mm and a 100 mm clearance for the crib ballast and 50 mm extra allowance. The joints of the steel box were arc welded using 6310 electrode welding rods. A three-dimensional drawing and plan view of the steel box is shown in Figure 3-3. Table 3-1 shows the selected dimensions of the box.

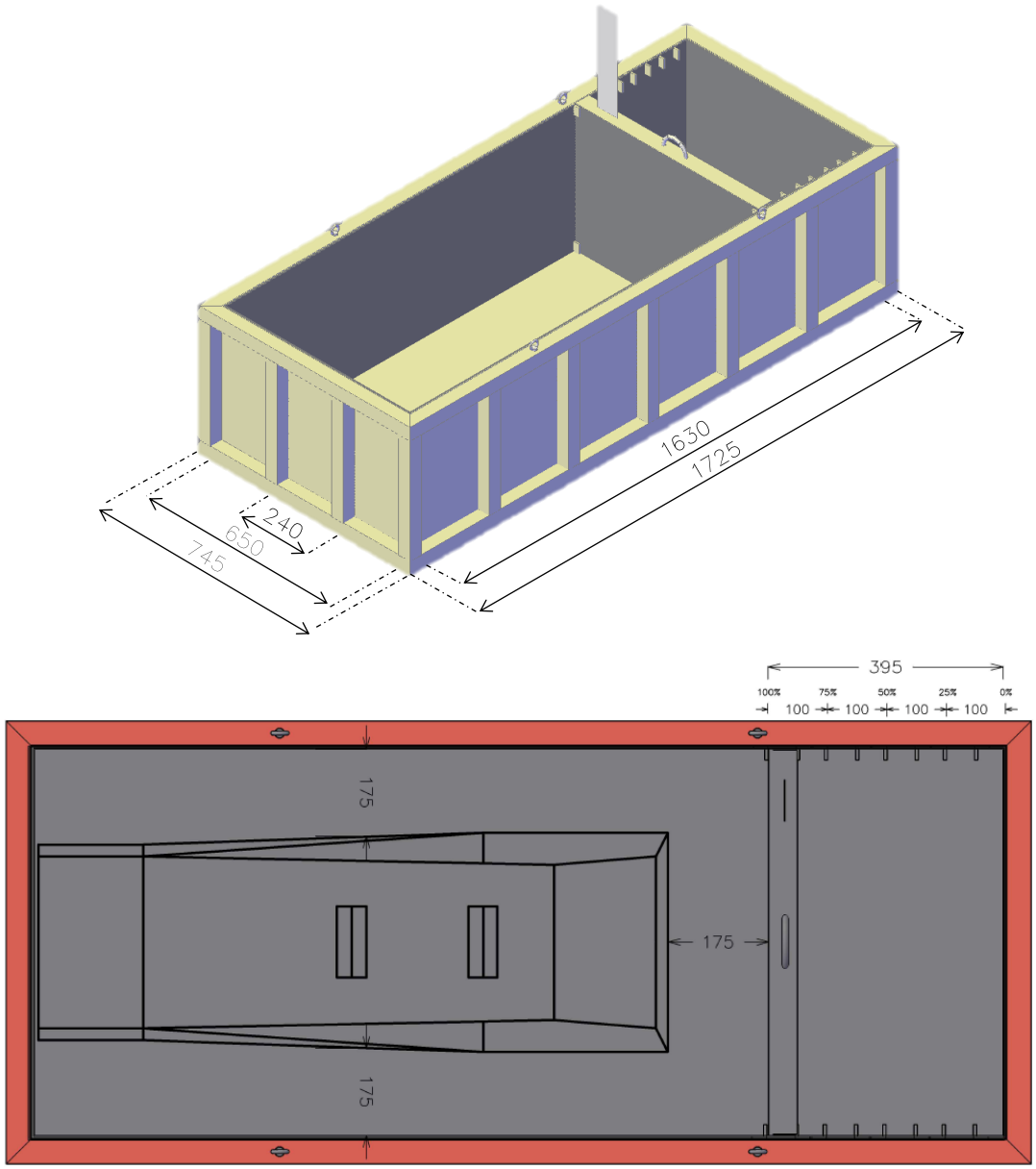

Figure 3-3: 3D drawing of steel box

Square hollow sections (SHS), 38 × 38 × 3 mm, were used for the box frame and served as vertical braces to prevent lateral buckling of the 2 mm mild steel sheets around the box. A 2 mm

steel sheet was placed at the base of the box. M12 links to aid lifting of the box were placed along the length of the steel box. 30 mm long angle bars (25 × 25 × 5 mm) were used to create four (4) slots to adjust the lateral confinement of the ballast. A steel framed gate (shown in Figure 3-4) consisting of 38 × 38 × 3 mm square steel tubes and a 2 mm thick steel sheet was made to fit into the slots. The dimensions of the gate are 650 × 450 × 40 mm. The average distance of 175 mm was calculated between the sides of the sleeper and the wall of the steel box. To achieve a fully confined setup (termed as 100% lateral confinement), the distance from the end of the sleeper to the steel gate was set to 175 mm. The distance between the steel gate and the end of the steel box (toe of ballast shoulder) was divided into 4 portions to represent 75 %, 50 %, 25 % and 0 % lateral confinements (with a full ballast shoulder representing 0% lateral confinement). 3 mm thick neoprene sheets were glued to the vertical sides of the steel box and gate. Thin sheets (250 μm thick) of Anti-Termite Damp-Proof Course were glued onto the neoprene sheets on the vertical sides of the box as well as the gate.

Table 3-1: Dimensions of the ballast box

Property	**Value**
Length - Internal (mm)	1630
Width – Internal (mm)	650
Height (mm)	450
Spacing of vertical square tubing (mm)	230

In addition to the lateral resistance provided by the slots, four holes were drilled through the 2 mm steel sheet at the base of the steel box where a welded steel rod protrusion from the base of the gate fits. A flat steel plate was welded to the top surface of the gate to support the Tekscan handle. The box was painted with red oxide. The weight of the steel box and gate without ballast material is 76 kg.

Figure 3-4: Steel gate and associated features

3.1.3 Sleeper

A 1065 mm gauge concrete PY sleeper weighing 280 kg was cut in half using a diamond disk. This cutting action was to meet the test box design requirements stated in Section 3.1.2. This type of sleeper is designed for heavy-haul lines with a maximum axle load of 30 tonnes. Figure 3-5 shows the cutting details of the sleeper.

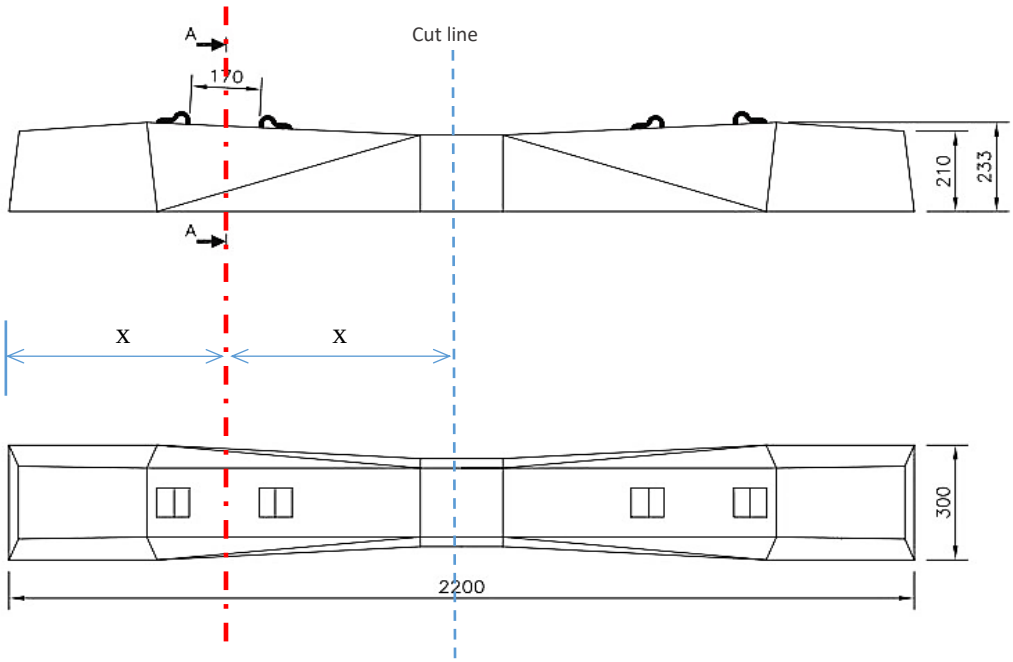

Figure 3-5: PY concrete Sleeper (dimensions and cutting details) - Side and Top view

3.1.4 Rail Piece (sleeper - actuator piston support)

The sleeper was fixed temporarily to the actuator piston to limit any lateral movement. In this regard, a mild steel bar (377 × 150 ×150 mm), weighing 40 kg, was used to link the sleeper and the actuator piston. The steel bar was milled to form a bevelled edge with a 1 in 20 slope to level off the rail-seat slope on the sleeper. The mild steel bar was also used to represent a section of a rail placed on the sleeper. Two 230 × 35 × 35 mm mild steel bars were used to support two 20 mm steel rods passing through the Pandrol 'e' clip slots on the sleeper. Bolts were used to join the main components of this connection to establish a temporary and flexible setup.

3.1.5 Rubber Base

A double layered insertion rubber was placed at the bottom of the box to emulate the compressibility of the substructure. Each layer of rubber sheeting was 3 mm, producing a 6 mm thick rubber base in total. The two layers of insertion rubber also served to protect the Tekscan pressure sensors (placed in between) against puncture.

3.2 TEST EQUIPMENT AND INSTRUMENTATION

This section focusses on the equipment and instrumentation used for the tests conducted. These include the hydraulic actuator, force and displacement transducers, Tekscan pressure mat as well as data analysis tools.

3.2.1 Hydraulic Actuator

A hydraulic actuator was used to apply dynamic loads to the ballast samples. The hydraulic actuator formed part of the components of the load unit (Figure 3-6). In addition to the hydraulic actuator, the load frame is a basic component structure providing the reaction mass for the force train, having an overall system stiffness of 7.4×10^5 kN/m. The load frame and other hydraulic components mounted to it collectively create the load unit. It will be referred to as the Materials Testing System (MTS) in this report. The hydraulic actuator has a force rating of 500 kN and a stroke (displacement) length of 150 mm. It includes an LVDT which measures the displacement of the actuator. Servovalves regulate the amount of hydraulic fluid to and from the hydraulic actuator, as well as the speed and direction of piston rod movement. The differential pressure across the piston forces the piston rod to move.

3.2.2 Transducers

The transducers used include the force transducer, an internal linear variable differential transformer (LVDT) located in the actuator and two external LVDTs. The force transducer (also called load cell or force sensor) with a load capacity of 500 kN was used to measure the amount of compression applied to the ballast sample. Non-linearity of the load cell was 0.15 % of the full scale and hysteresis was 0.2 % of full scale. The calibration of the actuator LVDT was done after setting up the load unit. Two external HBM WA/50 mm-L plungers were used to measure the displacement of the sleeper. They were connected to the load frame controller which recorded the analog signal inputs.

3.2.3 Tekscan Pressure Mats

Tekscan pressure mats were used to record the vertical and lateral stresses during the cyclic loading of the ballast layer in the large steel box. The dimensions of each pressure mat were 500 × 500 mm. Three pressure mats (A, B and C) were used: mats A and B were placed at the bottom of the box, while mat C was placed against the gate. The pressure mats were equilibrated to compensate for areas on the sensor that are less responsive in relation to higher responsive areas.

Figure 3-6: Load Unit (MTS) and components

3.2.4 Analysis Tools

A MATLAB code was written to extract upper and lower bands of deflection and axial load data to be used for further analysis in a spreadsheet. Sigmaplot software was used for data filtering and smoothing as well as plotting graphs. Tekscan Industrial Sensing (*I-Scan*) software was used to analyse the recorded pressure data.

3.3 EXPERIMENTAL SETUP AND PROCEDURES

This section focuses on characterising and modelling of the loading pattern imposed by a typical set of train wheels on a sleeper. Since this experiment seeked to develop a suitable loading condition for ballast box tests and investigate the effect of lateral confinement on key response elements and behaviour of the ballast layer, two experimental setups were considered, namely Setup 1 and Setup 2. Additionally, the experimental procedure for Setup 1 and Setup 2 are provided in this section.

The experiment for Setup 1 was concerned with developing a suitable loading pattern for laboratory box tests with the boundary conditions remaining constant (fully confined). The experiment for Setup 2 was concerned with altering the boundary conditions (decreasing the lateral confinement) of a box test to investigate the effects on key elements of the ballast response such as settlement, stiffness, modulus and ballast breakage.

3.3.1 Characterization and Modelling of the Field Loading Pattern

A typical field loading pulse (pattern) at the rail seat, in terms of load-time relationship, was recorded by Sadeghi (2008) with a wheel spacing of 1800 mm as discussed in Section 2.2.4 (Figure 2-6). Comparing the shape of this load pulse with the stress pulse obtained from in-situ pressure plate readings at the subballast layer, recorded by Gräbe et al. (2005) (Figure 2-7) with a wagon wheel spacing of 1830 mm, reveals some similarities in the pulse shapes – especially at the upper region. The stress pulse recorded by Gräbe et al. (2005) was generated under a 4 axle wagon configuration. The stress pulse shape presented by Gräbe et al. (2005) was used as a reference because the focus of this experiment was on replicating the loading pulse of a 4-axle train configuration (South African Coal Line) in laboratory box tests. Hence, the field loading pulse used for this experiment takes the shape of the stress pulse at the subballast (Figure 2-7). Multiplying the stress pulse by an influence area (which is constant) would produce the desired load pulse - which is similar to the load pulse recorded by Sadeghi (2008). Although wheel load data from strain gauges were readily available, the load on the ballast was assumed to be equivalent to the rail seat load due to the load distribution. Therefore, for all experiments conducted, a maximum load equal to the rail seat load was used. Table 3-2 shows more track details on the field studies conducted.

Table 3-2: Comparison of track details from field studies

Track details	Gräbe et al. (2005)	Sadeghi (2008)
Track gauge (mm)	1065	1435
Rail (kg/m)	60	UIC 60
Sleeper type	PY concrete	B70 pre-stressed concrete
Sleeper spacing (mm)	650	760
Ballast thickness (mm)	300	300
Passing speed (km/h)	40 – 50	40
Axle load (ton/axle)	20/26	22.5
Wheel spacing (mm)	1830	1800

To convert the stress pulse values to rail seat loads, the equivalent force, f_n from the in-situ pressure plate was calculated by multiplying the pressure plate readings, σ_n by the circular area of the pressure plate, a (Equation 21):

$$f_n = \sigma_n \times a \tag{21}$$

where n is the data point number and the pressure plate radius is 30 cm.

To obtain the field loading pattern (load-time relationship) as shown in Figure 3-7, the ratio of maximum rail seat load (q_r) to maximum equivalent force ($\max(f_n)$) was multiplied to each f_n value. The maximum rail seat load (q_r) was obtained by multiplying the dynamic wheel load (P_{dyn}) by a load distribution factor of 0.5. The dynamic wheel load (P_{dyn}) was calculated using the dynamic impact factor developed by Eisenmann (1972) (Section 2.2.2). Table 3-3 provides a summary of the dynamic wheel load and maximum rail seat load (q_r) calculation. A maximum rail seat load of 92 kN was determined, using the load distribution model (Equation 8) of Sadeghi (2008) in Section 2.2.6.

Table 3-3: Summary of variables used to calculate the dynamic wheel load and maximum rail seat load (q_r)

Variable	Unit	Value
Axle load (heavy haul)	Tonnes	26
Static wheel load, P_{static}	kN	127.53
Vehicle speed, V	km/h	70
η		1.07
Track condition, δ		0.2
t		2
Dynamic Impact Factor, φ		1.429
Dynamic wheel load, P_{dyn}	kN	182.2
Sleeper spacing	mm	650
Load distribution factor	%	50.4
Maximum rail seat load, (q_r)	kN	92

The Field Loading pattern (Figure 3-7) was simplified to eliminate irregularities. The following aspects of the loading pattern were adjusted:

i. Wheel load magnitudes (peaks): an equal maximum wheel load of 92 kN was set for all four wheel loads represented by the loading pattern.
ii. Averaged load valleys between wheel loads were equal

iii. Wheel spacing: equal wheel spacing for a load cycle was assumed, with a negligible effect on the ballast material tested.

The average load valley was calculated as 55.2 kN. A relationship between load amplitude and load valley was established using a factor of 1.667. Therefore, for any minimum applied load (L_{min}) and load amplitude (L_{ampl}), the load valleys ($L_{valleys}$) between wheel load can be obtained using the following expression:

$$L_{valleys} = L_{min} + \frac{L_{ampl}}{1.667} \tag{22}$$

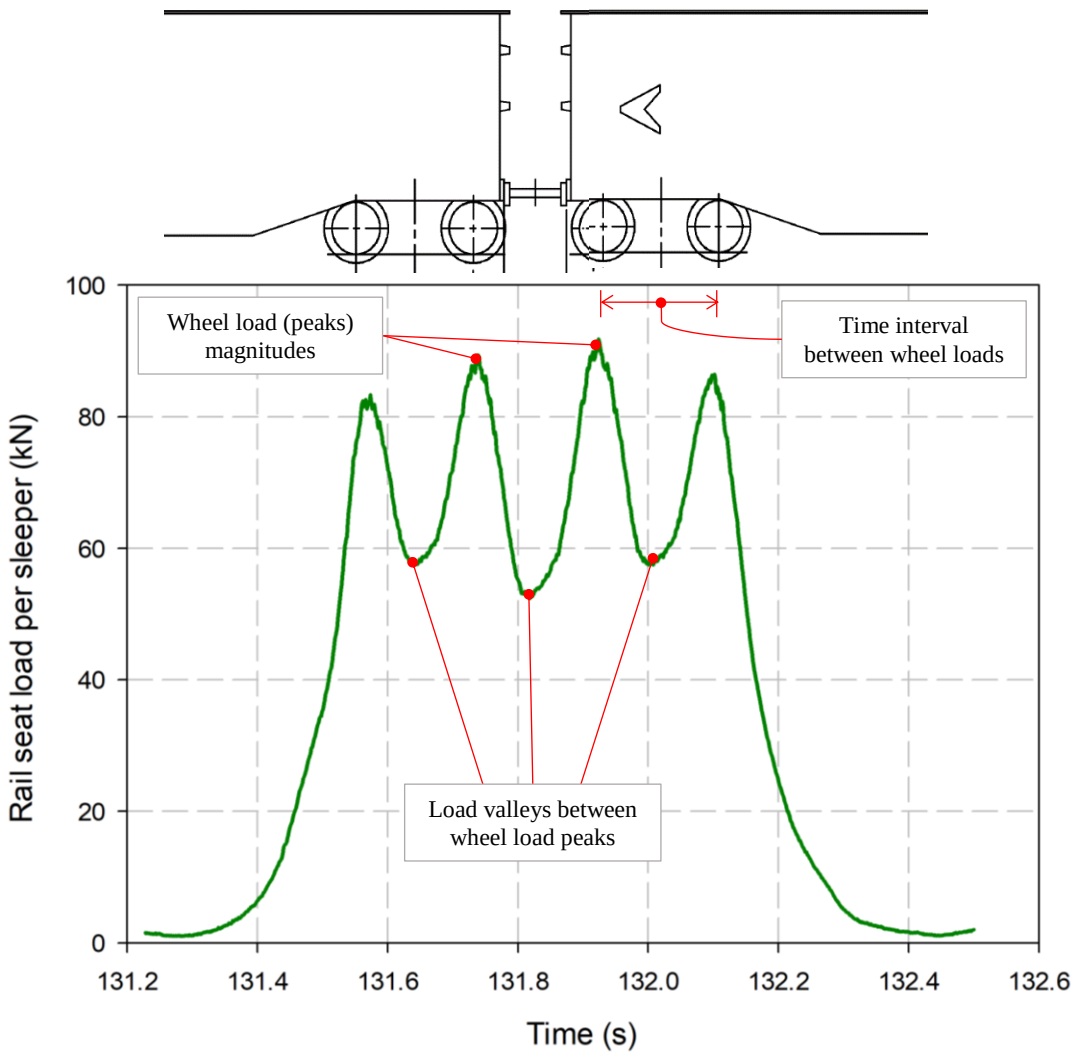

Figure 3-7: Loading pattern on rail seat from train axle loads experienced by a sleeper

Figure 3-8 shows the simplified field loading pattern, where the maximum rail seat load was rounded off to the nearest 10 kN (from 92 to 90 kN) and the load valleys with a value of 54 kN.

The ability of the hydraulic load frame to simulate this loading pattern was investigated by finding a suitable frequency and load amplitude to produce an appropriate loading shape. This was performed using the sleeper block and the 500 × 500 × 350 mm steel box containing ballast (300 mm depth) described in Section 3.3.2. Consequently, a scaled-down load was determined based on the theoretical stress at the ballast-sleeper interface under field conditions - which should be equal for both cases (field and laboratory conditions). The Axial Command values in the MTS load profile were adjusted to reduce the load amplitude required to achieve the desired simplified field loading pattern represented by the Axial Force values as shown in Figure 3-9. A scaled-down (rail seat) load amplitude and a minimum and maximum load of 10 kN, 5 kN and 15 kN respectively, at 2.5 Hz, were obtained after the Axial Command values were adjusted.

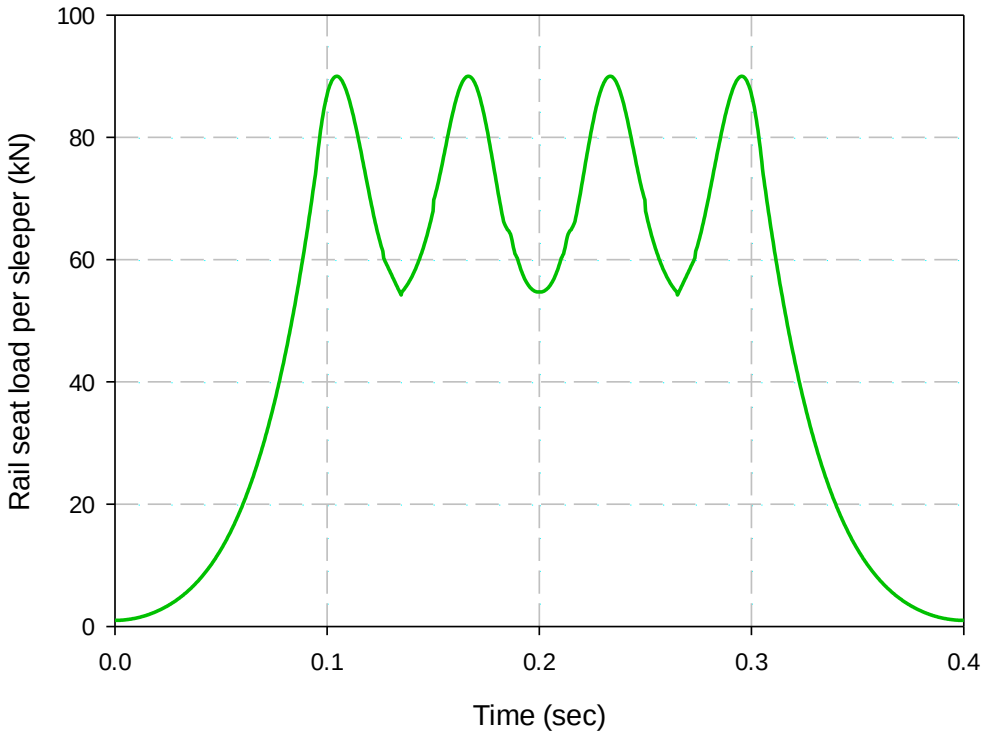

Figure 3-8: Simplified Field Loading pattern

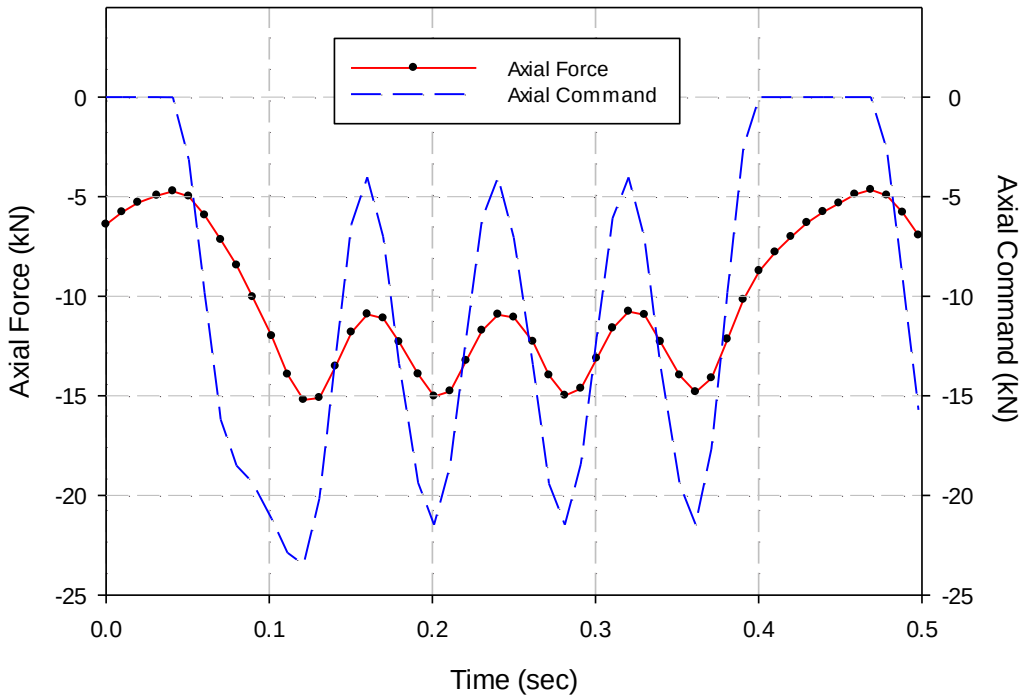

Figure 3-9: Simplified Field Loading pattern simulated by the MTS hydraulic actuator

3.3.2 Experimental Setup 1

The first experimental setup involved a scaled-down model of a railway track consisting of a steel box having internal dimensions 500 × 500 × 350 mm, with a thickness of 25 mm, and a sleeper block placed on ballast. Because several alternative loading patterns were investigated in this stage of the experiment, this setup was used to enable easy handling of the ballast material and sleeper block.

The schematic setup for compacting the ballast is shown in Figure 3-10. A 3 mm thick steel sheet (480 × 480 mm) was placed on the ballast. The 450 × 440 mm rigid compaction frame was constructed to ensure limited flexural movement. The rubber sheet placed between the ballast and steel sheet was used to reduce ballast abrasion during compaction. Prestick (a reusable adhesive) was placed between the LVDT plunger and steel plate to prevent unwanted vibration of the LVDT plunger. The rubber padding placed in between the actuator piston and the rigid frame was to prevent damage abrasion.

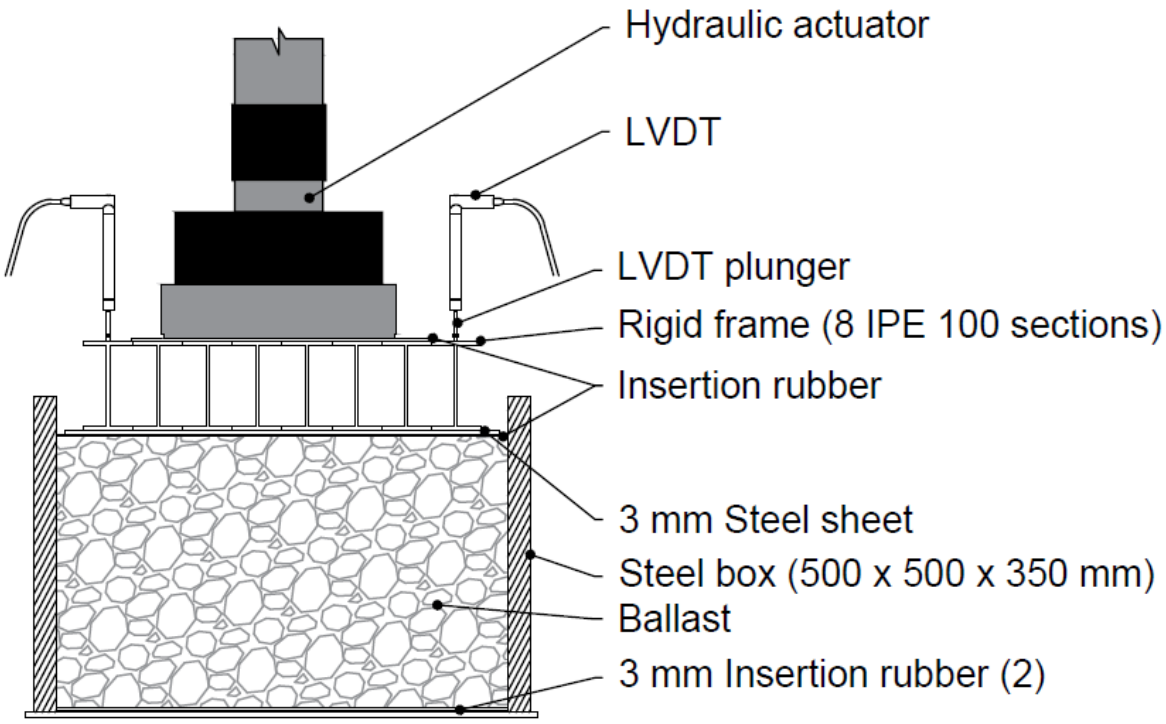

Figure 3-10: Cross section through the compaction setup for the small box test (Setup 1)

Track subgrade is commonly modelled as a semi-infinite elastic half space, characterised by a soft or stiff foundation. The insertion rubber sheets at the base of the box were used to replicate the slightly compressible effects of the subgrade layer. However, the contribution of the rubber sheets to achieve this subgrade behaviour is almost insignificant. Therefore, it is acknowledged that an artificial rigid subgrade provided by the load unit table in a box setup is always a limitation compared to the proper use of semi-infinite elastic half space. Figure 3-11 shows the final setup for the loading pattern experiment. After compaction, a High-Density Polyethylene (HDPE) Pandrol pad was fitted to the base of the sleeper block to prevent progressive sleeper wear. The cut-out section was at the middle of the PY sleeper length. The sleeper block dimensions were 228 × 185 × 170 mm. The LVDTs were supported by a setup consisting of magnetic bases and extension clamps. The boundary conditions for this test setup was fully confined.

Figure 3-11: Final experimental setup for Setup 1

3.3.3 Simulation of Loading Patterns through Setup 1

Comparison of alternative loading patterns to the Field Loading pattern was based on the rate of strain accumulation of the ballast layer. Other loading aspects that were compared were load cycle impulse and load frequency (rest periods). Impulse is the integral (area) of force plotted as a function of time. The Field loading (FL) pattern (Figure 3-8) was compared with the following loading patterns which can be simulated in the laboratory:

- Conventional haversine loading (Lab. L): Frequently used in the laboratory to simulate train loading, where a single load cycle represents four wheel loads.
- Impulse haversine loading (IHL): Modified conventional laboratory loading, where the impulse of the laboratory loading pattern (Lab. L) is equal to that of the Field loading pattern and a single load cycle represents four wheel loads.
- Haversine loading (HL): 4 loading pulses represent four wheel loads with the impulse of the loading equal to that of the Field loading pattern.
- Adjusted haversine loading (AHL): A modified version of the haversine loading (HL) where the load amplitude was reduced to closely match the ballast deformation caused by the Field loading pattern.

The terms haversine and sinusoidal are often used interchangeably. 'Sinusoidal' loading, often used in literature and research publications, refers to pure compression loading (with minimum and maximum stress levels) of the test sample. In other words, the waveform, which is sinusoidal in shape is used to describe the loading pattern. However, a typical sinusoidal

waveform might comprise both tension and compression regions. To clearly indicate that the loading type, though sinusoidal in shape, is fully compressional, the term ‘haversine’ loading is used, where the minimum load is greater than or equal to zero (compression).

Table 3-4 shows a summarized experimental procedure for Setup 1. Each sample was compacted in three layers following the rodding procedure outlined in the ASTM C29 standard. Each layer (100 mm) was rodded 25 times. Further compaction was conducted by applying a total of 25 000 haversine cyclic loads. The target ballast mass for each sample was 112.5 kg. A preload of 1 kN was applied. The compaction force applied (85 kN) was slightly greater than the calculated traffic load so that excess ballast deformation would not occur because of a higher load during train operation. All samples were compacted to a void ratio of 43 %. Data was captured at 100 Hz for all compaction stages. Table 3-5 compares each alternative loading pattern with the FL pattern, based on selected load properties. Graphical illustrations of these loading patterns are shown in Figure 3-12.

After compaction, each test sample was loaded (monotonically) to 20 kN. Table 3-5 provides the number of load applications for each loading pattern. 500 000 load cycles were applied on each sample. 100 000 load cycles were applied for each loading pattern. The number of load applications (Table 3-6) varied for each loading pattern depending on their characteristics. Rest periods were not included when transitioning to the next loading pattern as well as within the process of applying a loading pattern.

The effect of rest periods (bogie spacing and time interval between trains) on the permanent settlement of the ballast layer was only assessed on Sample B using the Field Loading pattern at 2.5 Hz. The number of cycles for each loading pattern (based on the duration rest period) was kept constant at 300 000 cycles.

Table 3-4: Test procedure for Setup 1

Sample	Cyclic Compaction			Loading Pattern					Rest Period (FL only)	
	Stage 1	Stage 2	Stage 3	Stage 1	Stage 2	Stage 3	Stage 4	Stage 5	Stage RP 1	Stage RP 2
A	40 kN at 5 Hz (5 000 cycles)	40 kN at 10 Hz (5 000 cycles)	85 kN at 10 Hz (15 000 cycles)	FL 1	Lab. L 1	FL 2	Lab. L 2	FL 3	-	-
B					IHL 1		IHL 2		0 to 0.8 seconds (0.4 second steps)	0.8 to 0 seconds (0.4 second steps)
C					HL 1		HL 2		-	-
D					AHL 1		AHL 2		-	-

Table 3-5: Alternative loading patterns compared with field loading based on selected parameters

Loading Pattern	Equal Impulse	Equal Frequency	Equal Load Amplitude	Load pulses per cycle
Lab. L	No	Yes	Yes	1
IHL	Yes	No	Yes	1
HL	Yes	No	Yes	4
AHL	Yes	No	No	4

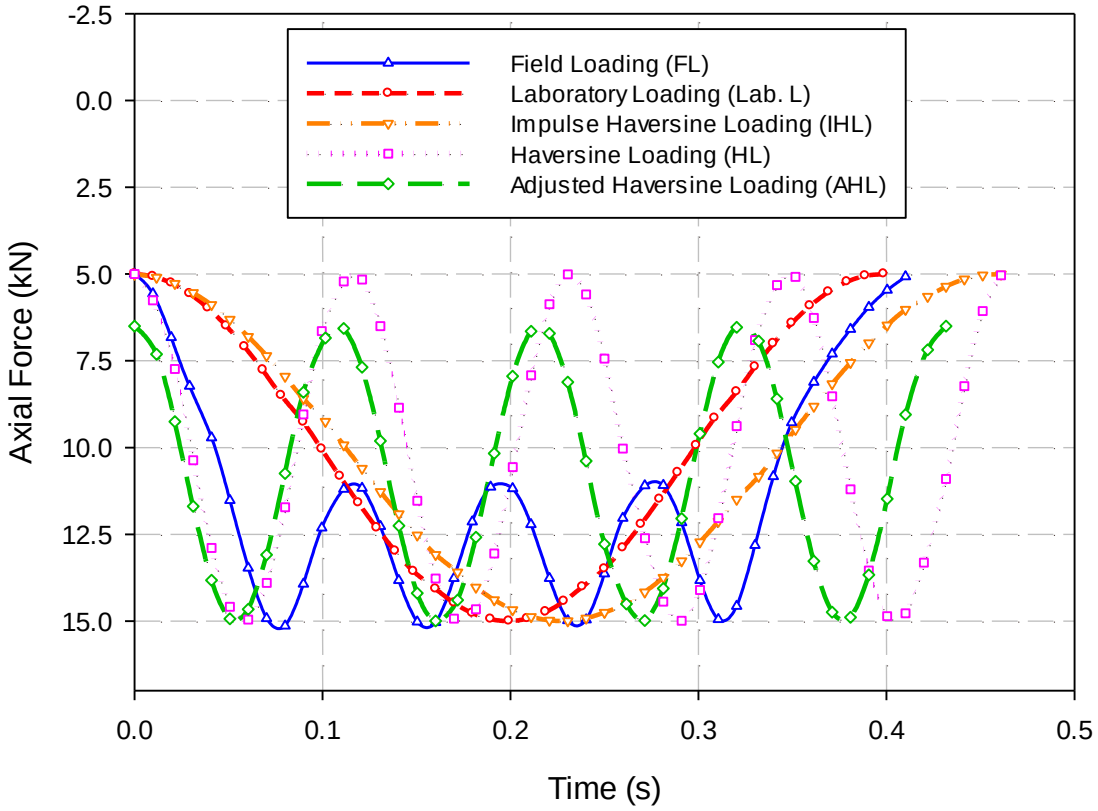

Figure 3-12: Shapes of the different Loading Patterns

Table 3-6: Number of load applications (pulses) for each loading pattern

Sample	Loading Patterns	Number of load applications (pulses)				
		FL 1	Alt. Load 1	FL 2	Alt. Load 2	FL 3
A	FL + Lab. L	400 000	100 000	400 000	100 000	400 000
B	FL + IHL	400 000	100 000	400 000	100 000	400 000
C	FL + HL	400 000	400 000	400 000	400 000	400 000
D	FL + AHL	400 000	400 000	400 000	400 000	400 000

3.3.4 Experimental Setup 2

The second experimental setup involved a full-scale box test with an adjustable length to investigate the effect of lateral confinement on ballast response. The internal dimensions of the box were 1630 × 650 × 450 mm. A schematic illustration of the materials, measuring devices and equipment and their respective positions are shown in Figure 3-13.

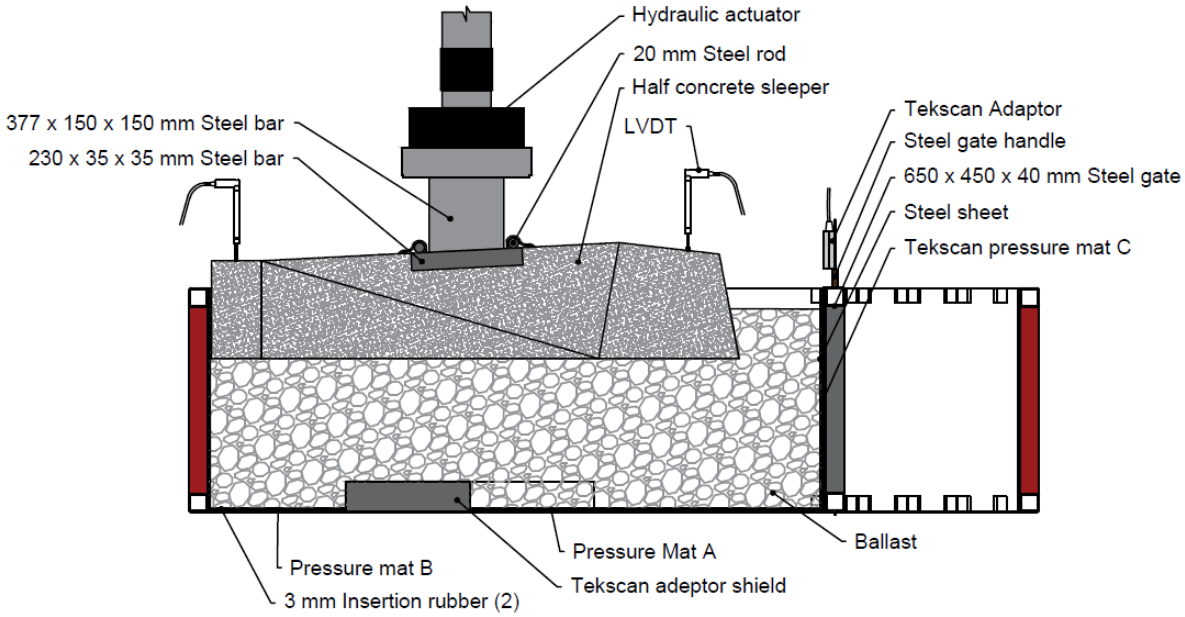

Figure 3-13: Schematic (cross section) illustration of experimental materials and instrumentation

The section of track simulated by this test setup is shown in Figure 3-14 (not to scale). Steel shields were made to protect the Tekscan handles placed at the base of the box. Rubber sheets at the base of the box provided protection for the pressure mats against ballast penetration and emulated the compressibility of the subgrade layer in the field.

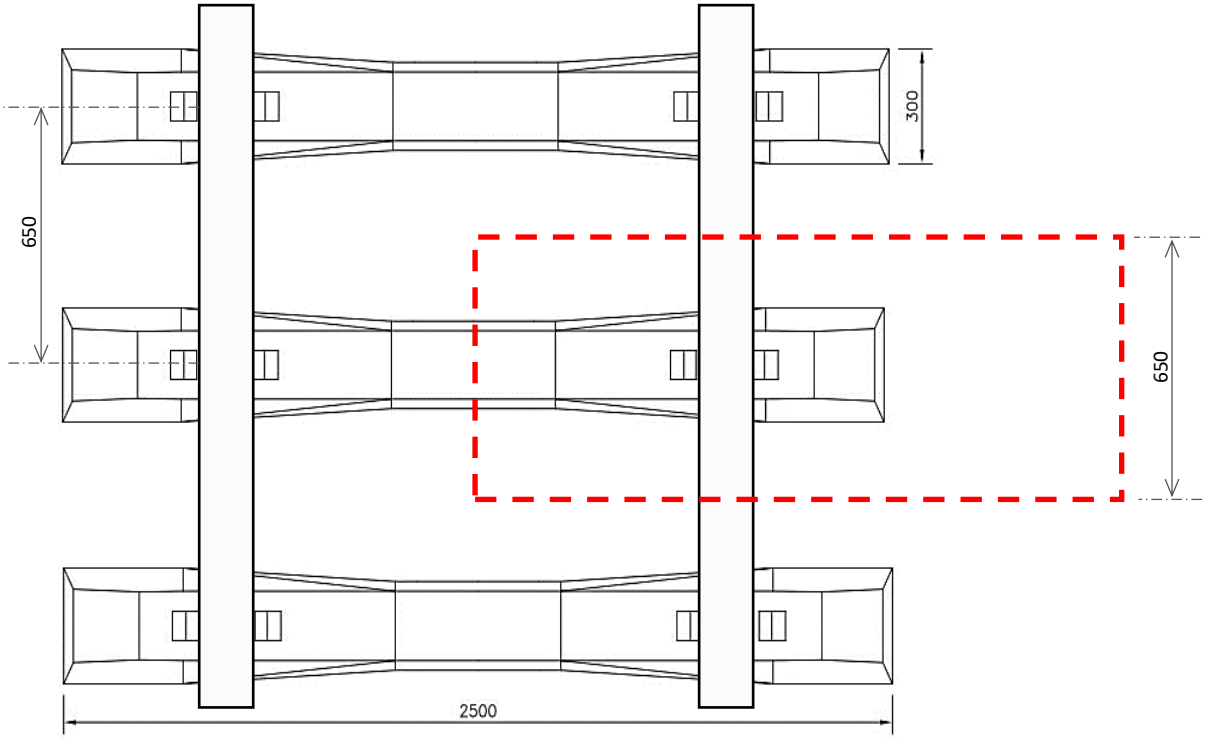

Figure 3-14: Track section represented by the full-scale adjustable steel box

The setup for ballast compaction involved a 5 mm thick steel sheet (1190 × 640 mm) and a steel frame made of IPE 100 sections welded along the flange to match the internal dimensions of the large steel box. Figure 3-15 shows the arrangement for the compaction of the ballast. For each sample, the gate was placed at a fully confined position to obtain relatively uniform ballast response after compaction. Ballast was placed around the half sleeper to the 400 mm mark, forming the crib ballast. Several different setups exist for this box test due to the length adjustment that simulated the effect of varying confinement on the ballast layer response. Figure 3-16 shows a typical setup for the different tests conducted for this experiment.

3.3.5 Influence of Confinement using Setup 2

The experimental procedures conducted using Setup 2 were concerned with the measurement of two parameters namely ballast breakage and ballast settlement. The steel box was designed to accommodate five levels of lateral confinement namely 100 % (fully confined), 75 %, 50 %, 25 %, and 0 % (with ballast shoulder) levels of lateral confinement. A new ballast sample was used for each level of confinement.

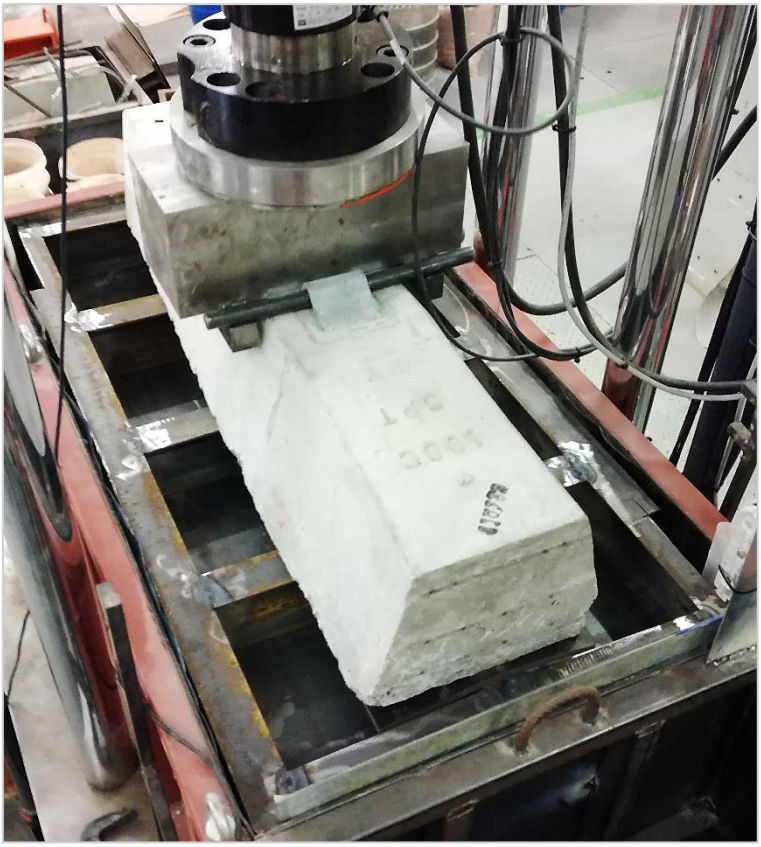

Figure 3-15: Large box compaction arrangement

Figure 3-16: Experimental setup for Setup 2

Ballast breakage was assessed at two locations in the ballast layer: at 100 mm and at 300 mm from the base of the box. 10 kg of ballast were painted with red and gold paint at 100 mm and 300 mm depths respectively, for each sample. Figure 3-17 shows the red painted ballast and their position in the box. To retain the surface friction of the ballast stones, the paint was applied sparingly using a brush as opposed to dipping them in paint. Sieve analyses were conducted on the painted ballast before placing in the box. The painted ballast at 300 mm was overlaid with normal ballast to prevent sleeper contact, since ballast breakage due particle interlocking was the focus. The painted ballast was placed in the region below the sleeper loaded area. Each sample was compacted in three layers following the rodding procedure outlined in the ASTM C29 standard. Each layer (100 mm) was rodded 55 times. Further compaction was conducted by applying 5 000 and 20 000 cyclic loads of 45 kN and 90 kN respectively, at 10 Hz.

For a 75 %, 50 %, 25 % and 0 % level of lateral confinement, a 2.5 mm steel sheet (630 × 460 mm) was placed against the gate prior to compaction to maintain the compacted state of the ballast layer at 100 % confinement. After compaction, the gate was removed and placed at the required confinement slot as shown in Figure 3-18. Figure 3-19 shows the steel sheet separating the compacted ballast and the ballast shoulder for 0 % lateral confinement.

The experimental procedures following compaction for the different levels of lateral confinement are described as follows:

- The sleeper was lowered into the box just above the compacted ballast. Crib ballast was placed around the sleeper and rod compacted.
- External LVDTs were placed at both ends of the half sleeper to record the permanent settlement of the ballast layer.
- A vertical monotonic load from 0 to 91 kN was applied to each sample. Subsequently, the AHL pattern was applied at 10 Hz with a load range from 2.5 to 91 kN.
- The number of wheel load applications were 1 300 000 cycles. Therefore, 325 000 load cycles were applied, with a load cycle representing 4 wheel loads, based on the wagon wheel configuration on the SA Coal Line.
- Vertical and lateral pressure readings were recorded at the start and after every 65 000 cycles to observe stress changes during cyclic loading.
- Sieve analyses were conducted on the painted ballast at 100 mm and 300 mm at the end of the cyclic loading.

Figure 3-17: Painted ballast (left) and painted ballast placed at 100 mm within the sleeper base area (right)

Figure 3-18: Gate placed at 50 % confinement slot

Figure 3-19: Steel plate separating the compacted ballast from the ballast shoulder during the 0 % lateral confinement setup

3.4 RAW DATA FROM TESTS

This section shows selected raw data extracted after each test. Figure 3-20 shows the axial force against time plotted for the first 5 seconds of Sample C - FL and HL tests. For the same test, Figure 3-21 shows the LVDT 1 and 2 output data. The first frame of Pressure Mats A and C (lateral) for a 100 % confinement at 95 000 load cycles are shown in Figure 3-22 and Figure 3-23 respectively.

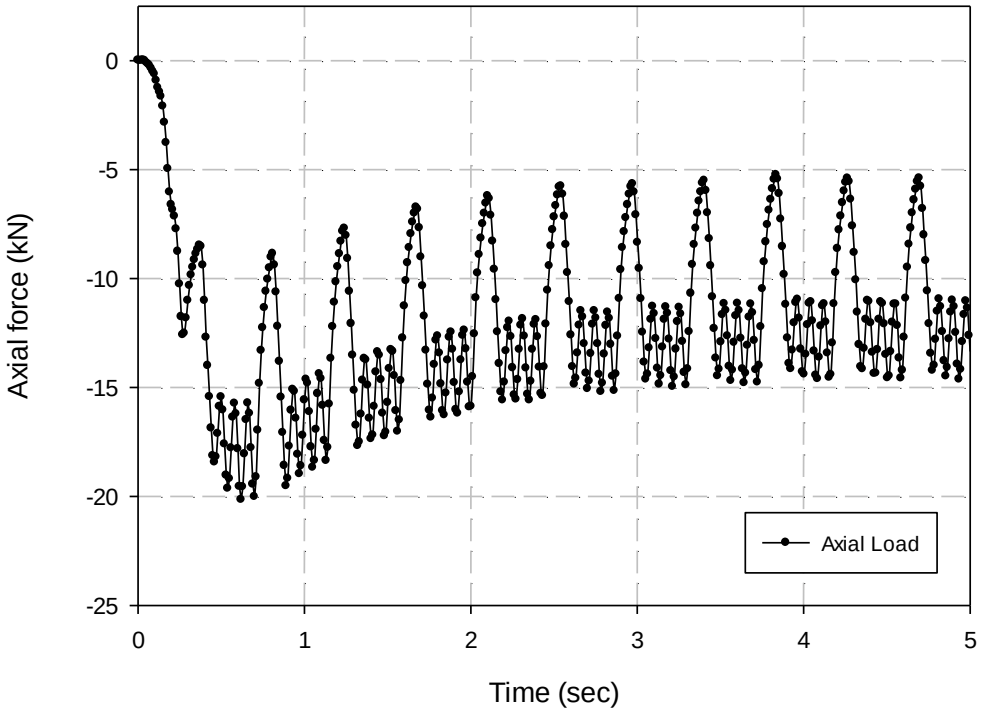

Figure 3-20: Raw data - Axial force versus time

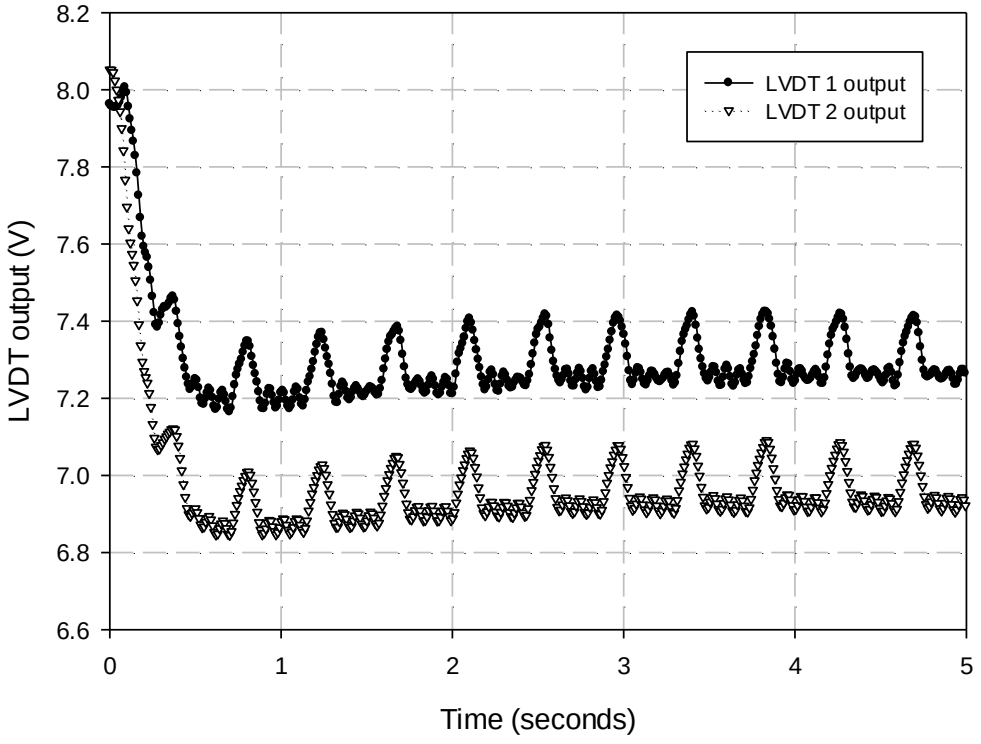

Figure 3-21: Raw data - LVDT output versus time

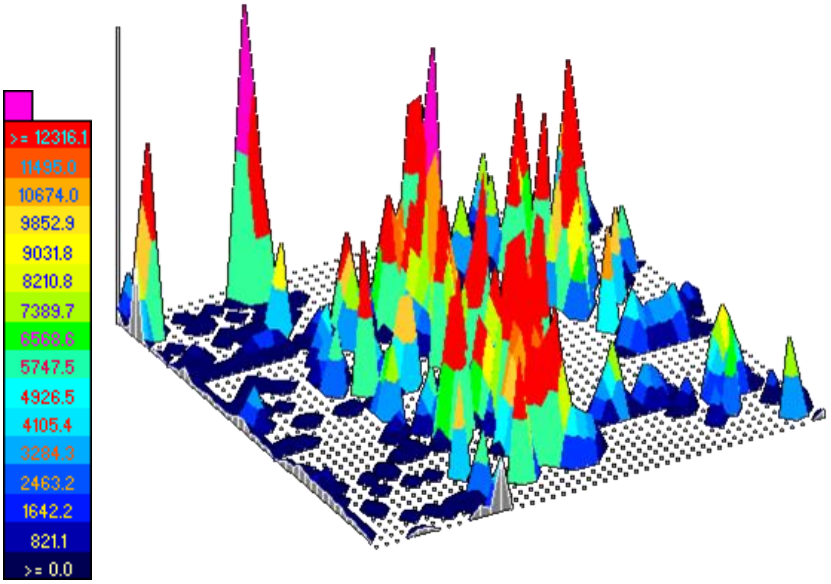

Figure 3-22: Stress contours on Mat A (100 % lateral confinement) at 380 000 load applications

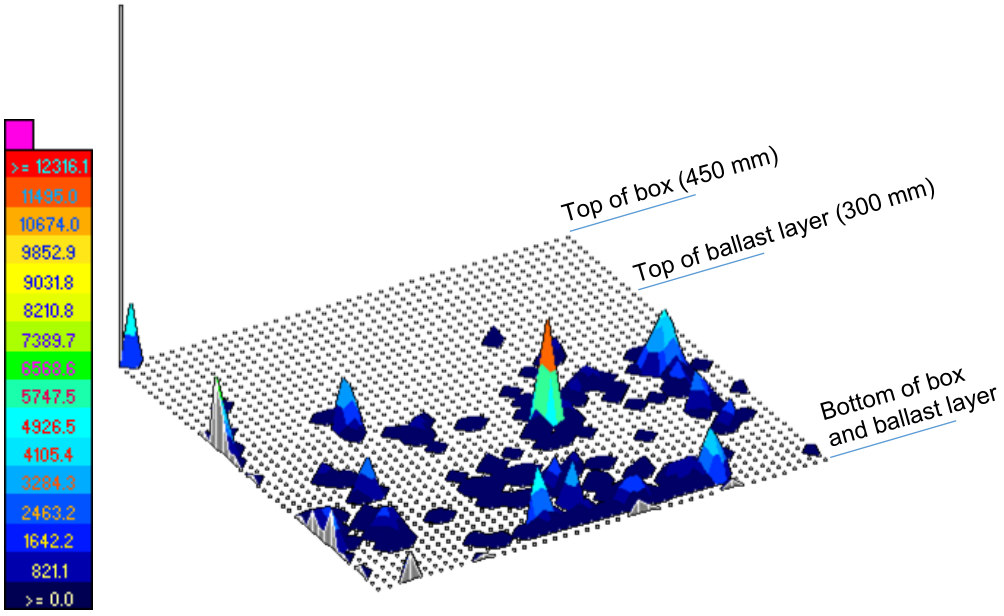

Figure 3-23: Stress contours on Mat C (100 % lateral confinement) at 380 000 load applications

4 ANALYSIS AND DISCUSSION

The analysis and discussion of experimental results are divided into three subsections, namely loading pattern results, boundary condition results and ballast layer stress results. The subsection on loading pattern compares the response of each ballast sample after compaction. It also compares the rate of ballast strain accumulation during the different loading patterns. The subsection on boundary conditions compares the ballast permanent settlement and ballast breakage at different levels of lateral confinement. The subsection on ballast layer stress discusses the stress changes along different levels of lateral confinement.

4.1 LOADING PATTERN RESULTS

The response of each ballast sample during compaction and the rate of strain accumulation obtained from different loading patterns are compared and discussed in this section. Table 3-4 shows a summary of the loading procedures performed using the small steel box (Setup 1). The deformation behaviour that resulted from the Field loading (FL) pattern was compared with the behaviour that resulted from following loading patterns: Laboratory Loading (Lab. L), Impulse Haversine Loading (IHL), Haversine Loading (HL), and Adjusted Haversine Loading (AHL).

4.1.1 Ballast Compaction

Figure 4-1 below shows ballast settlement with number of cycles for each ballast sample. The conventional (laboratory) haversine loading was used to compact all test samples. Rapid settlement occurred within the first 10 cycles as shown in Figure 4-2 due to the rearrangement of ballast as cyclic loads of 40 kN were applied. The rate of settlement could have been increased by increasing the load, however, this would have resulted in undesired ballast breakage in the compaction stage. The effect of an increase in frequency on strain accumulation was not clearly identified, as the number of cycles were not sufficient to compare the rate of strain accumulation within the first 10 000 cycles. At 10 000 cycles, the compactive force was increased to 85 kN which caused rapid increase in permanent strain and possible particle breakage (Figure 4-1). There was a continuous decrease in the rate of permanent strain with increasing number of cycles thereafter. The stress applied to the ballast sample during compaction between 10 000 – 20 000 cycles was equivalent to the stress at the sleeper-ballast interface (below the rail seat) induced by a 13-tonne wheel load.

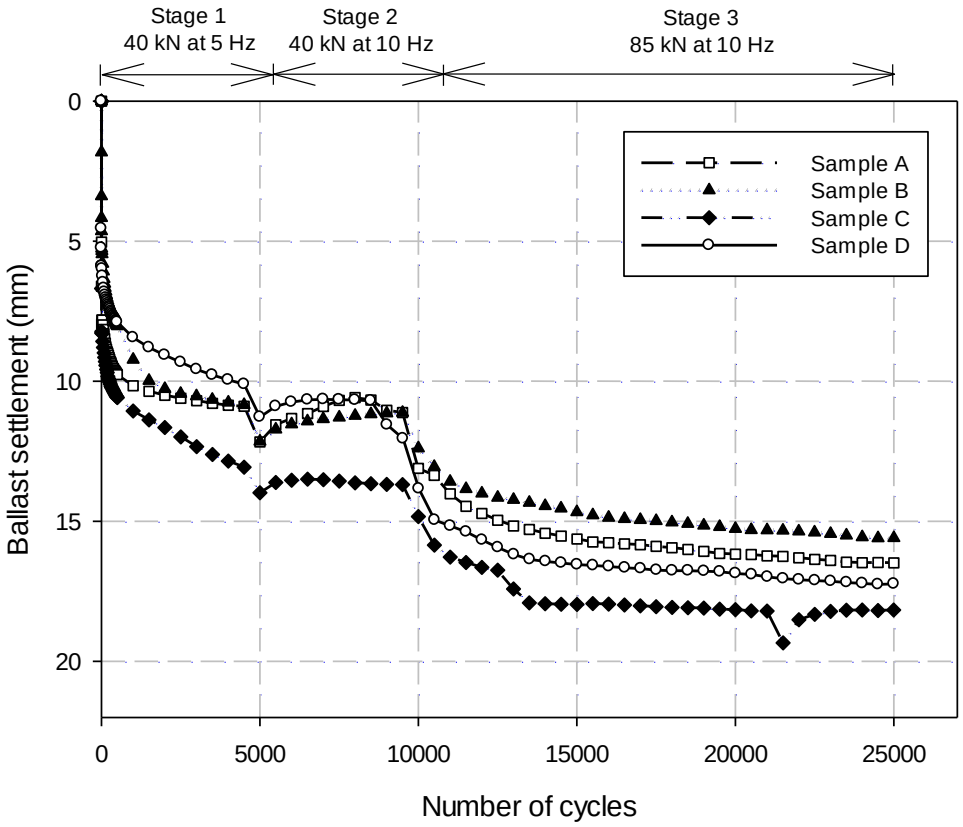

Figure 4-1: Permanent settlement of ballast for each sample during three stages of compaction

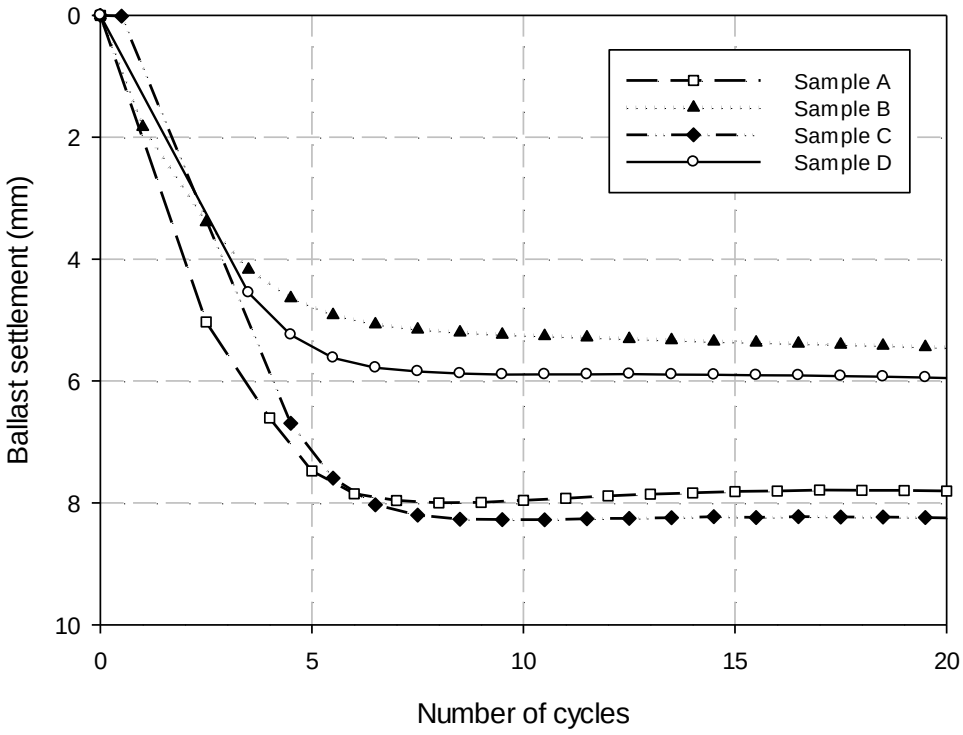

Figure 4-2: Rapid ballast settlement during the first 10 cycles for each ballast sample

Ballast stiffness per cycle, as shown in Figure 4-3, was calculated for each sample using Equation 20 (Section 2.11.1) while the ballast modulus was calculated as the ratio of applied stress to ballast strain. There was a general increase in stiffness with the number of cycles for each test sample. Differences in stiffness might be due to particle sizes and gradation as well as particle arrangement. Uneven stiffness paths occurred at transitions between increase in load frequencies and applied vertical load. Similar increases in ballast modulus was observed for every load cycle.

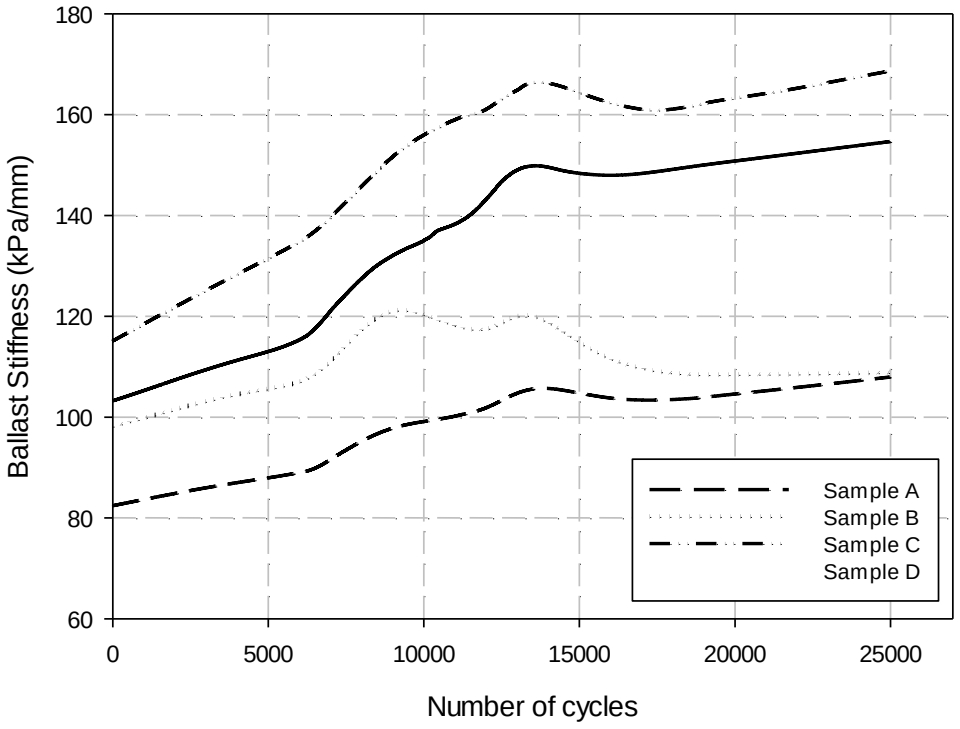

Figure 4-3: Ballast stiffness per cycle for each ballast sample

Settlement, stiffness and modulus values for each ballast sample after compaction are shown in Table 4-1. It is important to note that although equal loading parameters and frequency values were applied to each ballast sample, their final responses differed. Factors affecting the changes in ballast response include varying particle shape and sizes and particle arrangement, among others.

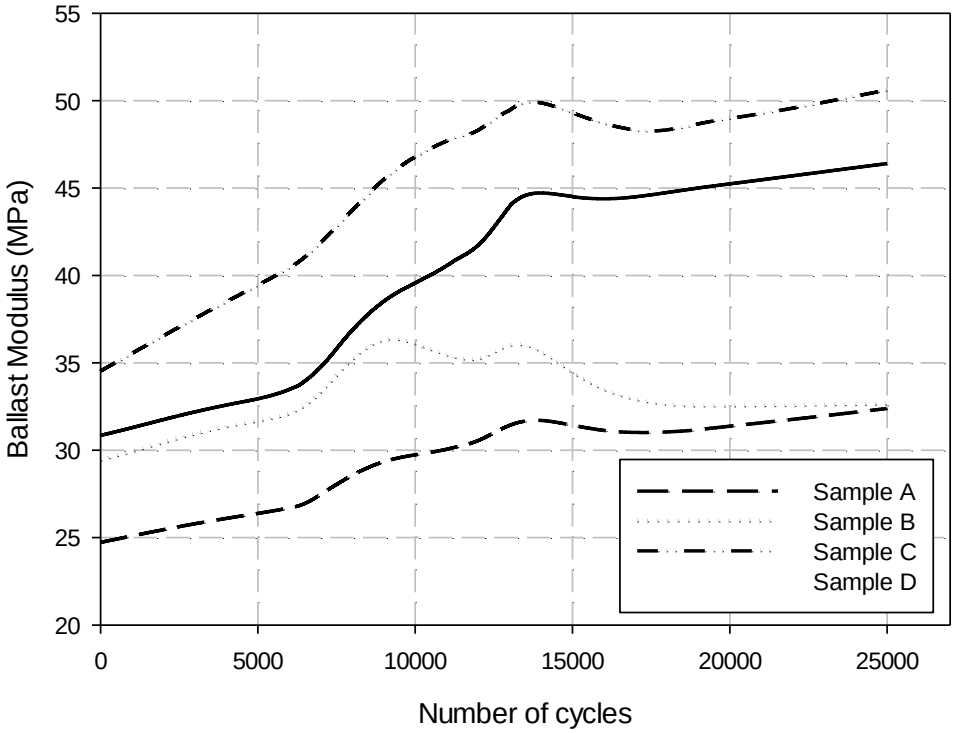

Figure 4-4: Ballast modulus per cycle for each ballast sample

Table 4-1: Summary of ballast sample response after compaction

Sample	Settlement (mm)	Stiffness (kPa/mm)	Modulus (MPa)
A	16.5	108.0	32.4
B	15.6	108.8	32.6
C	18.2	168.7	50.6
D	17.2	154.7	46.4

Despite the extreme care taken to produce ballast samples for the laboratory testing with similar stiffness (or modulus) after compaction, it is clear from the results that even though the compaction resulted in similar total settlement, the final stiffness values differed too much to regard the samples as identical for comparative testing. Instead of applying one loading pattern to each sample, it was therefore decided to alternate two loading patterns on the same sample for comparison. As a result, the FL pattern was alternated with one of the four Laboratory patterns on each individual sample. This procedure enabled accurate comparisons between the settlement and strain behaviour resulting from the different loading patterns.

4.1.2 Comparison of Loading Patterns

This section compares elements of each loading pattern, the rate of ballast axial strain due to varying loading patterns and ballast modulus initiated by each loading pattern to obtain a laboratory loading pattern that is a suitable representation of field loading conditions. Using Table 3-5 as a reference, Table 4-2 shows the properties of the loading patterns used in this study. Figure 4-5 shows the ballast deflection bowls associated with each loading pattern. It was expected that the AHL pattern would produce the smallest deflection due to a reduced load amplitude. Maximum deflections of other loading patterns differ due to varying sample properties such as stiffness.

Table 4-2: Properties of various Loading Patterns

Property	FL	Lab. L	IHL	HL	AHL
Load amplitude (kN)	10	10	10	10	8.5
Impulse (kN)	4.63	4	4.62	4.62	4.63
Frequency (Hz)	2.5	2.51	2.17	2.17	2.32
Maximum deflection (mm)	0.46	0.41	0.42	0.37	0.33
Deflection bowl area (mm s)	0.14	0.08	0.10	0.08	0.07

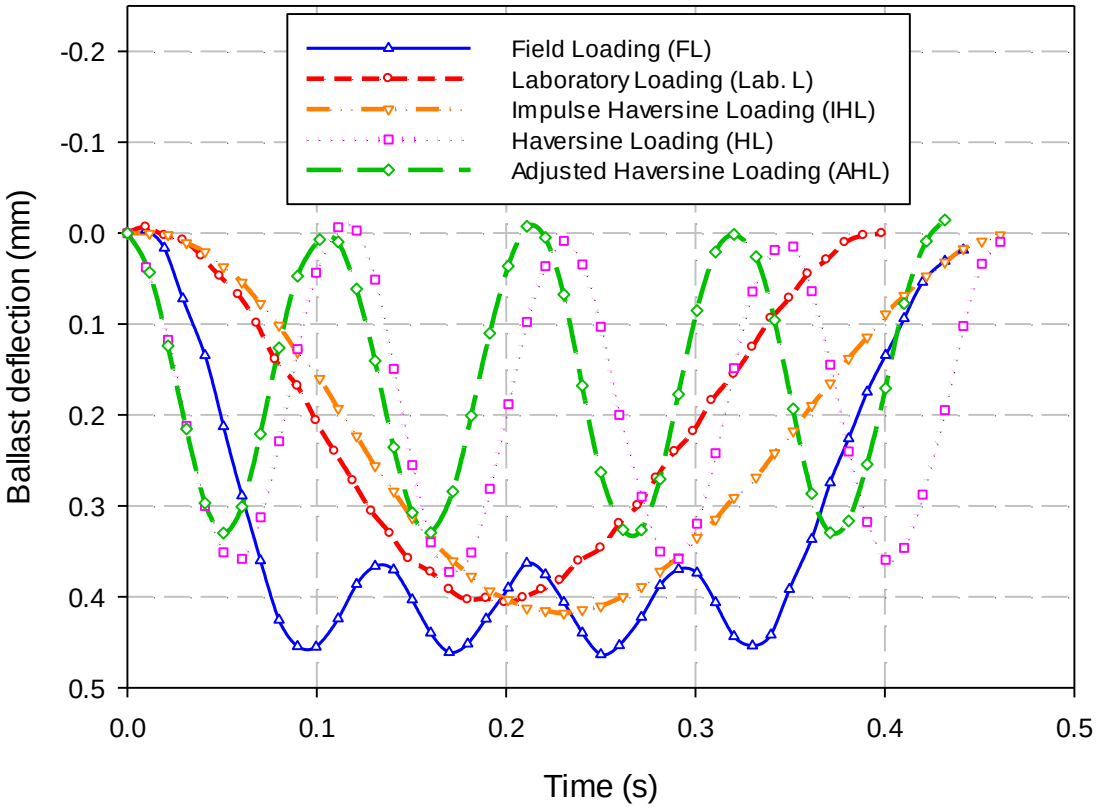

Figure 4-5: Deflection bowls for each Loading Pattern

4.1.3 Ballast Layer Axial Strain

Figure 4-6 shows the percentage strain of each ballast sample subjected to alternating loading patterns of FL and the other chosen loading pattern. This loading method was used to assess the rate of strain accumulation induced by each loading pattern. Although each loading pattern could have been performed on individual test samples, these test samples would not have similar ballast responses after compaction. The shakedown period to reach linearity occurred between 0 and 100 000 cycles which agrees with studies conducted by Lackenby et al. (2007) and Kashani et al. (2017). Samples A and B exhibited similar strain behaviour comprising of a significant increase in the rate of strain accumulation after 400 000 cycles. Possible reasons for this observation are:

- Both the Lab. L and IHL patterns do not have the same quantity of load pulses per cycle when compared to the FL pattern.
- Particle rearrangement or ballast breakage.

Considering the degradation zones established by Indraratna et al. (2005), the zone that best describes the deformation behaviour of each ballast sample is the compressive stable degradation zone (CSDZ). In this zone, the particle movements are restricted with a high

coordination number due to the high level of confinement. Typical forms of breakage in this degradation zone include attrition of asperities and corner breakage.

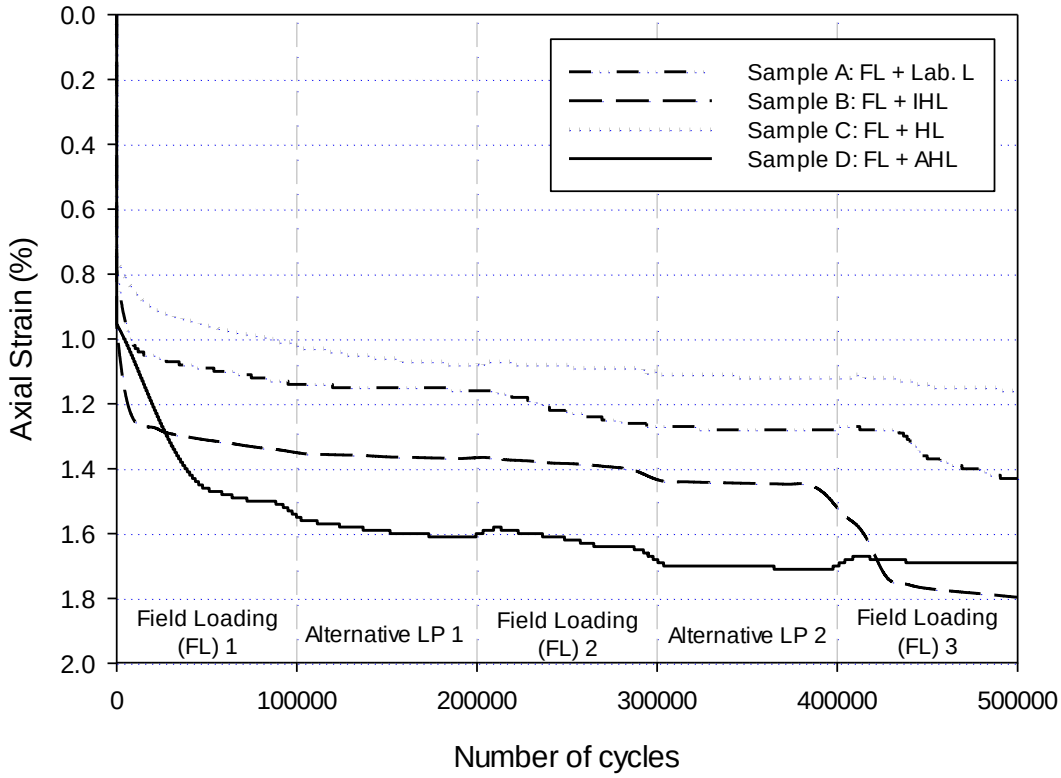

Figure 4-6: Permanent strain accumulation for each sample during alternating loading patterns

To compare the rates of strain accumulation between the FL pattern and each alternative loading pattern after 100 000 cycles, linear relationships between the percentage axial strain and traffic in million gross tonnes (MGT) were expressed. The number of cycles can be expressed in terms of MGT using Equation 7 (Section 2.2.3) presented by Selig and Waters (1994). Therefore, every 100 000 load cycles of an equivalent 26 tonne axle load represent 10.4 MGT and 500 000 load cycles represent 52 MGT. Plots of percentage axial strain against traffic for every 10.4 MGT were created to observe the strain accumulation rate between the FL and alternative loading patterns in Figure 4-7 to Figure 4-10, and are discussed individually in the sections which follow.

Sample A – Field Loading (FL) and Laboratory Loading (Lab. L) patterns

Common properties of the FL and Lab. L patterns include load amplitude and frequency. Dissimilar properties of these loading patterns include impulse and number of load pulses per

load cycle (Table 3-5). The Lab. L pattern is a generic sinusoidal waveform used to simulate train loading on ballast in the laboratory.

Figure 4-7 shows the plots of percentage axial strains of the ballast layer induced by the FL and Lab. L patterns. Two pairs of axial strains were compared, namely: Lab. L 1 - FL 2 and Lab. L 2 – FL 3. Linear regression lines were fitted to each plot to obtain the rate of strain accumulation (denoted as m - percentage strain/MGT). For plots indicating possible particle breakage or rearrangement (such as plot FL 3 after 4 MGT), the rate of strain accumulation for the gradual portion after breakage was computed.

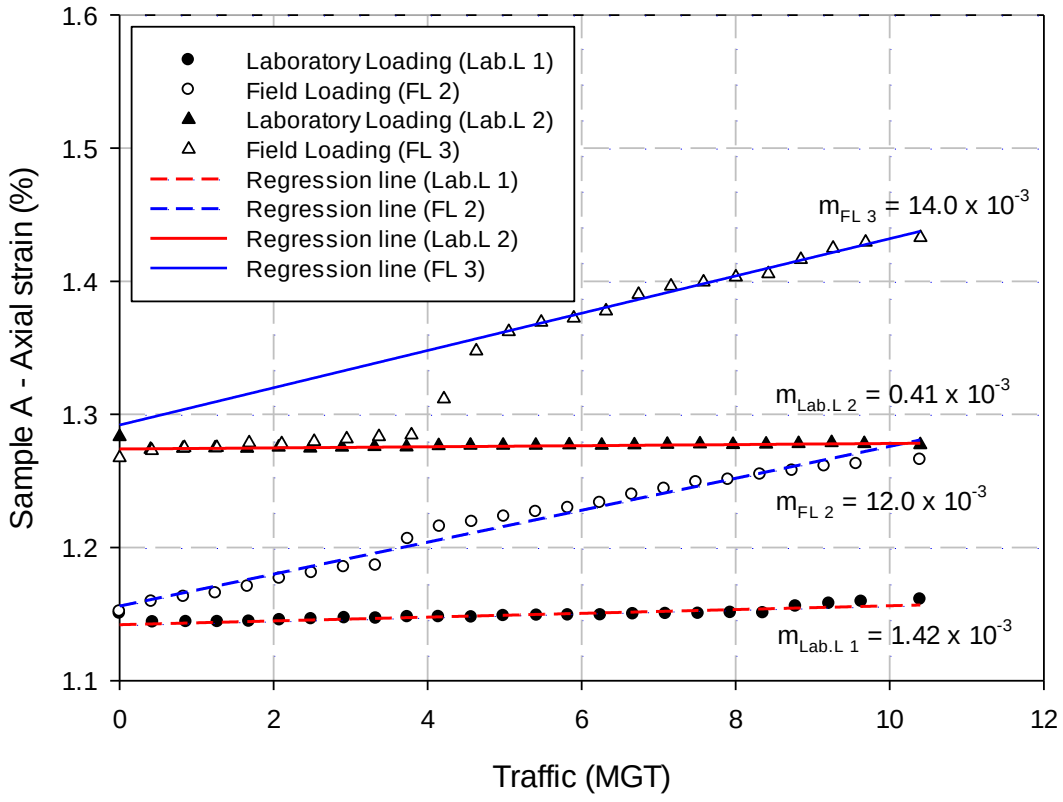

Figure 4-7: Axial strain accumulation of ballast layer (Sample A) during alternating loading patterns of FL and Lab. L

It is expected that the rate of strain accumulation would decrease with traffic (number of cycles) for ideal situations except in the event of weak spots in a track structure. However, there is a significant increase in strain rate after the transition from Lab. L to FL for both pairs of axial strain as FL yields a higher plastic strain of the ballast layer than Lab. L. It is evident that the Lab. L pattern is not capable of reproducing the strain under field conditions on the ballast layer.

As mentioned earlier, the rapid plastic strain between 4 and 5 MGT (FL 3) is possibly due to corner breakage and attrition of asperities or particle rearrangement. Aspects of the loading pattern influencing the rate of plastic strain are:

- Number of load pulses (or load applications): In this report, the number of load pulses refers to the number of load peaks within a load cycle as illustrated in Figure 3-7. Therefore, for a single load cycle, the FL pattern has 4 load pulses while the Lab. L pattern has 1 load pulse (which can also be referred as 1 load cycle). Therefore, the amount of plastic strain produced per FL load cycle is significantly more than the amount of plastic strain produced per Lab. L cycle.
- Load impulse: The influence of load impulse on the rate of ballast layer strain for this test sample is not clearly identifiable. However, a comparison of the Lab. L and IHL patterns is considered in Section 4.1.4.

Sample B – Field Loading (FL) and Impulse Haversine Loading (IHL) patterns

Common properties of the FL and IHL patterns include load amplitude and load impulse. Dissimilar properties of these loading patterns include frequency and number of load pulses per load cycle. IHL is a modified loading pattern from the Lab. L pattern where the load impulse of the Lab. L was increased to match the FL impulse per cycle.

Figure 4-8 shows the percentage axial strain plots of the ballast layer generated by the FL and IHL patterns. This sample experienced a high increase in strain due to possible particle breakage or rearrangement. The FL pattern applied more load pulses than the IHL pattern, therefore, the ballast layer deformed more under the FL pattern. The levelled off portion of the FL 3 plot (after 3 MGT) was used to compute the rate of plastic strain, m. Similar ballast strain behaviour is observed with Sample A (with the FL and Lab. L patterns - Figure 4-7). However, comparing the plastic strains induced by the IHL and Lab. L patterns, there is a notable increase in the rates of plastic strain due to an increase in load impulse (discussed in Section 4.1.4).

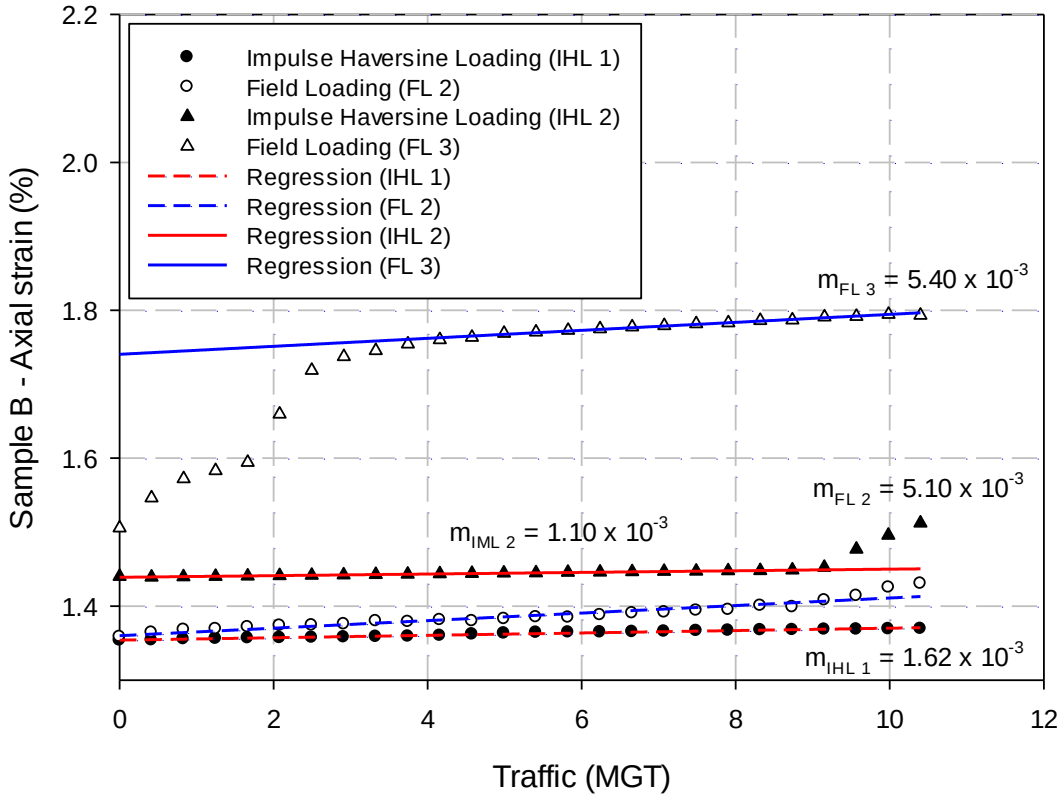

Figure 4-8: Axial strain accumulation of ballast layer (Sample B) during alternating loading patterns of FL and IHL

Sample C – Field Loading (FL) and Haversine Loading (HL) patterns

Common properties of the FL and HL patterns include load amplitude, load impulse and number of load pulses per cycle. A dissimilar property of these loading patterns is the load frequency. The HL pattern consists 4 load pulses per cycle. Each load pulse has equal load amplitude as in the case of the FL pattern.

Figure 4-9 shows percentage axial strain plots of the ballast layer generated by the FL and HL patterns. The HL pattern in the first pair caused a higher strain rate than the FL pattern. However, in the second pair, the strain rate caused by FL pattern was higher than the HL pattern due to possible particle breakage or rearrangement. The strain rate of FL 3 was computed after 4 MGTs. The frequency and load amplitude of intermediate load pulses per cycle differentiate these two loading patterns. It is important to note, however, that in a perfect scenario (i.e. absence of possible ballast breakage or rearrangement), the strain rate caused by the HL pattern marginally exceeds the strain rate caused by the FL pattern for the second pair. The driving factor for this behaviour is the effect of the additional load amplitude provided by the second and third load pulse in the HL pattern. This increases the stress level per cycle exhibited by the

HL pattern which generates more strain deformation than the FL pattern. Similar strain responses with these loading patterns were observed in preliminary tests.

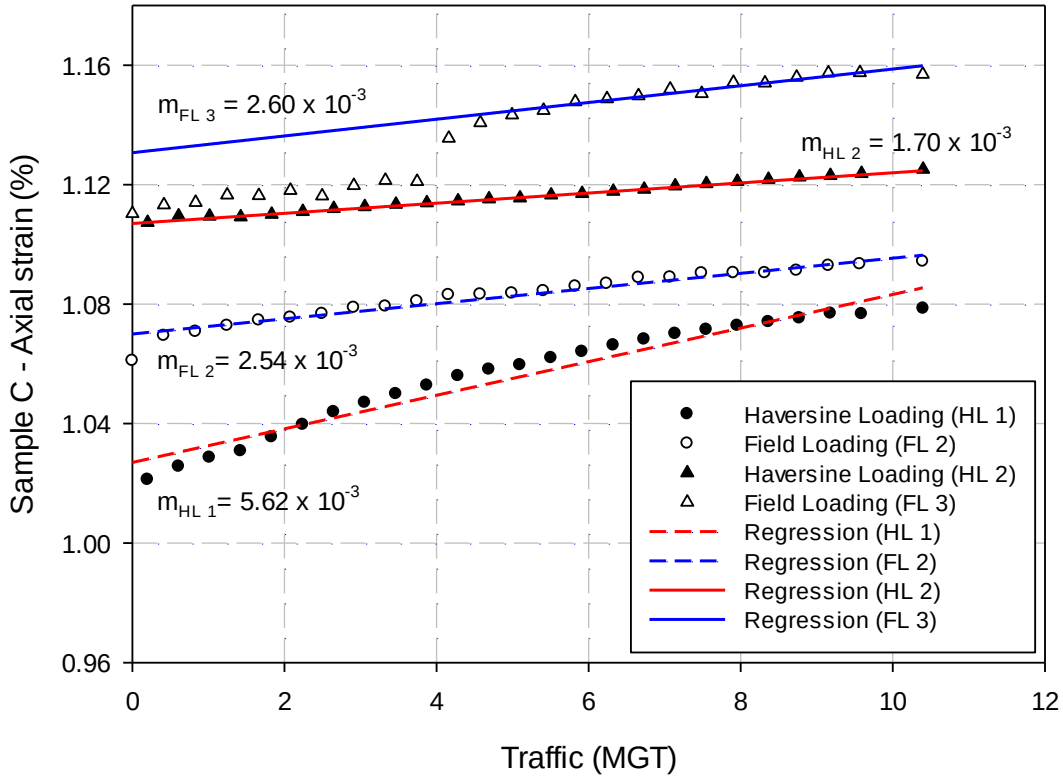

Figure 4-9: Axial strain accumulation of ballast layer (Sample C) during alternating loading patterns of FL and HL

Sample D – Field Loading (FL) and Adjusted Haversine Loading (AHL) patterns

Common properties of the FL and AHL patterns include load impulse and number of load pulses per cycle. Dissimilar properties of these loading patterns include load amplitude and frequency. The AHL pattern consists of 4 load pulses per cycle. After conducting several preliminary tests and comparing the rates of strain accumulation generated by FL and AHL under different load amplitudes of the AHL pattern, a final load amplitude of 8.5 kN was employed. The frequency of this loading pattern was determined based on the changes to the load amplitude and impulse.

Figure 4-10 shows the plots of percentage axial strain of the ballast layer generated by the FL and AHL patterns. Both pairs of plots have slight differences in the rates of axial strain, with a maximum strain difference of 2.2 % per MGT. The absence of a sudden increase in axial strain is possibly due to:

- the absence of ballast breakage or rearrangement, and

- Equal amounts of stress levels applied to the test sample which eliminate potential rearrangement or breakage of ballast particles.

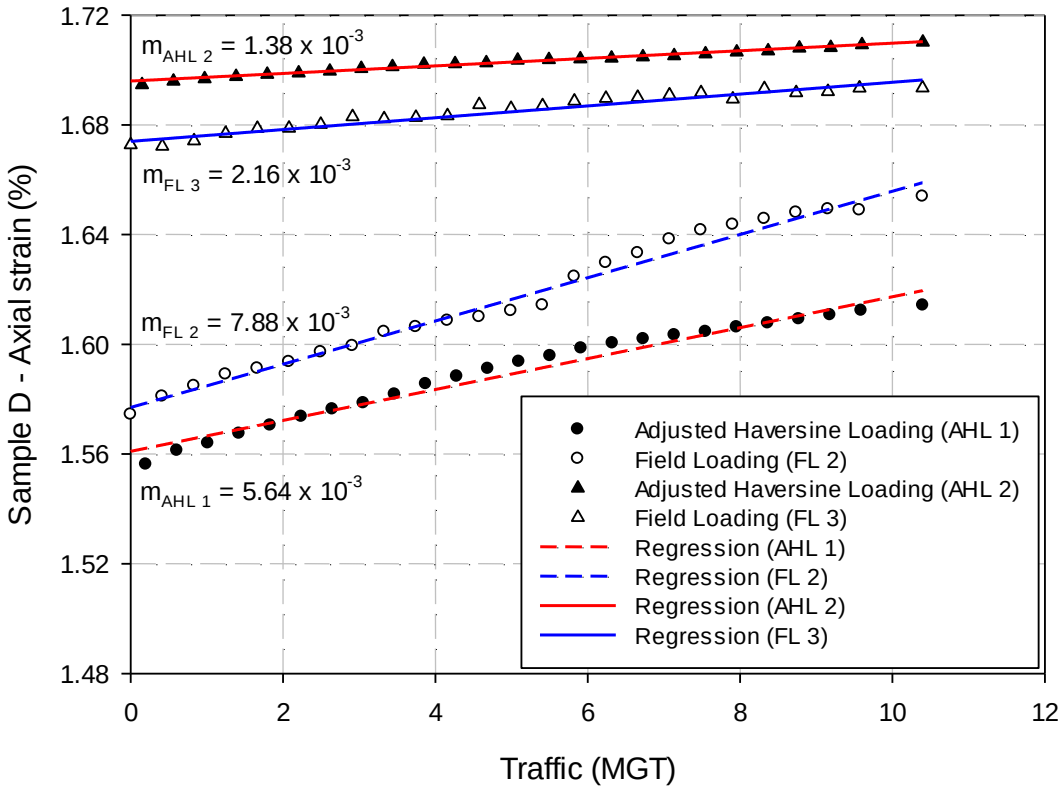

Figure 4-10: Axial strain accumulation of ballast layer (Sample D) during alternating loading patterns of FL and AHL

All the axial strain plots were zeroed to quantify the extent of axial strain after every 10 MGT. For each axial strain plot pair of the FL and alternative loading pattern, the difference in strain accumulation was computed. Figure 4-11 shows the percentage axial strain difference between the FL and alternative loading pattern after every10 MGT. The AHL pattern has the lowest strain difference while the Lab. L had the highest strain difference in relation to the axial strains induced by the FL pattern. Therefore, from the assessed loading patterns, the AHL pattern is the most appropriate loading pattern to be implemented for laboratory tests when considering axial ballast strain. Employing this loading pattern will produce accurate and realistic results to predict ballast layer behaviour and track structure response during field loading. The Lab. L pattern is therefore not a suitable loading pattern to be used in the laboratory when loading based on a 4-wheel train configuration. It is assumed that a major influence on the settlement trends of the ballast layer from these results can be associated with the rigid bottom (subgrade) of the box.

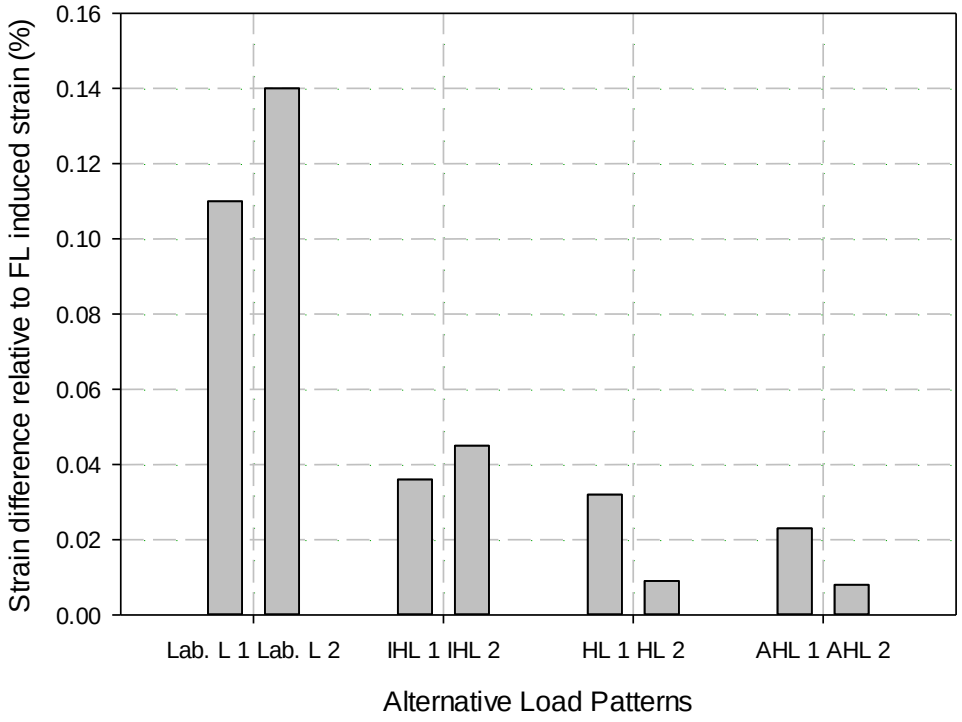

Figure 4-11: Difference in axial strain between the FL and alternative loading patterns after every 10 MGT

4.1.4 Effect of Load Impulse on Plastic Strain of Ballast Layer

Increasing the loaded area of the Lab. L pattern to match the FL pattern involved reducing the load frequency of a single Lab. L cycle while maintaining a constant load amplitude. Test results from Samples A and B were compared. The comparison of the strain rates resulting from these loading patterns is valid as the initial ballast layer response of each test sample after compaction were relatively similar.

Referring to Figure 4-11, the effect of load impulse is clearly observed from the decrease in strain difference between FL-Lab.L 1 and FL-IHL 1. Although there was a decrease in load frequency as characterised by the IHL pattern, it is not quite clear as to a possible reason for an increase in the rate of strain accumulation. However, it can be concluded that the loaded area of a loading pattern (or frequency) influences the rate of plastic strain accumulation.

4.1.5 Ballast Layer Modulus

There is a general increase in ballast layer modulus across ballast samples as shown in Figure 4-12. There are possible reasons that justify the rapid changes in moduli at loading transitions, these include:

- Specified command-based values in the profile which are read and simulated by the MTS to form the FL pattern as opposed to in-built control signals or parameters which perform predefined sinusoidal waveforms.
- The average maximum deflection of the FL pattern: the 4 deflection troughs generated by the FL pattern were averaged as well as the corresponding number of cycles and load values.
- Non-uniform loading of the FL pattern: At random load cycles, the minimum and maximum loads were less than 5 kN and greater than 15 kN, respectively. This also affected the average value of the 4 troughs of the deflection bowl.
- Rebound effect of the rigid bottom of the box could alter the ballast moduli as opposed to the absorbing nature of a semi-infinite half space.

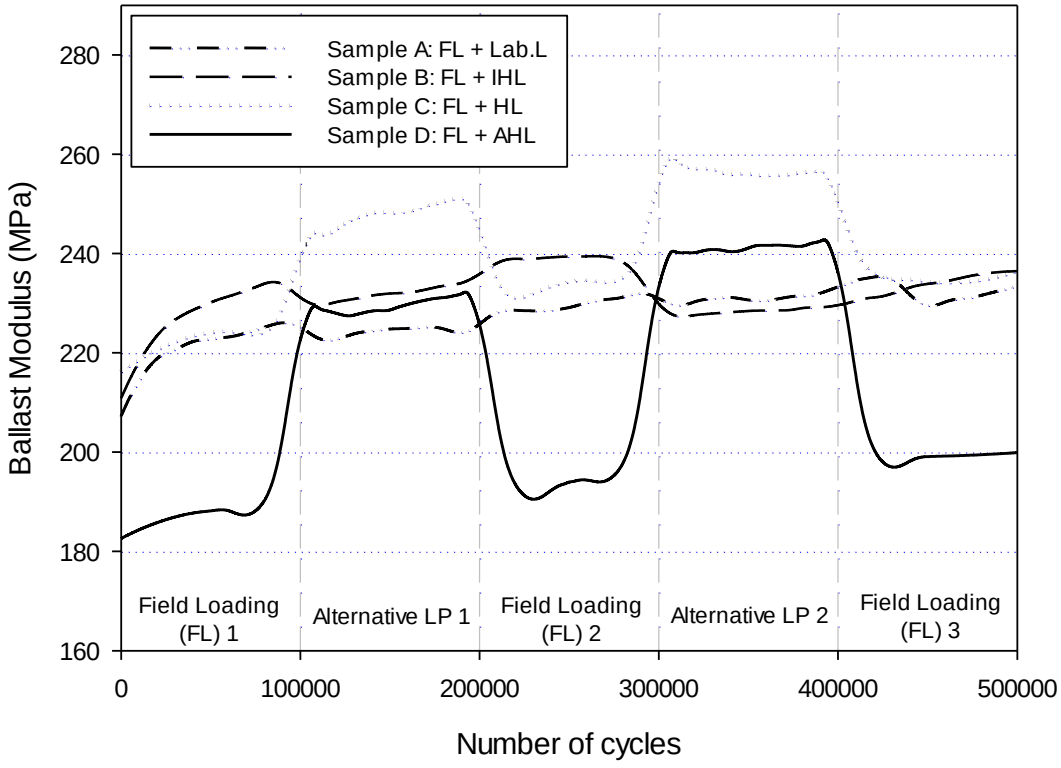

Figure 4-12: Ballast layer modulus per load cycle for each sample

Therefore, these factors might have contributed to the reduced modulus of test samples during the FL pattern. A more consistent FL pattern could be obtained when testing at lower frequencies (<2.5 Hz). Table 4-3 shows ballast modulus values at 150 000 and 350 000 cycles together with the increase in modulus for each loading pattern. The highest ballast modulus recorded at 350 000 cycles was 256 MPa for the HL pattern while the lowest ballast modulus was 228 MPa for the IHL pattern.

Table 4-3: Ballast modulus at 150 000 and 350 000 cycles with percentage increase for each loading pattern

Property	Lab. L	IHL	HL	AHL
Modulus at 150 000 cycles (MPa)	225	232	248	229
Modulus at 350 000 cycles (MPa)	231	228	256	241
Increase in modulus (%)	2.6	-1.5	3.1	5.5

4.1.6 Effect of Rest Periods on Ballast Permanent Settlement

Figure 4-13 (a) shows the ballast permanent settlement contribution of each loading pattern with increasing interval between load cycles. Figure 4-13 (b) shows the ballast permanent settlement contribution of each FL pattern with decreasing rest intervals between load cycles. Axial deformations from FL patterns with rest periods of 0.8 s and 0.4 s were similar, with settlement values of 0.021 and 0.019 mm respectively (Figure 4-13 (b)).

Looking at rest periods from the aspect of loading frequency, loading a ballast sample using an FL pattern with no rest period exposes the particles to more load pulses in a given time. This results in more inter-particle abrasion which leads to corner breakage, thus resulting in a considerable amount of ballast deformation. However, increasing the number of rest periods for the same amount of load pulses gives room for possible ballast recovery.

Figure 4-14 gives a summary of ballast permanent deformation caused by different loading patterns characterized by varying rest period intervals. For Stage Rest Period 1 (Stage RP 1), taking the settlement caused by a FL pattern with no rest period as a reference, there was an 83 % and 86 % reduction in settlement for the FL pattern of 0.4 s and 0.8 s respectively. For Stage Rest Period 2 (Stage RP 2), taking the settlement caused by a FL pattern with 0.8 s rest period as a reference, there was a 10 % reduction in settlement caused by the FL pattern with 0.4 s rest period, while a 110 % increase in settlement caused by a FL pattern without rest period was recorded. The reason for a decrease in settlement from a 0.8 s rest period to a 0.4 s rest period for Stage RP 2 is unclear. In summary, increasing the number of load pulses per given time increases the rate of ballast permanent settlement.

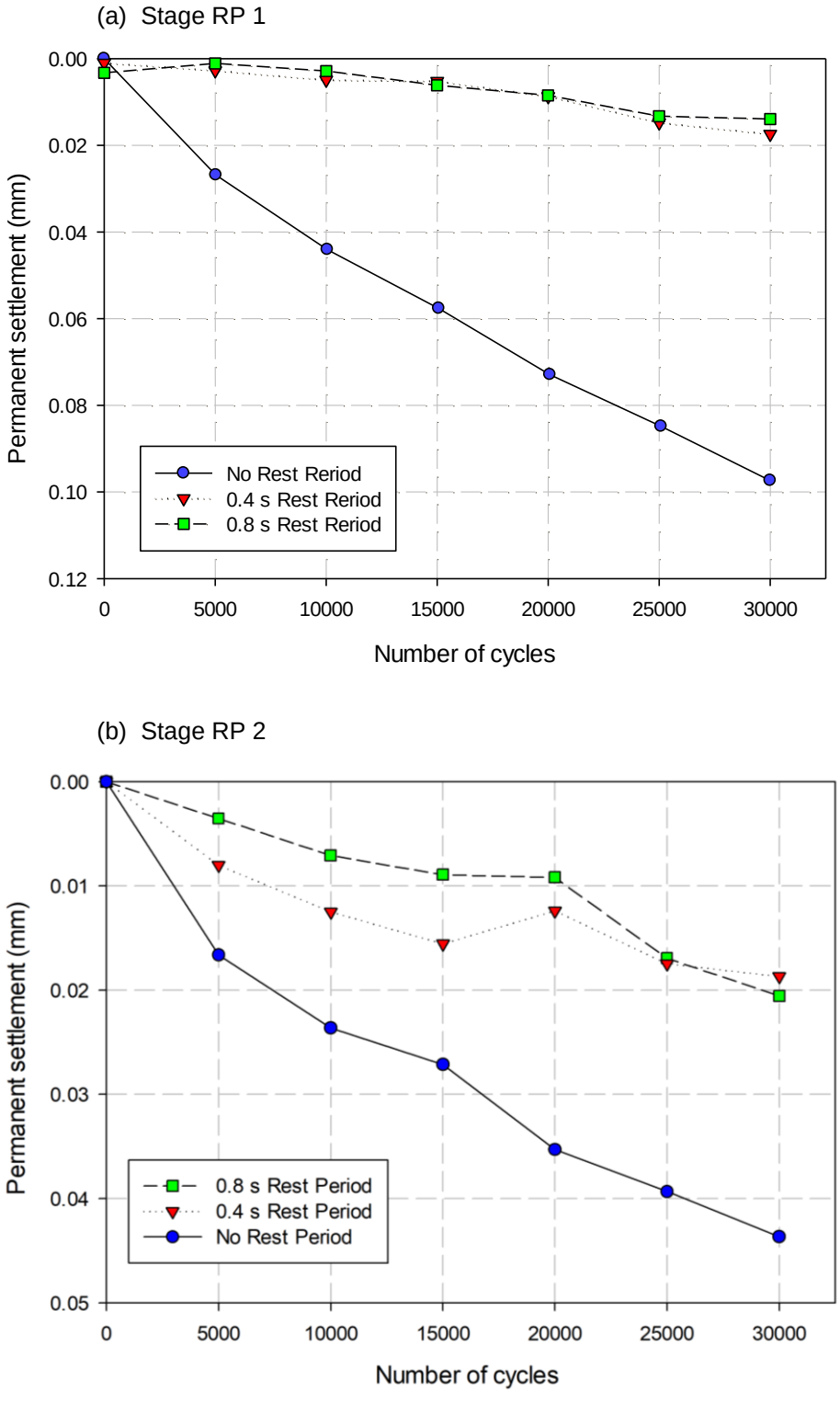

Figure 4-13: Permanent settlement of the ballast layer due to increasing (a) and decreasing (b) Rest Periods between loading cycles

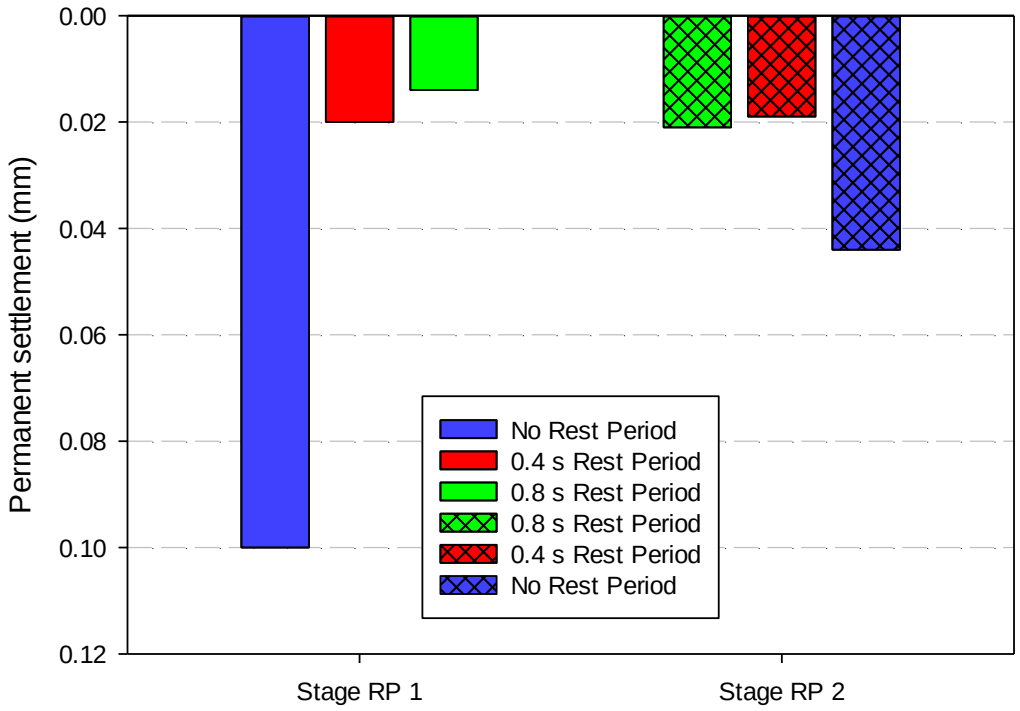

Figure 4-14: Final settlement of the ballast layer after increasing and decreasing intervals of Rest Period

Generally, it is expected that the duration of rest periods increases with decreasing train speeds. For heavy haul conditions with low train speeds (typically 50 km/h on average or less), rest periods can be more prominent between load cycles depending on bogie spacing (under constant train speed). Therefore, it is important to identify and execute the appropriate duration of rest period for different track loading parameters (such as passing speed, bogie spacing and wheel configurations) during laboratory testing. Further studies on rest periods are required to identify the appropriate rest period for different track loading parameters. Thus, laboratory specimen testing under heavy haul conditions is not realistic if the appropriate duration of rest period is not considered.

4.2 INFLUENCE OF BOUNDARY CONDITIONS

This section focuses on the results from the experiment conducted using the half (full-scale) box with step-wise decrease in lateral confinement (Setup 2). Results of ballast permanent deformation and the amount of ballast breakage due to varying lateral confinement are discussed in this section. The loading pattern used for this experiment was the AHL pattern. A maximum load of 90 kN was calculated, however, considering the properties of the AHL pattern, a load amplitude of 88.5 kN was applied across all samples. In addition, a preload of 1 kN was also applied.

4.2.1 Permanent Deformation

Figure 4-15 shows the axial strain deformation of the ballast layer at each level of lateral confinement with a constant deviatoric applied stress across all samples. Although a relative amount of lateral constraint is provided by the ballast shoulder (which was not considered in this work), the term '0 %' confinement refers to the absence of lateral constraint produced by the gate of the ballast box. It is important to note that the number of cycles (Figure 4-15) is represented as a quarter of the number of load pulses (which was 1.3 million) where a load cycle represents 4 wheel loads (to match the wheel configuration of CCR 11 wagons used on the South African Coal Line). This adjustment to the number of cycles agrees with the settlement trends of the ballast layer as it is expected that at a million cycles the settlement trend would have levelled off significantly where gradual degradation occurs with time as seen from previous research conducted on ballast in the literature.

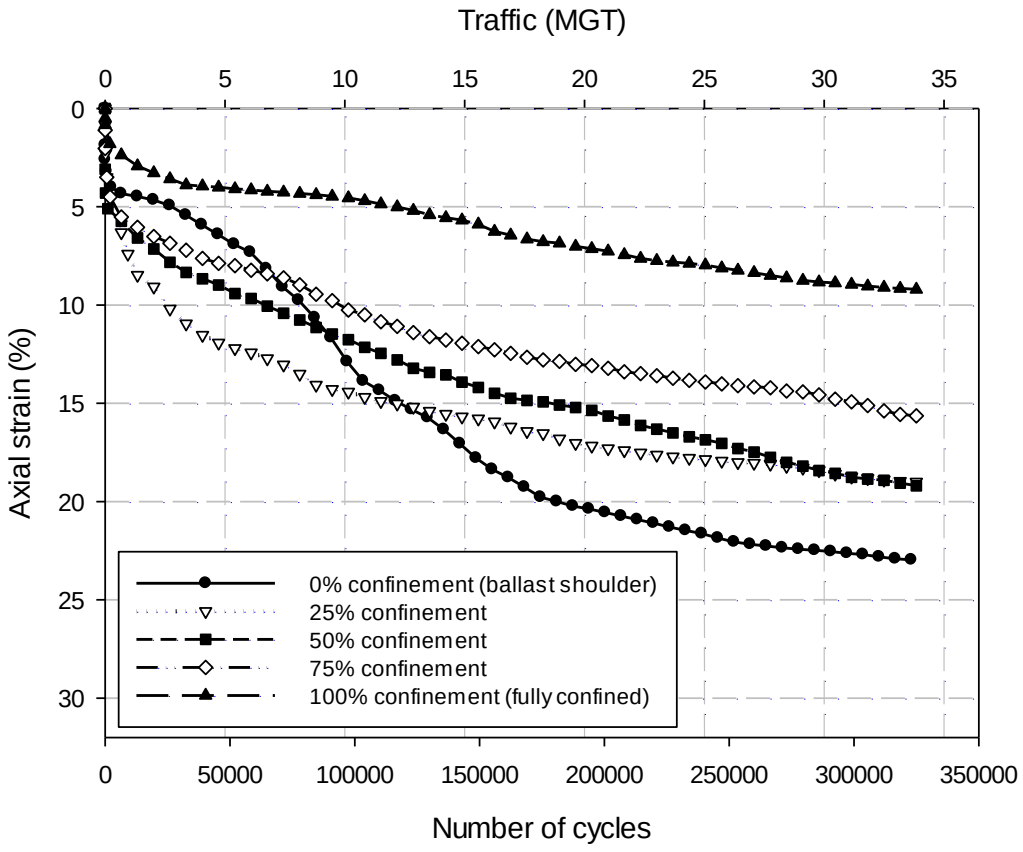

Figure 4-15: Axial strain deformation of the ballast layer at each level of lateral confinement

Discrepancies in Figure 4-15, such as irregular axial strain plot of the ballast layer at 0 % confinement and similar final ballast strain for 25 % and 50 % confinements could be due to slow deformation response after compaction and uncontrollable variations in ballast layer response (such as stiffness, modulus etc.) respectively.

Ballast degradation behaviour under cyclic loading for the various levels of lateral confinement can be classified into the degradation zones established by Indraratna et al. (2005) following the explanations below:

- Ballast degradation behaviour at 100 % confinement can be classified within the compressive stable degradation zone (CSDZ) where a high level of lateral confinement significantly restricts particle movement, reorientation and rearrangement according to Indraratna et al. (2005). Final ballast vertical settlement for the fully confined (100 %) ballast layer was 27.6 mm.
- Reducing the level of confinement to 75 % increased the final ballast settlement by 19.3 mm - a 70% increase in ballast settlement. This reduction in lateral confinement further increased particle movement into air voids and particle reorientation due to continuous vertical load pulses. This led to increased deflection and permanent settlement per load pulse. The ballast behaviour at 75 % confinement can be classified in the initial portion of the CSDZ.
- For 50 % lateral confinement, the ballast layer had a permanent settlement of 57.6 mm - a 10.7 mm settlement difference (22.8 % increase in vertical settlement) compared to the 75 % confinement case. The permanent settlement of the ballast layer at 25% and 50% lateral confinement was similar at approximately 57 mm. Ballast degradation at 50 % and 25 % lateral confinement can be described by the particle behaviour and degradation that occurs in the optimum degradation zone (ODZ) established by Indraratna et al. (2005).
- High levels of ballast settlement were observed and recorded for the ballast layer at 0 % confinement, with a vertical settlement of 68.9 mm. Comparing the amount of settlement at 25 % and 0 % confinement, vertical settlement increased by 20.9 % (11.9 mm) with a decrease in lateral confinement. The degradation zone that best describes the behaviour of particles under cyclic loading at 0 % confinement is the dilatant unstable degradation zone (DUDZ). Ballast particles in this zone are subjected to low confining lateral pressures under high deviatoric stresses which settles significantly with time. Particles had more room to displace as the level of lateral confinement decreases under the influence of constant loading. This leads to increased axial deformation and particle breakage.

Figure 4-16 shows a linear relationship between final permanent settlement and level of confinement after 325 000 cycles (1.3 million load pulses). This clearly indicates a general decrease in ballast layer settlement with increasing level of lateral confinement from 0 % to 100 %. There is a good fit of the regression line to the settlement values as indicated by a high coefficient of determination (R^2) value of 0.893.

4.2.2 Permanent Deformation Models

Published ballast settlement (S_N) and strain (ε_N) models from previous research in the literature were compared with test settlement and strain data respectively as a function of number of cycles (N) and other related parameters. These published models are summarised in Table 4-4. Certain parameters were kept constant as indicated in the footnote to Table 4-4. The remaining parameters in the models were determined by fitting a regression to the experimental data using the method of least squares in Microsoft Excel. Table 4-5 presents the final fitted parameters of each ballast permanent deformation model which provided the best fit.

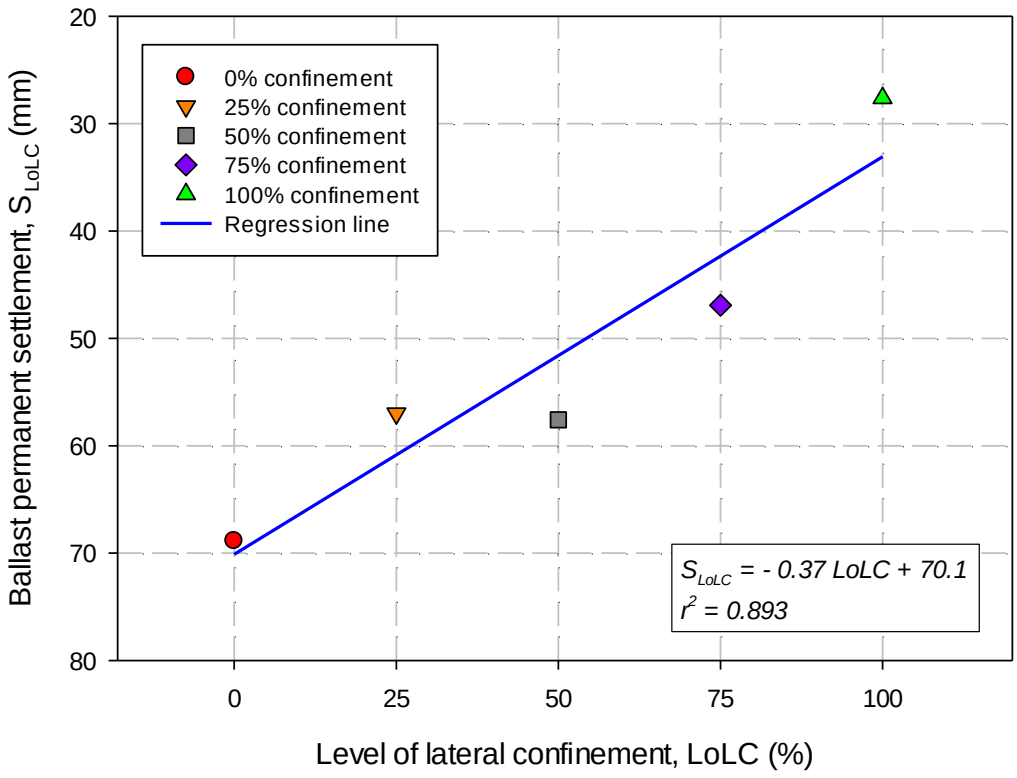

Figure 4-16: Linear relationship between final ballast settlement and level of lateral confinement

Plots of permanent settlement, S_N and strain, ε_N against number of cycles for 100 % lateral confinement are shown in Figure 4-17 and Figure 4-18 respectively. From Figure 4-17, the following conclusions can be drawn:

- Settlement deformation models established by Selig & Waters (1994) and Sato (1995), which are power functions, produced similar settlement trends as the test data settlement with final settlements of 27.3 and 29 mm respectively in comparison to the test settlement data of 27.6 mm after 325 000 cycles (1.3 million load pulses)
- Log linear models of Stewart & Selig (1984), Neidhart (2001), etc. under-predicted the settlement.
- The settlement model of Thom & Oakley (2006) is a logarithmic function of solely the number of cycles. Hence, it provides a poor prediction of the ballast settlement during the test.

Table 4-4: Deformation models of settlement and strain as a function of number of cycles

Deformation model	Reference
$S = K_s \frac{A_e}{20}[(0.69 + 0.028L)N^{0.2} + (2.7 \times 10^{-6})N]$	Shenton (1984)
$S_N = s(F_l)^{1.6}(1 + c' \ln N)$	Hettler (1984)
$d_N = d_1(1 + C_b \log N)$	Stewart & Selig (1984)
$S_N = p\, N^q$	Selig & Waters (1994)
$S = \left[\log_{10}(N) - 2.4\right]^2$	Thom & Oakley (2006)
$S_N = \gamma(1 - e^{-\alpha N}) + \beta N$	Sato (1995)
$S_N = S_1 + \frac{e \log N}{1 + f \log N}$	Neidhart (2001)
$S_N = S_1(N^y)$	Indraratna et al. (2007)
$S_N = c + d(\ln N)$	Indraratna et al. (2011)
$S_N = S_1(1 + a \ln N + 0.5b \ln N^2)$	Indraratna & Nimbalkar (2013)
$\varepsilon_N = 0.082(100n - 38.2)(\sigma_1 - \sigma_3)^2 \times (1 + 0.2 \log N)$	ORE (1970)
$\varepsilon_N = \varepsilon_1\left(1 + C \log_{10} N\right)$	Shenton (1978)
$\varepsilon_N = (0.85 + 0.38 \log N)\varepsilon_1 + (\varepsilon_1)^2 \times (0.05 - 0.09 \log N)$	Alva-Hurtado & Selig (1981)

$\varepsilon_N = t\ N^u$	Selig & Waters (1994)

A_e (average axle load) = 26 tonnes; L (tamping lift) = 0; n (porosity) = 0.3

From Figure 4-18, the following conclusions can be drawn:

- Strain deformation models established by the Selig & Waters (1994) power model provides a good prediction of the axial strain deformation at 100 % confinement.
- Log linear models of ORE (1970) and Shenton (1978) under-predict the final axial strain of the test data.
- Alva-Hurtado & Selig's model provides a poor estimate of axial strain deformation.

Table 4-5: Parameter values used to obtain best fit curves for permanent deformation models using the method of least squares

Model reference	Varied Parameters	Parameter values for each LoLC				
		100	**75**	**50**	**25**	**0**
Shenton (1984) - S_N	K_s	1.91	3.51	4.21	4.61	5
Hettler (1984)	s	5.2×10^{-4}	9.6×10^{-4}	7.6×10^{-4}	9.5×10^{-4}	7.3×10^{-4}
	c'	2.31	2.33	3.54	3.13	4.33
Stewart & Selig (1984)	d_1	-1.44	-3.33	-9.28	-2.66	-5.73
	C_b	1.05	0.83	0.31	1.42	0.66
Selig & Waters (1994) - S_N	p	0.073	0.72	0.5	2.4	0.06
	q	0.47	0.33	0.37	0.25	0.56
Thom & Oakley (2006)	-	-	-	-	-	-
Sato (1995)	γ	8.5	21.9	24.3	36	79.2
	α	1.8×10^{-2}	1.3×10^{-4}	1.1×10^{-4}	7.2×10^{-5}	7.1×10^{-6}
	β	6.3×10^{-5}	8.2×10^{-5}	1.1×10^{-4}	7.1×10^{-5}	0
Neidhart (2001)	e	4.05	7.62	10.15	9.73	10.91
	f	0	0	0	0	0
Indraratna et al. (2007)	y	0.22	0.2	0.13	0.24	0.19
Indraratna et al. (2011)	c	0	0	0	0	0
	d	1.64	3.03	3.62	4	4.25
Indraratna & Nimbalkar (2013)	a	0.52	0.41	0.15	0.71	0.33
	b	0.52	0.41	0.15	0.71	0.33
ORE (1970)	σ_3 (kPa)	44.6	0	0	0	0
Shenton (1978) - ε_N	C	2.42	1.9	0.7	3.27	1.51
Alva-Hurtado & Selig (1981)	-	-	-	-	-	-

Selig & Waters (1994) - ε_N	t	2.4×10^{-4}	2.4×10^{-3}	1.7×10^{-3}	8.0×10^{-3}	2.0×10^{-4}
	u	0.47	0.33	0.37	0.25	0.56

Coefficient of determination (R^2) values were determined for each model for all levels of lateral confinement as shown in Table 4-6. The R^2 values provide more information on the quality and goodness of fit of each model's relationship to the different levels of lateral confinement. Permanent deformation models with high R^2 across all levels of lateral confinement include Shenton (1984) - S_N, Selig & Waters (1994) - S_N, Sato (1995), and Selig & Waters (1994) - ε_N.

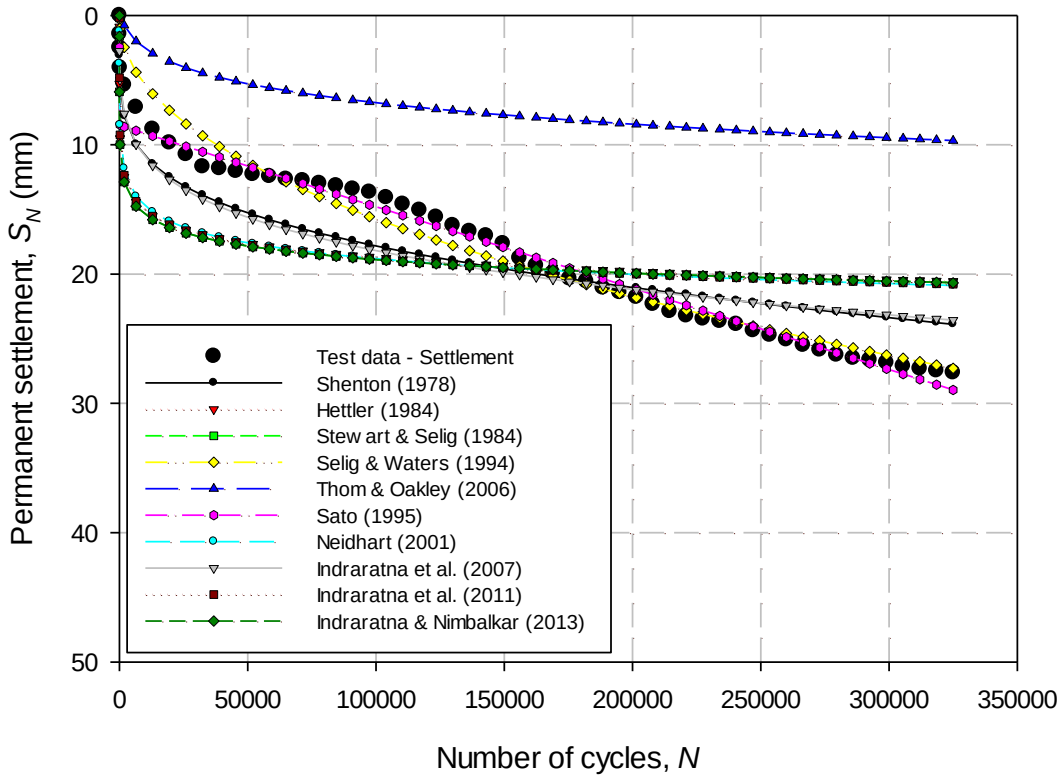

Figure 4-17: Ballast permanent settlement models fitted to the settlement test data of 100 % confinement

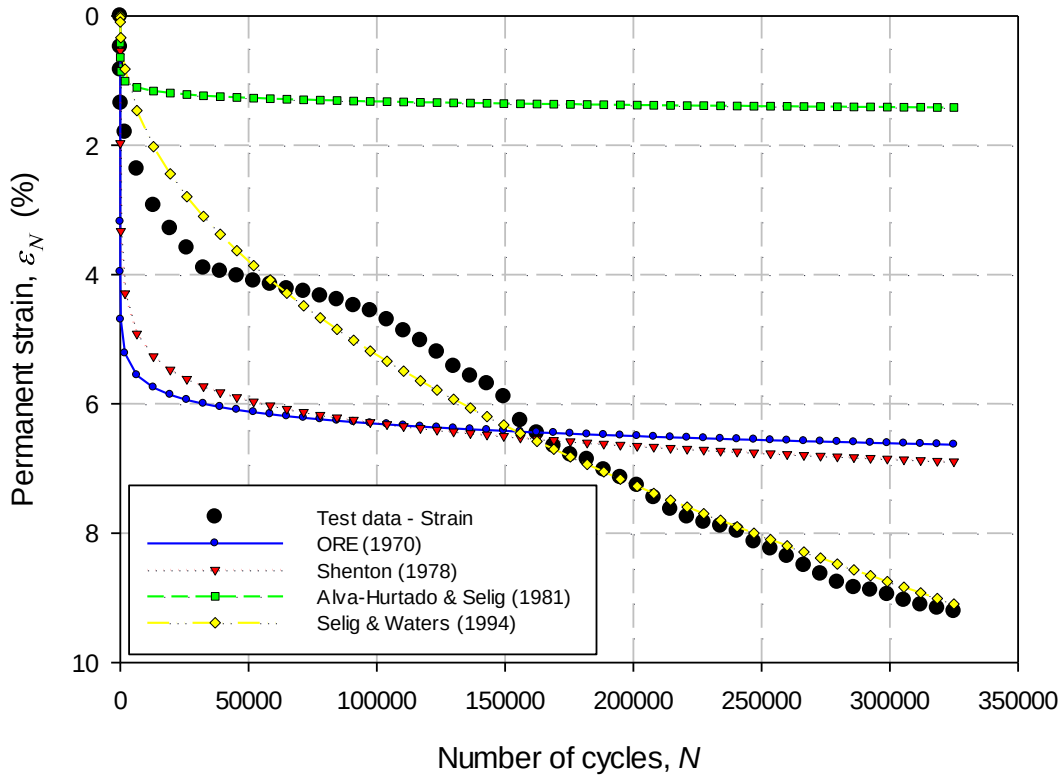

Figure 4-18: Ballast permanent strain models fitted to the strain test data of 100 % confinement

Table 4-6: Goodness of fit of models for each LoLC based on the coefficient of determination, R^2

Model reference	Coefficient of determination, R^2 for each LoLC				
	100	**75**	**50**	**25**	**0**
Shenton (1984) – S_N	0.82	0.95	0.91	0.99	0.73
Hettler (1984)	0.48	0.62	0.58	0.74	0.40
Stewart & Selig (1984)	0.46	0.61	0.51	0.73	0.38
Selig & Waters (1994) - S_N	0.96	0.99	0.99	0.997	0.96
Thom & Oakley (2006)	-2.53	-7.53	-7.07	-11.8	-3.91
Sato (1995)	0.99	0.97	0.99	0.98	0.98
Neidhart (2001)	0.51	0.66	0.65	0.77	0.44
Indraratna et al. (2007)	0.79	0.90	0.71	0.996	0.64
Indraratna et al. (2011)	0.49	0.63	0.58	0.75	0.41
Indraratna & Nimbalkar (2013)	0.46	0.61	0.51	0.73	0.38
ORE (1970)	0.34	-0.15	-0.92	-2.36	-0.88
Shenton (1978) - ε_N	0.46	0.60	0.51	0.73	0.38
Alva-Hurtado & Selig (1981)	-5.03	-6.71	-1.27	-12	-2.46
Selig & Waters (1994) - ε_N	0.96	0.99	0.99	0.997	0.96

4.2.3 Ballast Breakage

Two ballast breakage indices, among others, were used to quantify the breakage of the painted ballast particles in the ballast layer (placed at 100 mm and 300 mm from the base of ballast layer) after loading for each level of lateral confinement. These two breakage indices included Marsal's breakage index (Marsal 1967) and the Ballast Breakage Index (BBI) introduced by Indraratna et al. (2005) as explained in Section 2.8. Results of ballast breakage indices for each level of confinement are discussed in this section.

Marsal's breakage index, B_g

Figure 4-19 and Figure 4-20 shows the difference in percentage retained (ΔW_k) at each sieve size for the painted ballast placed at 100 and 300 mm respectively, for each lateral ballast confinement level. Positive ΔW_k values would be expected for large sieve sizes because less ballast was retained on the larger sieves after grading. Furthermore, negative ΔW_k values would be expected on the smaller sieve sizes as particles which have broken off from the larger pieces fall through the large sieve sizes and are retained on the smaller sieve sizes. These trends are evident at the 22 mm and 38 mm sieves for 100 and 300 mm depths. Due to increased loading influence on ballast particles at 300 mm (Figure 4-20), significant breakage is observed, especially on the 50.8 mm particles.

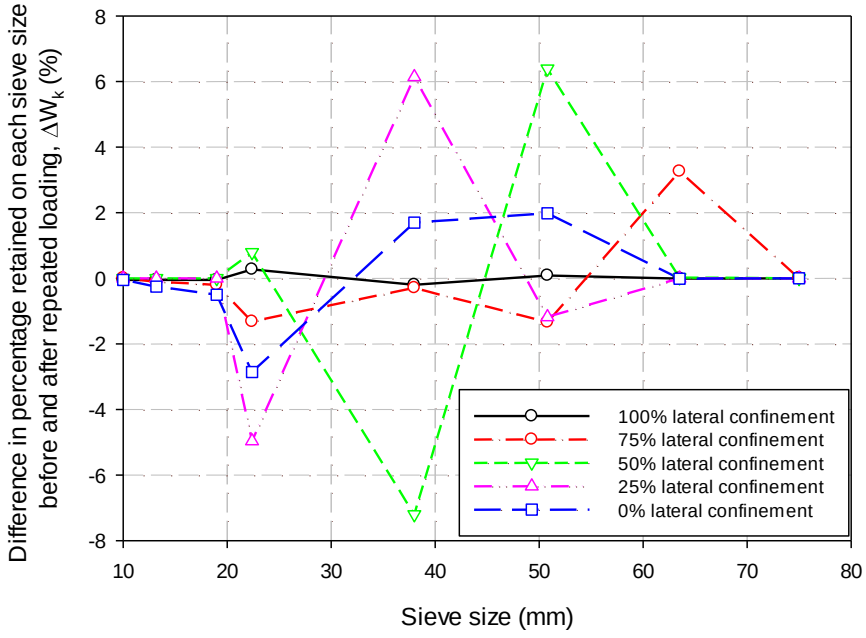

Figure 4-19: Difference in percentage retained on different sieve sizes for the painted ballast at 100 mm from the ballast layer base for each level of lateral confinement

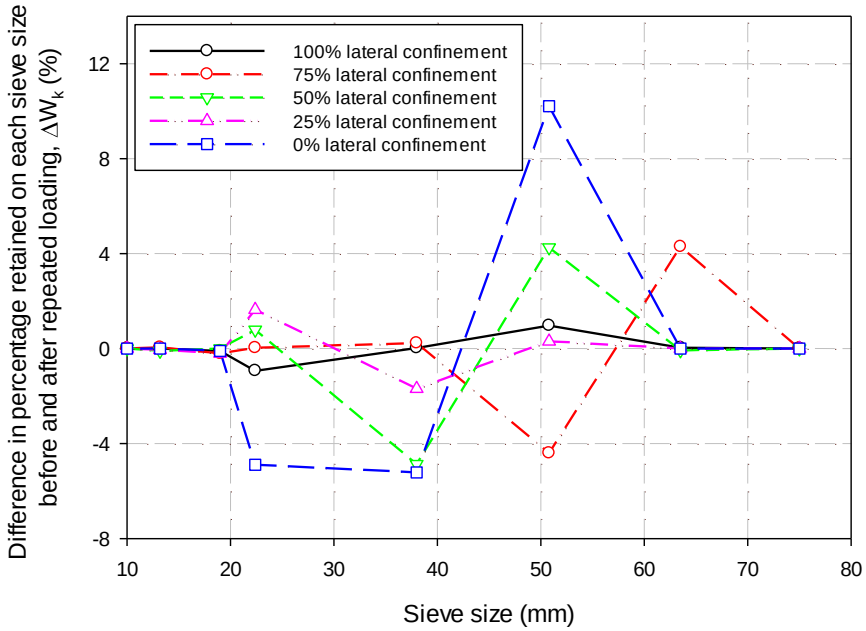

Figure 4-20: Difference in percentage retained on different sieve sizes for painted ballast at 300 mm from the ballast layer base for each level of confinement level

Figure 4-21 shows a bar chart of the Marsal's breakage index B_g for the painted ballast particles at 100 and 300 mm from ballast layer base at each level of ballast lateral confinement. At 100 mm there is a general increase in the breakage of the ballast particles with a decrease in lateral confinement. At 300 mm, more ballast breakage was observed at 50 % confinement.

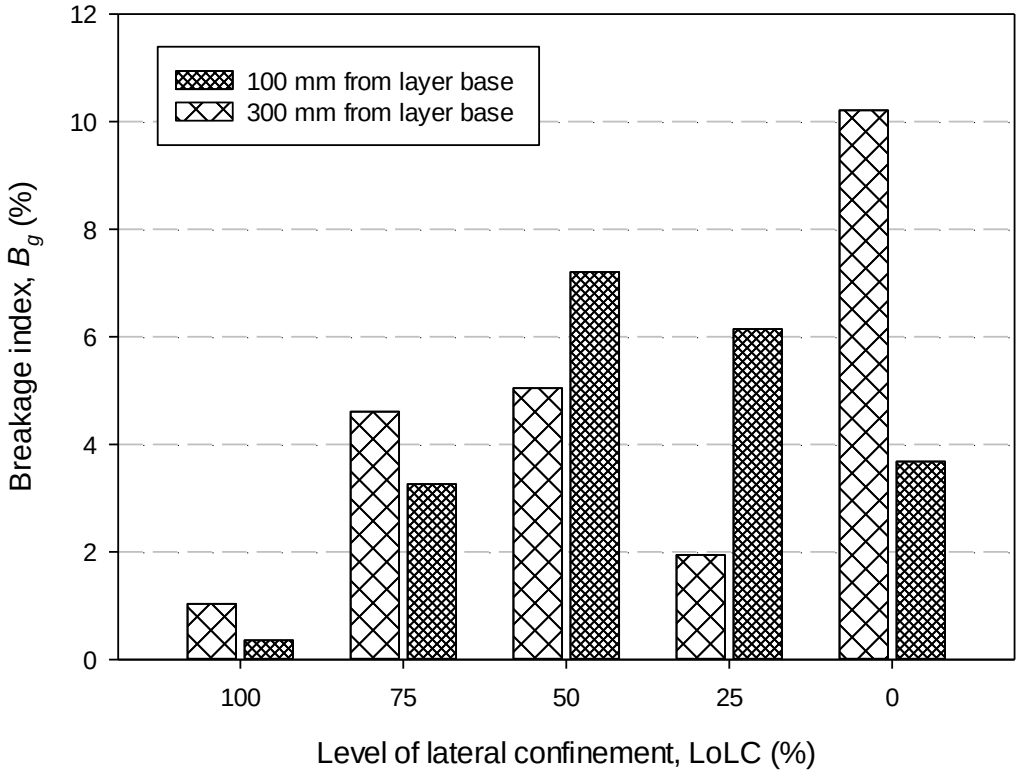

Figure 4-21: Marsal's breakage index of painted ballast particles placed at 100 and 300 mm from the base of the ballast layer for each level of lateral confinement

Indraratna's Ballast Breakage Index, BBI

Sieve analyses were conducted before and after each test at different levels of confinement to evaluate the degradation of ballast using the BBI technique. Figure 4-22 (a) and (b) shows the particle size distribution of the painted ballast at 100 and 300 mm before and after the test for a fully confined (100 % confined) ballast layer.

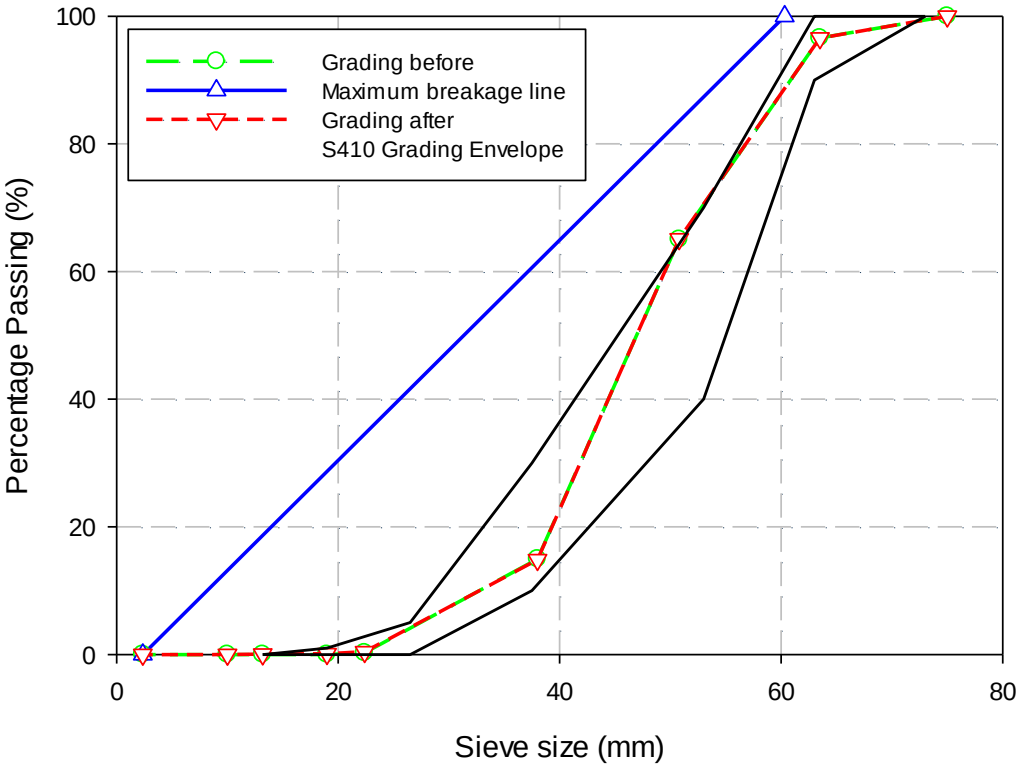

(a)

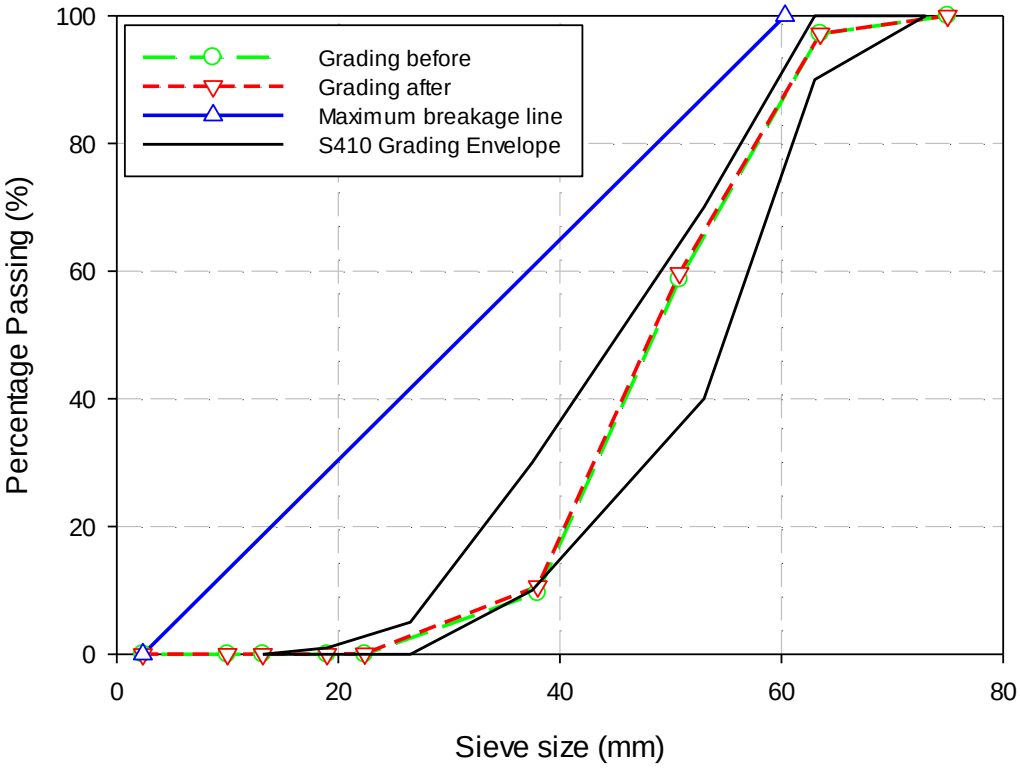

(b)

Figure 4-22: Particle size distribution for painted ballast at (a) 100 mm and (b) 300 mm from the base of the ballast layer before and after 100 % level of lateral confinement test

Table 4-7 shows the BBI results. As expected, there was more particle degradation at 300 mm (particles closer to the sleeper) at 100 % and 0 % lateral confinement than at 100 mm. However, for 75 % to 25 % lateral confinement, there was more particle breakage for particles at 100 mm than at 300 mm. This is contrary to expectation. Possible contributing factors to the discrepancies in BBI values between levels of confinement could be:

- Displaced painted ballast particles that are not within the sleeper loading region due to particle rearrangement during compaction. This movement is assumed to be significant at 300 mm than at 100 mm as high inter-particle contact forces decrease with depth (Han 2012).
- The probability of the same particle passing through the appropriate sieve during sieve analysis after testing might be low at some instances. Furthermore, Abadi et al. (2016) stated that the degree of particle breakage was not sufficiently detected by comparing PSDs before and after cyclic loading test.
- The number of ballast particles (overall sample size) may not be statistically significant and might have contributed to the discrepancies in these results.

Table 4-7: Ballast Breakage Index (BBI) at 100 mm and 300 mm for each level of confinement

	BBI	
Level of confinement (%)	**At 100 mm**	**At 300 mm**
100	0.0019	0.034
75	0.166	0.073
50	0.084	0.048
25	0.097	-0.023
0	0.086	0.251

The difference in mass before and after cyclic loading for each lateral confinement at 100 mm and 300 mm were compared as shown in Figure 4-23. This method was suggested by Abadi et al. (2016). A clear indication that ballast degradation is significant closer to the sleeper as well as for a ballast layer supported by a ballast shoulder without additional lateral confinement is provided in Figure 4-23. The change in mass at 300 mm for the 75 % confinement is considered an outlier.

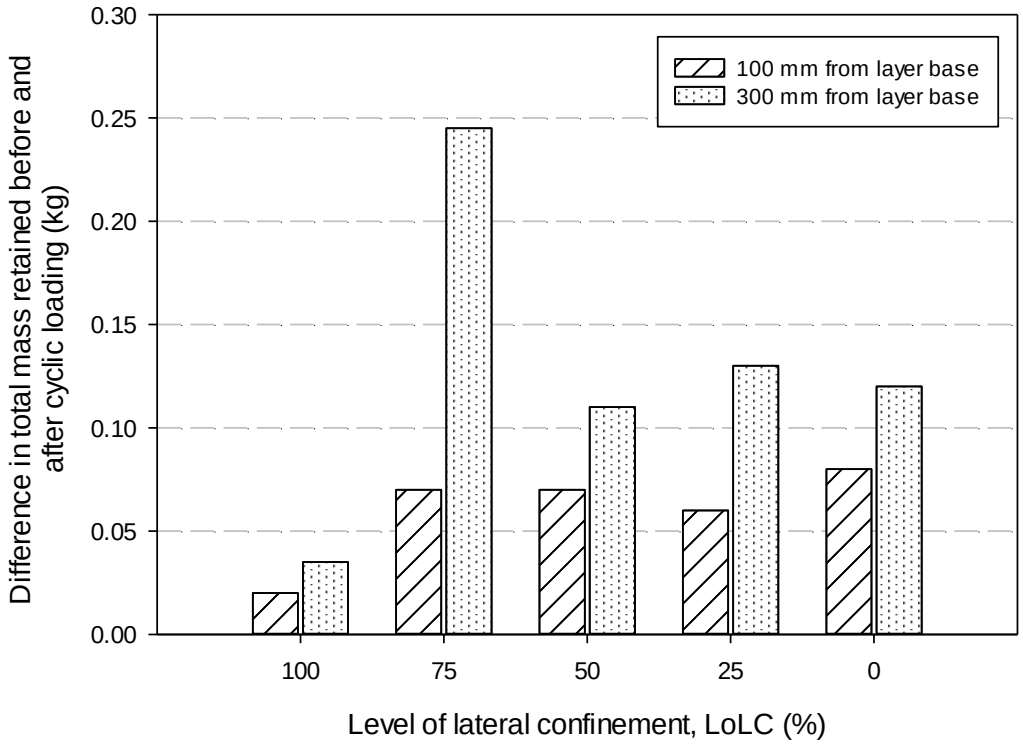

(a)

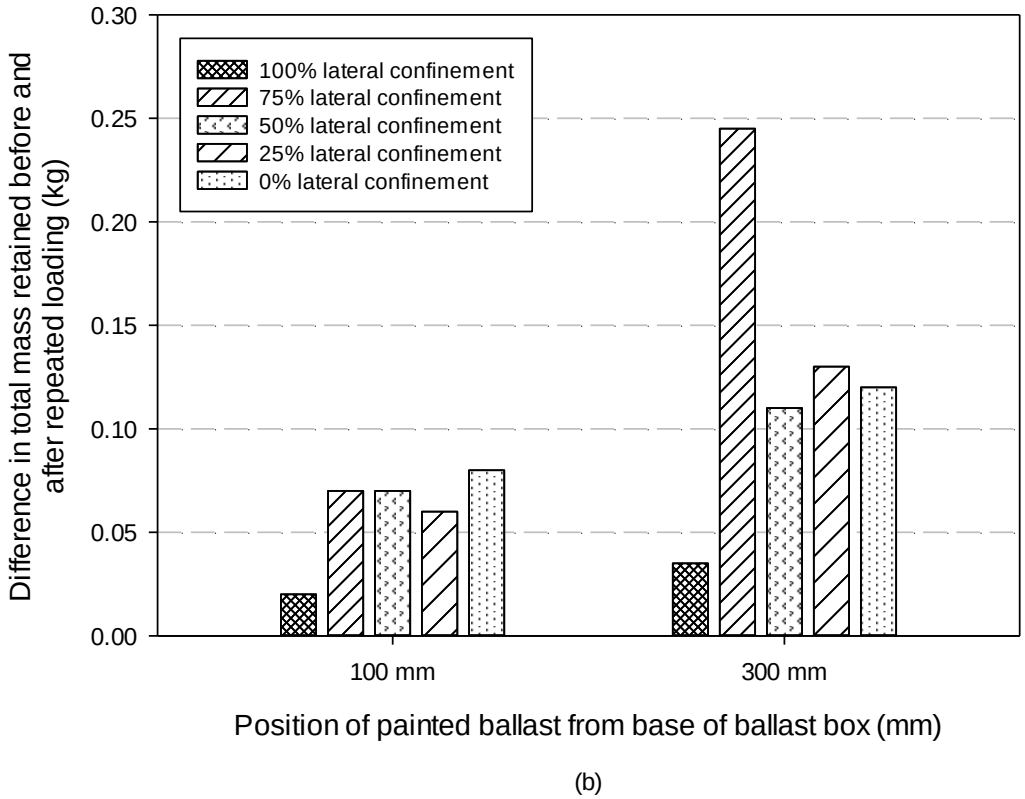

(b)

Figure 4-23: Difference in mass before and after cyclic loading at (a) 100 and 300 mm from base of ballast layer for each lateral confinement and (b) the effect of lateral confinement on changes to total mass of ballast at 100 and 300 mm before and after cyclic loading

Figure 4-24 shows different forms of ballast breakage which consists of corner breakage, with particle fatigue and particle splitting along weak planes (such as micro cracks and flaws).

Figure 4-24 (a) shows particle corner breakage after cyclic loading at 100 % lateral confinement. Attrition of asperities (Figure 4-24 (d)) and corner breakage are the foremost kind of breakage across all levels of confinement. However, according to Indraratna et al. (2005), particle splitting through planes of weakness and particle fatigue become more prominent under fully (100%) confined conditions (in the CSDZ).

Figure 4-24 (b) shows particle splitting occurring in the ballast layer – laterally supported by a full ballast shoulder profile (0 % confinement). These particles were situated 100 mm from the base of the ballast layer. This indicates that the inter-particle contact forces increased with number of cycles due to extensive settlement, causing significant particle degradation to lower lying particles of the ballast layer.

Figure 4-24 (c) shows a split ballast particle bounded by the steel box wall and neighbouring ballast particles following the 75 % lateral confinement test.

Figure 4-24 (d) are images of painted ballast placed at 100 and 300 mm from the base of the ballast layer after load applications. White patches on each painted ballast particle reveals the contact points of neighbouring ballast particles during load application which result in attrition of asperities (unevenness or roughness).

Figure 4-24 (e) shows particle splitting after cyclic loading on the ballast layer – laterally supported by a 25 % level of confinement.

Figure 4-24 (f) and (g) show images of particle breakage along weak planes (such as micro cracks and flaws) and particle splitting (or corner breakage) respectively, that occurred in the ballast layer subjected to vertical load application, supported with a 75 % level of lateral confinement.

In general, the most common forms of ballast breakage, among others, are attrition of asperities and corner breakage. Other forms of breakage are particle splitting along weak planes and particle fatigue. A major governing factor stimulating ballast breakage is the fracture strength of individual ballast particles. A particle with a high fracture strength will experience attrition of uneven surfaces and slight corner breakage and has the capacity to tolerate high stress levels and higher load applications. However, a particle with a low fracture strength, characterised by micro cracks and flaws, will experience particle split at low stress levels and low number of load cycles. Therefore, to ensure limited degradation of the ballast layer and track structure,

obtaining high quality ballast particles on the railway track (especially heavy haul lines) is necessary.

Figure 4-24: Forms of ballast breakage

4.3 BALLAST LAYER STRESS RESULTS

Figure 4-25 shows the layout of the Tekscan pressure mats in the steel box. To analyse the overall effect of stress on the substructure rather than point stresses generated by individual ballast particles (Figure 4-26 (a)), the 'Averaging' option was selected which modified each sensel's pressure value to reflect the value of neighbouring sensels. This action was performed for each Pressure mat (A, B and C). Figure 4-26 (b) illustrates the changes after the averaging function was applied to the raw data.

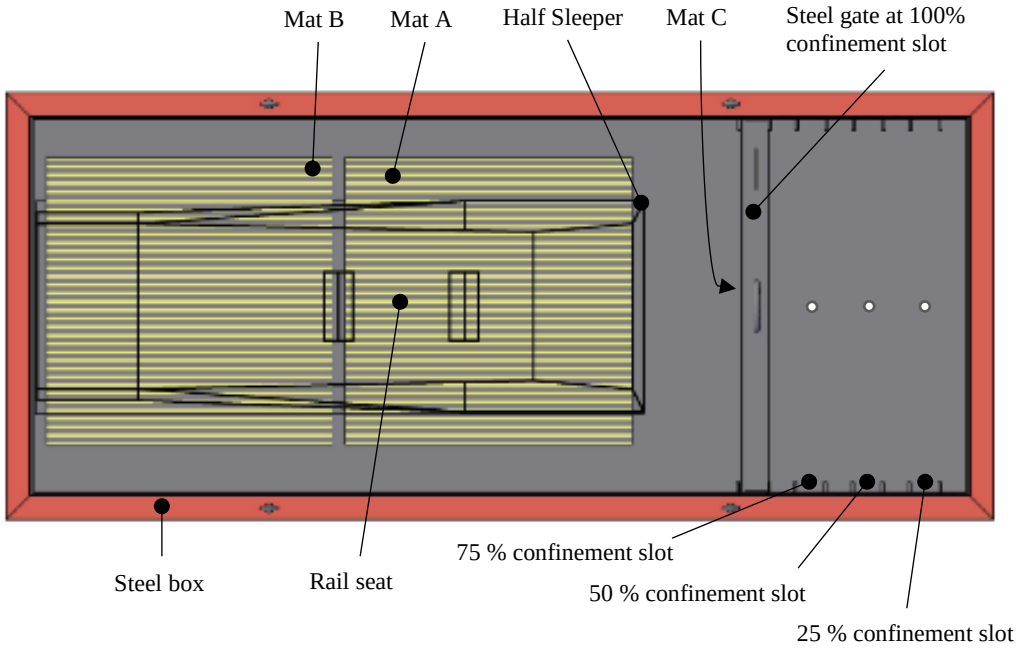

Figure 4-25: Plan view of steel box and layout of Tekscan pressure mats

The pressure data for the horizontal pressure mats (Mat A and B) at the bottom of the ballast layer were analysed by separating their areas into two portions:

- Portion 1 (red rectangle in Figure 4-27) considers the pressures acting in the area projected vertically down from the base of the sleeper, while
- Portion 2 (green square in Figure 4-27) considers the pressure over the entire surface area of the pressure mat.

The analysis of the laterally placed Tekscan mat (Mat C) only considered a total height of 400 mm to include the pressures from the crib ballast as shown in Figure 4-28. Sensel pressure values from each pressure mat was saved as an ASCII file. For all pressure mats, the average

pressures in each portion considered was determined by dividing the sum of all pressures bounded by each portion with the total number of pressure sensels within each portion.

(a)

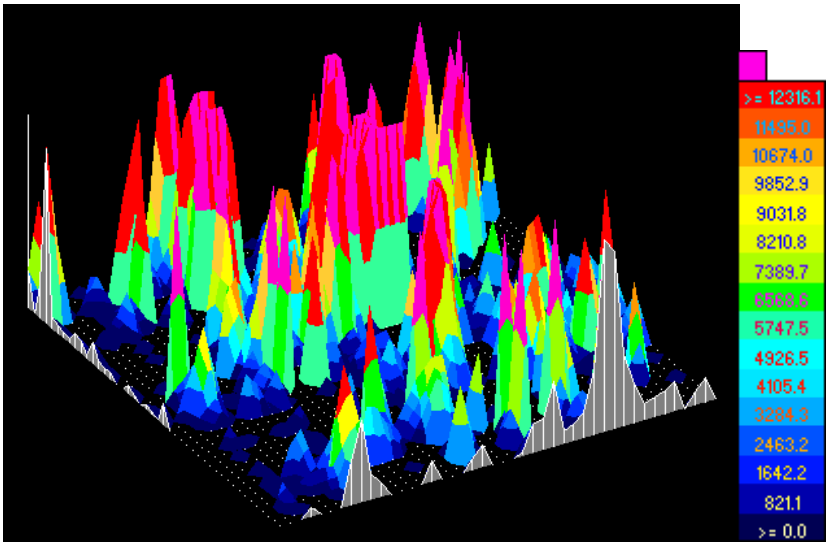

(b)

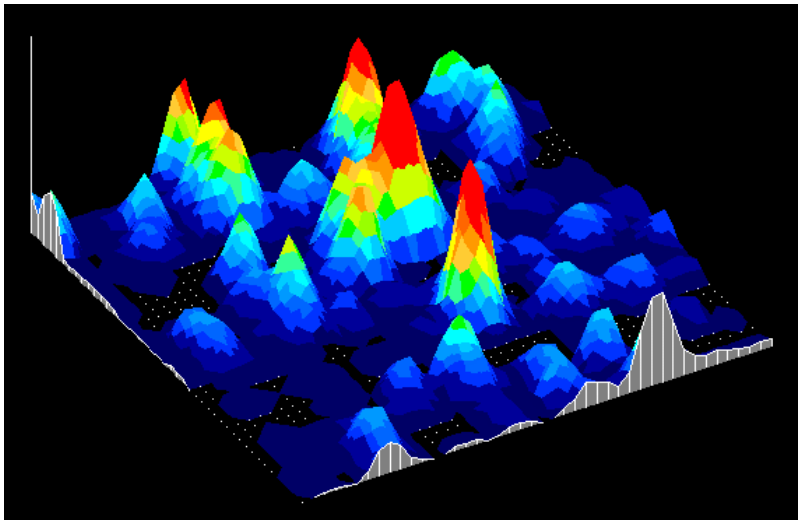

Figure 4-26: 3D solid view of (a) pressure contours for selected ballast particles and (b) averaged pressure contours at the base of the ballast layer

4.3.1 Matrix Based Tactile Surface Sensors: Mat A

Figure 4-29 shows the averaged sensel pressures within the sleeper and pressure mat region at the bottom of the ballast layer recorded at every 65 000 cycles for 100 % and 0 % lateral confinement. Pressure data for 50 % confinement was not obtained as there was a misalignment between the sensor and the handle after the ballast was placed in the box.

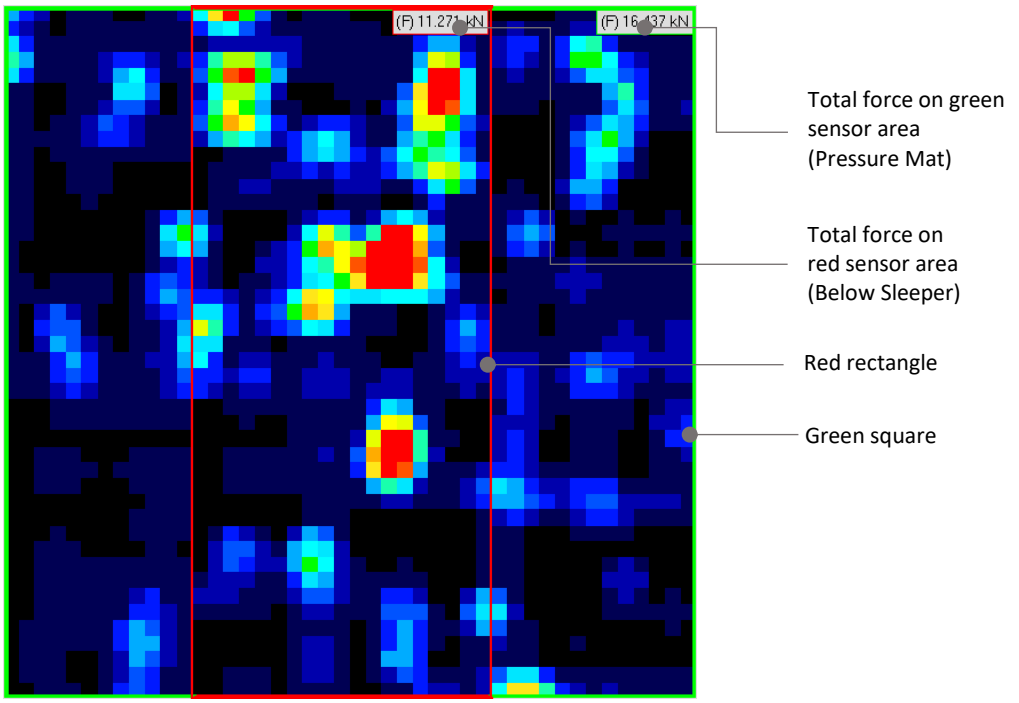

Figure 4-27: 2D view window with a red rectangle and a green square to assess pressure values below the sleeper region and over the pressure mat surface area

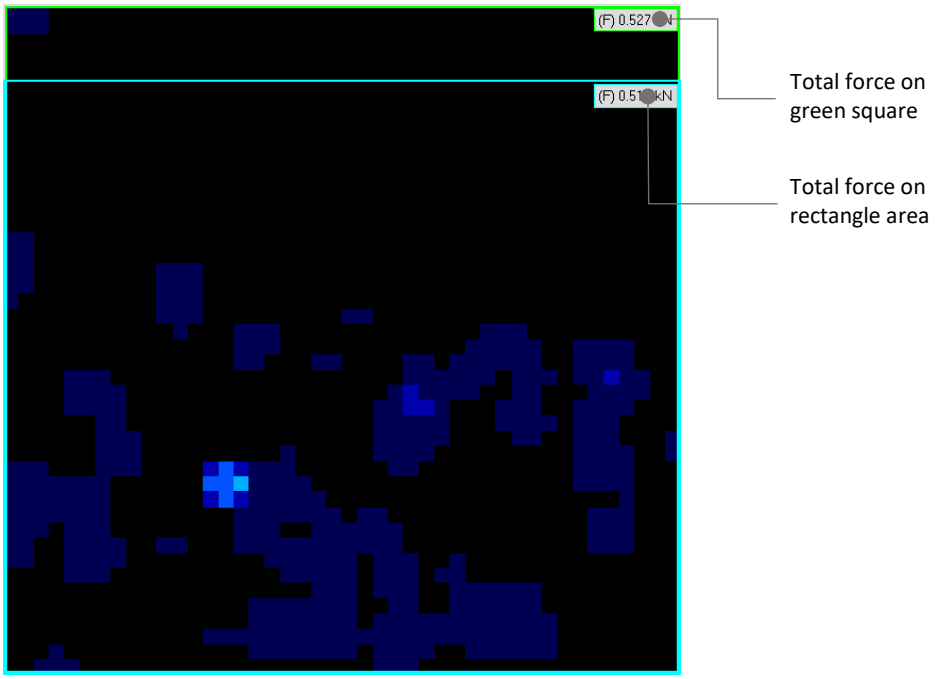

Figure 4-28: 2D view window for lateral pressure mat with a rectangle to assess pressure values up to the crib ballast

There is a general increase in pressure as the number of cycles increase. As depth is a function of stress, the stress at the bottom of the ballast layer increases as the sleeper moves closer to the base due to axial strain deformation during cyclic loading. Figure 4-30 shows the average vertical pressure at 100 % and 0 % lateral confinement in the sleeper region and over the pressure mat surface area. These pressures were determined by computing the average maximum pressure for every 65 000 cycles (Figure 4-29). It is expected that the pressures directly below loaded sleepers will be greater than the overall pressure (or stress) experienced by the underlying layers.

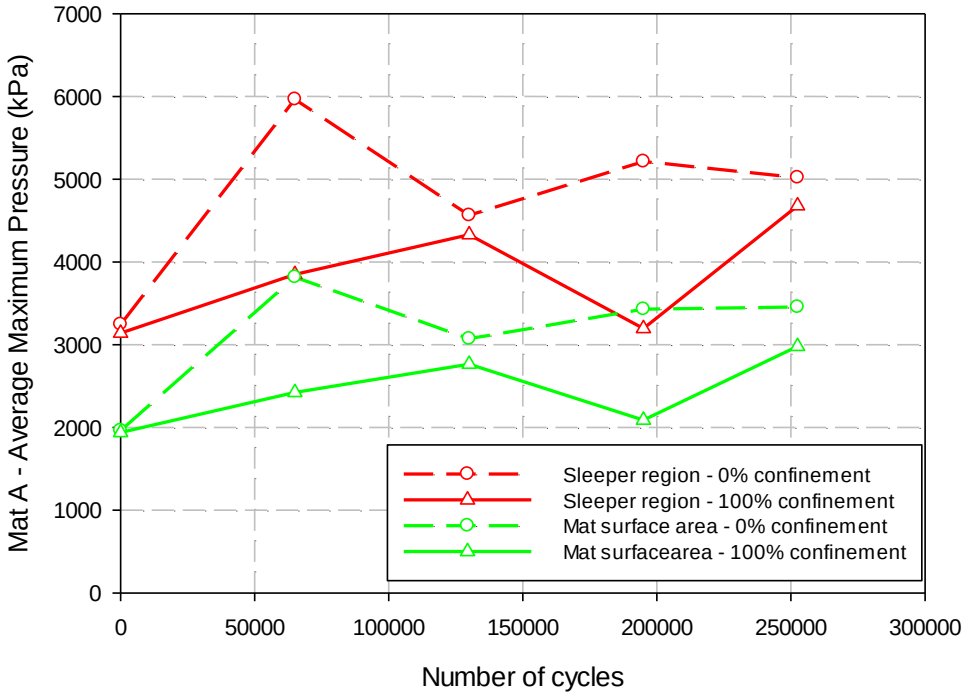

Figure 4-29: Average maximum pressure on Mat A for every 65 000 cycles within the sleeper region and over the mat surface area at the bottom of the ballast layer for 0 % and 100 % lateral confinements

4.3.2 Matrix Based Tactile Surface Sensors: Mat B

Figure 4-31 shows the average sensel pressures on Mat B for pressures below the sleeper and the pressure mat surface area at every 65 000 cycles for 0 %, 50 % and 100 % lateral confinement. High pressures are experienced at the bottom of the ballast layer for 0 % lateral confinement compared with 50 % and 100 % lateral confinement which have similar pressure magnitudes at the bottom of the ballast layer. These pressures increase with continuous traffic which leads to increased rates of deformation of underlying layers. Thus, the level of lateral

confinement plays an important role in limiting vertical stresses at the bottom of the ballast layer.

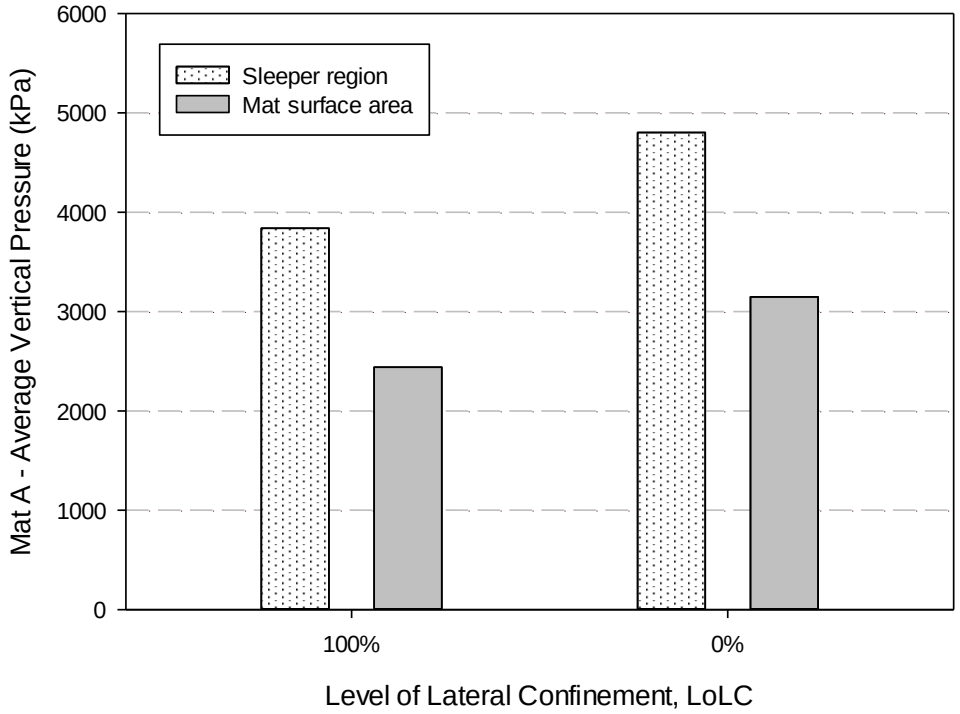

Figure 4-30: Average vertical pressures on Mat A within the sleeper region and over the mat surface area for 100 % and 0 % lateral confinements

Figure 4-32 shows the average vertical pressure of Mat B for 100 %, 50 % and 0 % confinements for the sleeper region and for the mat surface area. These pressures were determined by computing the average maximum pressure for every 65 000 cycles (Figure 4-31). It is not clear as to the seemingly equal pressures for the 100 % and 50 % lateral confined ballast layers. However, a clear difference in pressures are observed from an unconfined ballast layer.

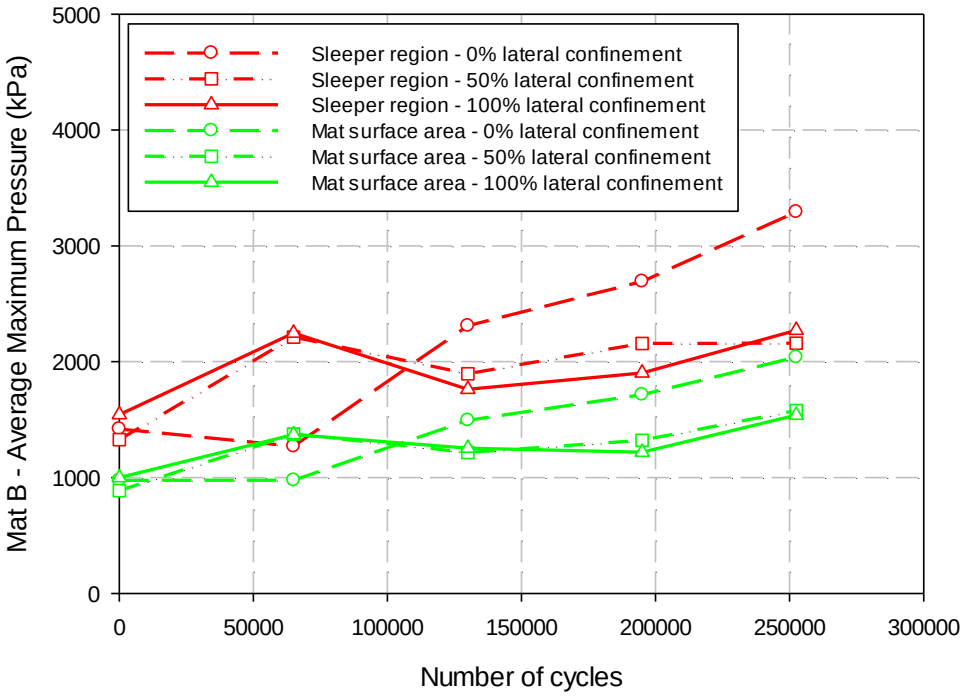

Figure 4-31: Average maximum pressure on Mat B for every 65 000 cycles within the sleeper region and over the mat surface area at the bottom of the ballast layer for 0 %, 50 % and 100 % lateral confinements

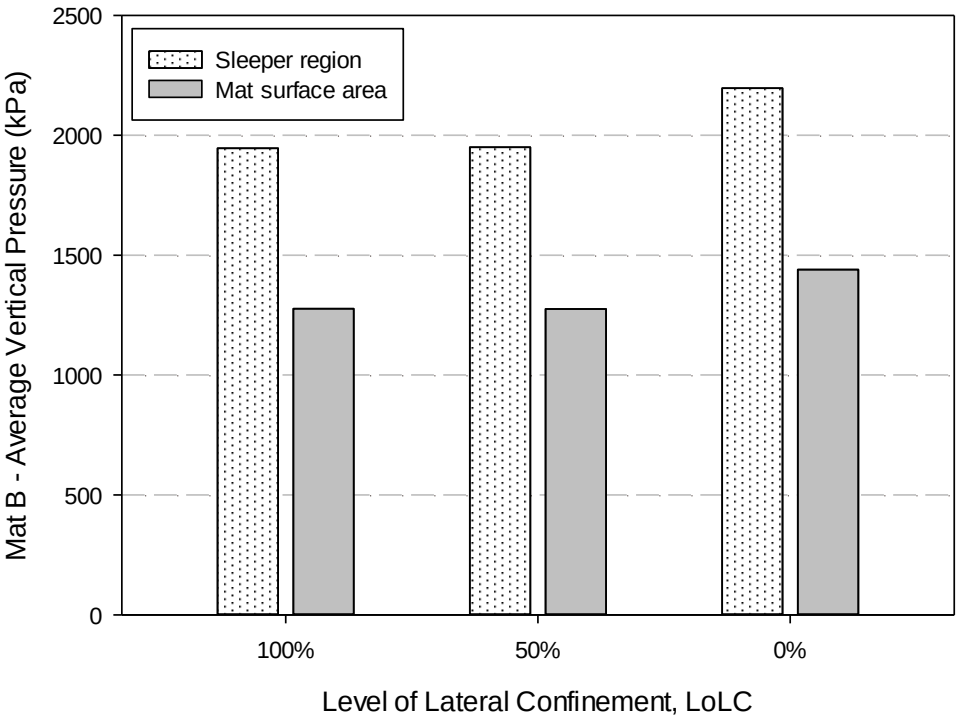

Figure 4-32: Average vertical pressures on Mat A within the sleeper region and over the mat surface area for 100 %, 50 % and 0 % lateral confinements

4.3.3 Comparison of Test Vertical Pressure Values to Vertical Stress Distribution Models

Table 4-8 shows vertical pressures at 300 mm ballast depth from the test conducted as well as from vertical stress distribution models. Mat A and B pressures in Table 4-8 were obtained from the region below the sleeper at 300 mm depth as the vertical stress distribution models predict stresses below the loaded sleeper. However, these pressure values from Mat A and B over predict the stresses at 300 mm ballast depth. The high pressure values on Mat A could be because of the positioning of Mat A directly below the rail seat while low pressures on Mat B represent pressure values towards the midpoint of the sleeper.

As mentioned in Chapter 2, McHenry (2013) assessed the pressures at the ballast-sleeper interface and recorded a conservative average pressure of 9 997 kPa because of the rubber protection. Therefore, since the vertical stress in the ballast layer decreases with depth, the pressure values on Mat A of 3839 kPa and 4801 kPa (for 100 % and 0 % lateral confinements) at 300 mm ballast depth (Table 4-8) seem to be reasonable pressure values – in comparison to 9 997 kPa at the ballast-sleeper interface.

Table 4-8: Vertical pressures at 300 mm ballast depth from test data and vertical stress distribution models

Test Reference / Stress Model	Vertical Pressure (kPa)
Mat A – 100 % LoLC	3839
Mat A – 0 % LoLC	4801
Mat B – 100 % LoLC	1945
Mat B – 50 % LoLC	1950
Mat B – 0 % LoLC	2197
Boussinesq (1885)	330
Clarke (1957)	444
Schramm (1961)	456
Talbot (1919)	680
Horikoshi (JNR)	475
Okabe (1961) – Broken stone ballast	662
Okabe (1961) – Gravel ballast	519

4.3.4 Matrix Based Tactile Surface Sensors: Mat C

Figure 4-33 shows the average maximum lateral pressures for 50 % and 100 % confinement for every 65 000 cycles. Lateral pressures were not recorded for 0 % LoLC. The build-up of lateral

pressures during cyclic loading occurs due to lateral movement and rearrangement of particles in response to the vertical applied stress. Figure 4-34 shows the average lateral pressures on Mat C which were 9.5 kPa and 38 kPa for 50 % and 100 % lateral confinement respectively. The average lateral pressure at 100 % lateral confinement can be compared with findings from previous research conducted under similar boundary conditions. Lackenby et al. (2007) obtained a range of confining pressures between 15 to 65 kPa for a deviator stress of 230 kPa during a cyclic loading triaxial test. In addition, Selig and Waters (1994) recorded fluctuating horizontal pressures of between 20 kPa and 60 kPa in a fully confined ballast box test. These pressures eventually levelled off to 30 kPa. Therefore, the 38 kPa lateral pressure obtained for the fully confined ballast layer in this experiment appears valid.

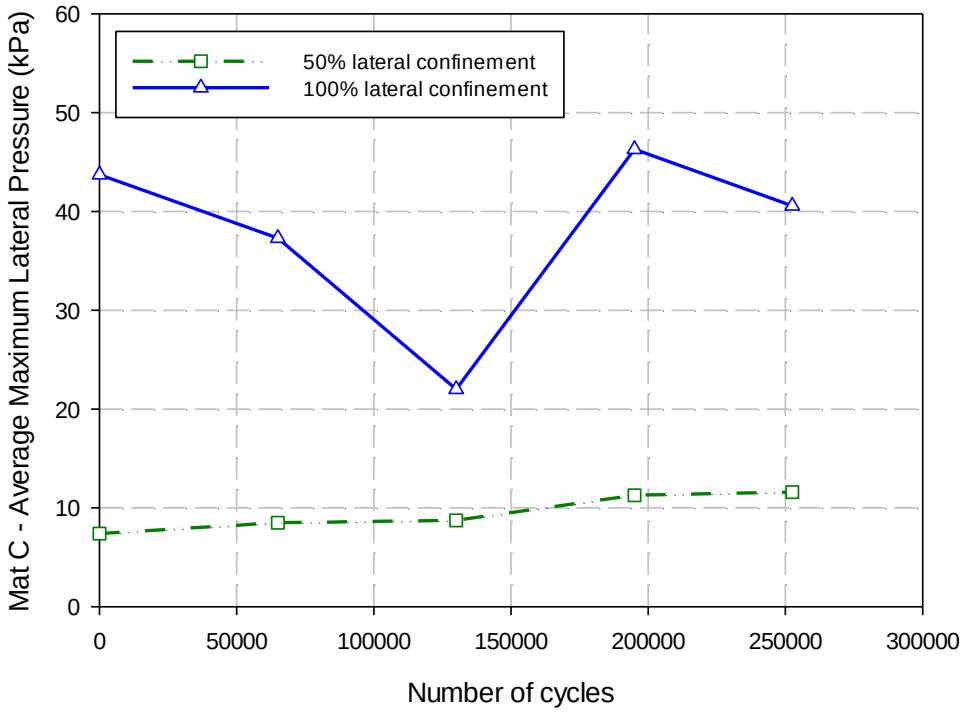

Figure 4-33: Average maximum lateral pressure on Mat C for every 65 000 cycles for 50 % and 100 % confinement

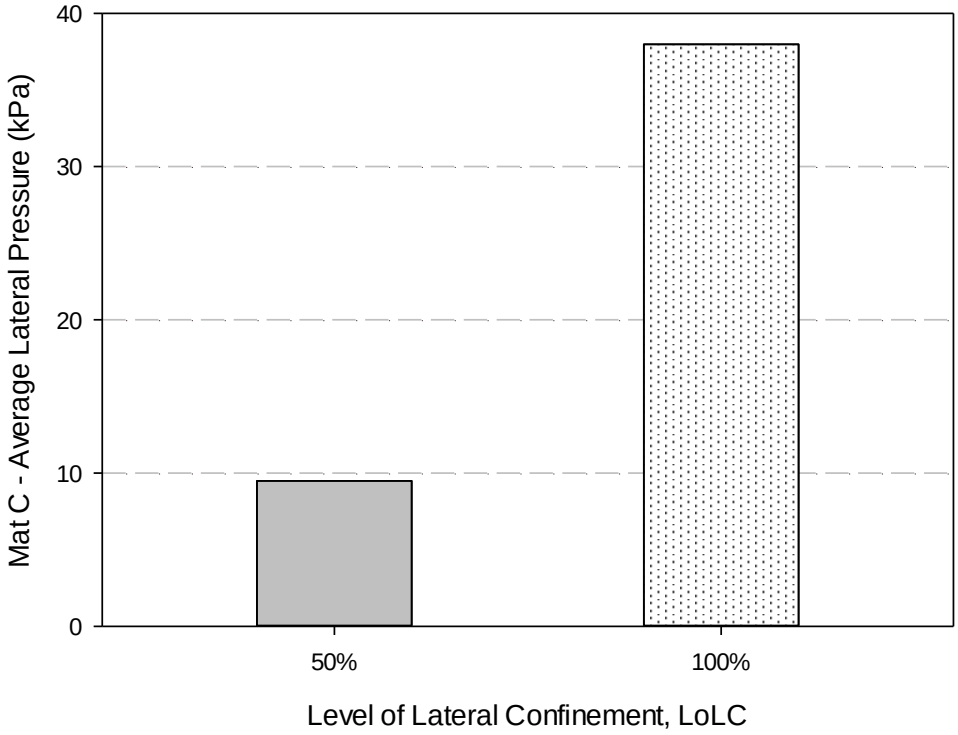

Figure 4-34: Average lateral pressure on Mat C for 50 % and 100 % confinement

5 CONCLUSIONS AND RECOMMENDATONS

This chapter provides a summary of the findings from Chapter 4 and outcomes addressing the objectives of this study outlined in Chapter 1. Recommendations for improvement and further studies on aspects relating to this study are also provided.

5.1 CONCLUSIONS

The following conclusions can be made for each of the study objectives outlined in Chapter 1:

5.1.1 Ballast Compaction

- The likelihood of obtaining ballast samples of equal stiffness that will result in similar deformation response, is small due to particle arrangement, particle sizes and the particle distribution of the ballast sample, irrespective of similar loading parameters used across the different ballast samples.
- However, test samples A and B had similar stiffness values of 108 kPa/mm and 109 kPa/mm respectively along with modulus values of 32 MPa and 33 MPa respectively. Furthermore, Sample C had the highest stiffness response with a ballast stiffness of 169 kPa/mm and modulus of 51 MPa. Sample D had stiffness and modulus values of 155 kPa/mm and 46 MPa, respectively.
- Rapid settlement occurred during the first 10 cycles - which was 41% of the total settlement on average.
- Permanent deformation stabilized (became linear) after the first 100 000 cycles of ballast loading in the laboratory setup.

5.1.2 Comparison of Loading Patterns

- The Field Loading (FL) pattern had more load pulses than the Laboratory Loading (Lab. L) patterns which contributed to increased rates of axial deformation. The rate of strain deformation under the Lab. L was considerably lower than that of the FL pattern. Employing the FL pattern thereafter caused a significant increase in the strain rate due to possible ballast rearrangement or breakage under more load pulses per cycle.
- Although the Laboratory Loading (Lab. L) and Impulse Haversine Loading (IHL) patterns have a single load pulse, there is a notable increase in the rate of axial strain of the IHL pattern compared to that of the Lab. L pattern. This increase in strain rate is

due to an increase in the impulse (loaded area) of the Lab. L pattern as simulated by the IHL pattern.

- The rate of strain accumulation of the Haversine Loading (HL) pattern surpasses the FL strain rate marginally because of the increased loading effects of the second and third load pulses in comparison to their corresponding load pulses in the FL pattern.
- By modifying different aspects of the HL pattern, the Adjusted Haversine Loading (AHL) pattern was developed. This loading pattern was found to be a suitable loading pattern for ballast box testing in the Laboratory based on the rate of strain accumulation. By decreasing the load amplitude of the HL pattern, this loading pattern (AHL) reproduced similar rates of strain compared to the FL pattern considered in this study.

5.1.3 Effect of Rest Periods on Ballast Permanent Settlement

- The permanent settlement of the ballast layer decreased with an increase in the rest period interval between load cycles, and increased with a decrease in the rest period interval.
- Based on the results from this study, by incorporating 0.4 s and 0.8 s rest periods, there was an 83 % and 86 % reduction in settlement following for the FL pattern with no rest period, respectively.

5.1.4 Effect of Boundary Conditions on Permanent Deformation of the Ballast layer

- Decreasing the level of lateral confinement increased the permanent strain of the ballast layer.
- Ballast permanent deformation models of Selig & Waters (1994) (power function) and Sato (1995) accurately predicted the settlement trends of the test data. The variables of the power function also considered the levels of lateral confinement. Deformation models based on log-normal and number of cycles do not consider the levels of lateral confinement.
- Ballast settlement increased by 150 % when the lateral confinement in the ballast box tests were reduced from 100 % to 0 %.

5.1.5 Effect of Boundary Conditions on Particle Breakage

- A fully confined ballast layer prohibited particle breakage to a large extent, while significant ballast breakage occurred in ballast layers with a shoulder profile. Although no ballast breakage is always favourable, ballast breakage is inevitable over time, under heavy haul conditions. Therefore, increasing the lateral confinement of the ballast layer could limit excessive ballast breakage within acceptable levels.
- Ballast breakage indices were useful in quantifying the degree of ballast breakage by identifying changes at sieve size levels. Alternatively, obtaining the difference in total mass before and after cyclic loading provided a broad perspective on the degree of ballast breakage.
- Although the different forms of ballast breakage at each lateral confinement was not identified, common forms of ballast breakage identified include attrition of asperities, corner breakage, particle splitting and particle breakage along weak planes.

5.1.6 Vertical Stress Distribution at the bottom of the ballast layer

- An average vertical pressure of 4801 kPa was experienced at the bottom of the laterally unconfined (0 % lateral confinement) ballast layer as opposed to reduced average vertical pressure of 3838.9 kPa for a 100 % laterally confined ballast layer.
- Vertical pressures obtained in these tests were significantly larger than theoretical and empirical vertical stress distribution models due to the sharp, angular edges of new ballast particles.
- Lateral pressures of 9.5 kPa and 38 kPa for 50 % and 100 % lateral confinement were recorded. The lateral pressure for a 100 % lateral confinement fell within the lateral pressure range of 15 to 65 kPa mentioned in the literature.

5.2 RECOMMENDATIONS

Recommendations and suggestions to the railway industry and for further study are outlined in this section.

5.2.1 Development of an advanced Materials Testing System (MTS)

Although a suitable loading pattern was developed and recommended in this study, MTS machines capable of simulating complex train loading patterns with various preference options such as choosing from various loading patterns, customizing these loading patterns according

to type of locomotive, type of wagon, wheel spacing and other options, can be manufactured to promote accurate and realistic laboratory testing. Furthermore, MTS features can be modified to easily perform complex loading patterns at high frequencies where necessary.

5.2.2 Practical applications to achieve adequate ballast layer lateral confinement

The following practical applications could be implemented to limit the permanent settlement and ballast deterioration of ballasted tracks:

- Geosynthetic ballast layer reinforcement, such as geocells placed at the bottom of the ballast layer, could increase the level of lateral confinement.
- Placing intermittent lateral restraints at various track sections could increase the level of lateral confinement.
- Increasing the volume of ballast at the ballast shoulder will increase the level of lateral confinement, hence, decreasing the slope of the ballast shoulder.

5.2.3 Recommendations for further study

Further studies and investigations can be conducted in the following areas:

- Development of suitable loading patterns to simulate alternative locomotive or wagon wheel configurations in the laboratory.
- Investigation into suitable loading patterns for subgrade materials. Loading patterns for consideration would include haversine or trapezoidal loading patterns.
- Further studies on rest periods to identify the appropriate rest period duration for different track loading parameters.
- Investigate alternative methods of implementing lateral restraints at various track sections.

6 REFERENCES

Abadi, T. et al. (2016) Improving the performance of railway track through ballast interventions. *Proceedings of the Institution of Mechanical Engineers, Part F: Journal of Rail and Rapid Transit*, 1-17.

Al-Saoudi, N.K. and Hassan, K.H. (2014) Behaviour of track ballast under repeated loading, *Geotechnical and Geological Engineering*, Vol. 32, No. 1, pp. 167-178.

Alva-Hurtado, J. E. & Selig, E. T. (1981). Permanent strain behaviour of railroad ballast. Proceedings of the International Conference on Soil Mechanics and Foundation Engineering Vol 1, 543 – 546.

AREMA. (2012). Manual for Railway Engineering. *American Railway Engineering and Maintenance of Way Association*, Lanham, MD.

Aursudkij, B., McDowell, G. R., & Collop, A. C. (2009). Cyclic loading of railway ballast under triaxial conditions and in a railway test facility. *Granular Matter*, *11*(6), 391-401.

Awoleye, E. O. A. (1993). Ballast type - ballast life predictions. Derby, *British rail research* LR CES 122, October 1993.

Barksdale, R. D. (1972). Laboratory evaluation of rutting in base course materials. *3rd International Conference on the Structural Design of Asphalt Pavements, Vol. 1*, London, England

Bennett, K. C., Ho, C. L., and Nguyen, H. Q. (2011). Verification of box test model and calibration of finite element model. Transportation Research Record 2261, Transportation Research Board, Washington, DC, pp. 171-177.

Boussinesq, J. (1885) Application des Potentiele a l'Etude de l'Equilibre et du Mouvement des Solides Elastiques. *Gautheir-Villars*. Paris, France.

Cedergren, H.R. (1989), *Seepage, drainage, and flow nets*, 3rd Edition edn, John Wiley & Sons, New York.

Clarke, C. W. (1957). Track loading fundamentals. *The Railway Gazette*. Part 1, pp. 45-48, part 2, pp. 103 – 107.

Doyle, N.F. (1980), Railway track design: a review of current practice, *Issue 35 of Occasional paper, Australia Bureau of Transport Economics Research report (Melbourne Research Laboratories)*, Australian Government Publishing Service, Canberra, 1980

Ebrahimi, A., Tinjum, J.M., and Edil, T.B. (2012). Protocol for Testing Fouled Railway Ballast in Large-Scale Cyclic Triaxial Equipment. Geotechnical Testing Journal, Vol. 35, No. 5.

Eisenman, J., (1970) Stress Distribution in the Permanent Way due to Heavy Axle Loads and High Speeds, *AREA Proceedings*, Vol. 71, 24-59.

Eisenmann, J. (1972), Germans gain a better understanding of track structure, *Railway Gazette International*, Vol. 128, No. 8, pp. 305.

Esveld, C. (2001). Modern Railway Track. *MRT-Productions*, Zaltbommel, the Netherlands.

Fredrick, C. O. and Newton, S. G. (1977). The relationship between traffic and track damage – The effect of vertical loads. *Technical Note TN.T2, British Broad Research and Development Division*, London.

Fröhling, R. D. (1995). Measurement, interpretation and classification of South Africa track geometry. Interaction of railway vehicles with the track and its substructures. *International Journal of Vehicle Mechanics and Mobility*, Volume 24. Swets and Zeitlinger Publisher, Prague.

Gräbe, P. J. (2001). "Resilient and permanent deformation of railway foundations under principal stress rotation." Ph.D. thesis, Univ. of Southampton, Southampton, U.K

Gräbe, P. J., and Clayton, C. R. (2009). Effects of principal stress rotation on permanent deformation in rail track foundations. *Journal of Geotechnical and Geoenvironmental Engineering*, *135*(4), 555-565.

Gräbe, P. J., and Clayton, C. R. I. (2003). "Permanent deformation of railway foundations under heavy axle loading." Proc., Int. Heavy Haul Association (IHHA), IHHA, Virginia Beach, VA, 3.25–3.32

Gräbe, P. J., and Clayton, C. R. I. (2013). Effects of principal stress rotation on resilient behavior in rail track foundations. *Journal of Geotechnical and Geoenvironmental Engineering*, *140*(2), 04013010.

Gräbe, P. J., Clayton, C. R. I., and Shaw, F. J. (2005). Deformation measurement on a heavy haul track formation. *Proceedings of the 8th international Heavy Haul Conference*, International Heavy Haul Association, Rio de Janeiro, Brazil, 287-295.

Han, X. (2012). The role of particle breakage on the permanent deformation of ballast, Master of Engineering – Research thesis, Department of Civil, Mining and Environmental Engineering, University of Wollongong.

Han, X., and Selig, E. T. (1997). Effects of fouling on ballast settlement. *Proceedings of the 6th International Heavy Haul Railway Conference*, Cape Town, South Africa, pp. 257-268

Hardin, B.O. (1985) Crushing of soil particles. *Journal of Geotechnical Engineering, ASCE*, Vol. 111, No. 10, 1177–1192.

Hettler, A. (1984) Bleibende Setzungen des Schotteroberbaus. *Eisenbahn-technische Rundschau (ETR), Vol. 33*(11), 847-853.

Huang Y.H. (1993), Pavement analysis and design. *Prentice-Hall Inc.*, Englewood Cliffs

Huang, H., Shen, S., and Tutumluer, E. (2009) Sandwich model to evaluate railroad asphalt trackbed performance under moving loads. *Transportation Research Record,* 2117: 57-65

Indraratna, B. and Ionescu, D.J. (2000). State of the art large scale testing of ballast. Railway Technical Society of Australasia (eds), CORE 2000 Railway Technology for the 21st Century, pp. 24.1-24.3, Australia: Railway Technical Society of Australasia.

Indraratna, B., Khabbaz, H., Salim, W., & Christie, D. (2006). Geotechnical Properties of Ballast and the Role of Geosynthetics. *Journal of Ground Improvement, 10(3),* 2006, 91-102.

Indraratna, B., Lackenby, J., and Christie, D. (2005) Effect of Confining Pressure on the Degradation of Ballast under Cyclic Loading. *Geotechnique*, Institution of Civil Engineers, UK, Vol. 55, No. 4, pp. 325-328.

Indraratna, B., Salim, W. & Rujikiatkamjorn, C. (2011) *Advanced rail geotechnology–ballasted track,* CRC press.

Indraratna, B., Thakur, P. K. & Vinod, J. S. (2010a). Experimental and numerical study of railway ballast behaviour under cyclic loading. *International Journal of Geomechanics, Vol. 10,* No.4

Ionescu, D., (2004). *Evaluation of the engineering behaviour of railway ballast*, Doctor of Philosophy Thesis, Faculty of Engineering, University of Wollongong.

IRR Iraq Railway Company (2000) Ballast Specification

Ishikawa, T., Sekine, E., and Miura, S. (2011). Cyclic deformation of granular material subjected to moving-wheel loads. *Canadian Geotechnical Journal,* 48(5): 691-703.

Jeffs, T. and Tew, G.P. (1991), A review of track design procedures, Vol. 2, Sleepers and Ballast, *Railways of Australia*.

Klassen, M., Clifton, A. and Watters, B. (1987) *Track evaluation and ballast performance specifications.*

Knutson, R. M. (1976). Factors influencing the repeated load behaviour of railway ballast. PhD Dissertation, University of Illinois at Urbana-Champaign.

Kashani, H. F., Hyslip, J. P., & Ho, C. L. (2017). Laboratory evaluation of railroad ballast behavior under heavy axle load and high traffic conditions. *Transportation Geotechnics*, *11*, 69-81.

Lackenby, J., Indraratna, B and McDowel, G. (2007) The Role of Confining Pressure on Cyclic Triaxial Behaviour of Ballast. Geotechnique, Institution of Civil Engineers, UK Vol. 57, No. 6, pp. 527-536.

Lade, P.V., Yamamuro, J.A. and Bopp, P.A. (1996) Significance of particle crushing in granular materials. *Journal of Geotechnical Engineering, ASCE,* Vol. 122, No. 4, pp. 309–316.

Lee, K. L. and Farhoomand, I. (1967) Compressibility and crushing of granular soil in anisotropic triaxial compression. *Canadian Geotechnical Journal, Vol. 4*, No. 1, pp.69-86.

Lekarp, F., & Dawson, A. (1998). Modelling permanent deformation behaviour of unbound granular materials. *Construction and building materials, 12*(1), 9-18.

Lekarp, L., Isacsson, U., and Dawson, A. (2000) State of the Art. II: Permanent Strain Response of Unbound Aggregates. *Journal of Transportation Engineering*, 126(1), 76-83

Li, D. (1994). Railway Track Granular Layer Thickness Design Based on Subgrade Performance under Repeated Loading. *PhD dissertation, Department of Civil Engineering, University of Massachusetts*, Amherst, MA

Li, D., & Selig, E. T. (1996). Cumulative plastic deformation for fine-grained subgrade soils. *Journal of geotechnical engineering*, *122*(12), 1006-1013.

Li, D., Hyslip, J., Sussmann, T., Chrismer, S., (2015), Railway geotechnics, *CRC Press/Spon Press*, Boca Raton, Fla. [u.a.

Li, S. (2012), Railway sleeper modelling with deterministic and non-deterministic support conditions, Masters Degree Project, Department of Transport Science, Royal Institute of Technology, Stockholm.

Lim, W. L. (2004). Mechanics of railway ballast behaviour. *PhD Thesis*, University of Nottingham.

Liu, J. and Xiao, J. (2010) Experimental study on the stability of railroad silt subgrade with increasing train speed, *Journal of Geotechnical and Geoenvironmental Engineering*, Vol. 136, No. 6

Marsal, R. J. (1967) Large scale testing of rockfill materials. *Journal of the Soil Mechanics and Foundations Division, ASCE, Vol. 93*, No. SM2, pp. 27-43.

McDowell, G. & Bolton, M. (1998) On the micromechanics of crushable aggregates, *Géotechnique*, vol. 48, no. 5, pp. 667-679.

McDowell, G., Bolton, M. and Robertson, D. (1996) The fractal crushing of granular materials, *Journal of the Mechanics and Physics of Solids* 44(12), 2079–2101.

McHenry, M. T. (2013). Pressure measurement at the ballast-tie interface of railroad track using matrix based tactile surface sensors. *Theses and Dissertations – Civil Engineering*, 15.

Michas, G. (2012), Slab track systems for high-speed railways, *Master's thesis, Royal Institute of Technology*, Stockholm. Department of Transport Science.

Miura, N. and O-hara, S. (1979) Particle crushing of decomposed granite soil under shear stresses. *Soils and Foundations, Vol. 19*, No. 3, pp. 1-14.

Okabe, Z. (1961) Laboratory Investigation of Railroad Ballast, *Japan Railway Civil Engineering Association*, Permanent Way No. 13.

ORE (1987). The dynamic effects due to increasing axle loads from 20 to 22.5 ton. *Report D161-RP4*. Office of Research and Experiments (ORE), International Union of Railways, Utrecht, the Netherlands.

Panuccio, C. M., Wayne, R. C., and E. T. Selig (1978). Investigation of a plate index test for railroad ballast, *Geotechnical Testing Journal, American Society for Testing and Materials (ASTM)*, Vol. 1, No. 4, 213–222.

Powrie, W., & Priest, J. (2011). Behaviour of ballasted track during high speed train passage. *High Speed Track Railways Day, Institution of Civil Engineers*, One Great George Street, London.

Powrie, W., Yang, L. A., & Clayton, C. R. (2007). Stress changes in the ground below ballasted railway track during train passage. *Proceedings of the Institution of Mechanical Engineers, Part F: Journal of Rail and Rapid Transit*, *221*(2), 247-262.

Priest, J.A., Powrie, W., Yang, L., Gräbe, P.J., and Clayton, C.R.I. (2010) Measurements of transient ground movements below a ballasted railway line, *Géotechnique* 60(9):667-677.

Profillidis, V. A. (2000). *Railway Engineering*. Aldershot: Ashgate Publishing Limited.

Qian, Y., Tutumluer, E., and Huang, H. (2011). Ballast vibrations and deformations due to different train loading scenarios studied using the discrete element method. *Advances in Environmental Vibration - Proceedings of the 5th International Symposium on Environmental Vibration, ISEV 2011* (pp. 613-619).

Razouki, S. S., and Schanz, T. (2011) One-dimensional consolidation under haversine repeated loading with rest period. *Acta Geotechnica*, *6*(1), 13-20.

RT/CE (2000) Railtrack line specification, RT/CE/S/006 issue 3. Track ballast.

Sadeghi, J.M and Shoja, H. (2012) Impact of superelevation deficiencies on the loading pattern of railway sleepers, *Proceedings from Institute of Mechanical Engineers, Part F: Journal of Rail and Rapid Transit*, 227(3) 286-295.

Sadeghi, J.M. (2008). Experimental evaluation of accuracy of current practices in analysis and design of railway track sleepers, *Canadian Journal of Civil Engineering*, 35:881-893.

Sadeghi, J.M. and Yoldashkhan, M. (2005). Investigation on the accuracy of current practices in analysis of railway track sleepers. *International Journal of Civil Engineering*, 3(1): 34-51.

Saxena, S.C. and Arora, S. P. (2004). A text book of railway engineering. *Dhanpat Rai Publications (p) Ltd*., New Delhi.

Schramm, G. (1961) Permanent Way Technique and Permanent Way Economy, *Otto Elsner Verlagsgesellschaft Darmstadt*.

Selig, E.T. & Waters, J.M. (1994) Track geotechnology and substructure management, *Thomas Telford,* London.

Shahin, M. A., Indraratna, B. & Salim, W. (2007) Stabilisation of granular media and formation soil using geosynthetics with special reference to railway engineering', *Proceedings of the ICE - Ground Improvement 11*(1), 27–43.

Shenton, M. J. (1984) Ballast Deformation and Track Deterioration. *Track Technology*. London: Thomas Telford Ltd.

Shenton, M.J. (1978) Deformation of railway ballast under repeated loading conditions. *Railroad Track Mechanics and Technology. Symposium Proceedings*, Princeton University, pp. 387–404.

Shi, X. (2009) Prediction of permanent deformation in railway track, *University of Nottingham*.

Spoornet (1998), S406 (1998) Specification for the supply of stone, Technical report, Spoornet.

Spoornet (2006), S410 (2006) Specification for Railway Earthworks, Technical report, Spoornet

Stewart, H.E. (1986) Permanent strains from cyclic variable amplitude loadings. *Journal of Geotechnical Engineering, ASCE,* Vol. 112, No. 6, pp. 646–660.

Suiker, A.S.J. (2002) The mechanical behaviour of ballasted railway tracks. *PhD Thesis, Delft University of Technology*, The Netherlands.

Sun, Q. D., Indraratna, B., and Nimbalkar, S. (2014) Effect of cyclic loading frequency on the permanent deformation and degradation of railway ballast. *Géotechnique, 64*(9), 746-751.

Sun, Q., Indraratna, B., and Nimbalkar, S. (2016). An elasto-plastic method for analysing the deformation of the railway ballast. *Procedia Engineering, Vol. 143,* 954-960.

Sussmann, T.R., Kish, A., and M. J. Trosino (2003). Investigation of the influence of track maintenance on the lateral resistance of concrete tie track, *Journal of the Transportation Research Board, Transportation Research Record 1825*, Railroad Research: Intercity Passenger Transportation, Track Design and Maintenance, and Hazardous Materials Transport, Washington, DC, pp. 56–63.

Talbot, A.N. et al. (1919) Stresses in Railroad Track, Report of the Special Committee to Report on Stresses in Railroad Track; *Second Progress Report, AREA Proceedings,* Vol. 21, 645-814.

Talbot, A.N. et al. (1933) Stresses in Railroad Track, Report of the Special Committee to Report on Stresses in Railroad Track; *Sixth Progress Report, AREA Proceedings*, Vol. 45, 66 – 848.

Technical Methods for Highways (1986). Standard methods of testing road construction materals (TMH 1), Pretoria: National Institute for Transport and Road Research.

Tennakoon, N., Indraratna, B. & Nimbalkar, S. (2014). Impact of ballast fouling on rail tracks. Second International Conference on Railway Technology: Research, Development and Maintenance (pp. 1-11).

Transnet Freight Rail (TFR) 1998. S406 - *Specification for the supply of stone.* Johannesburg: TFR.

Transnet Freight Rail (TFR) 2012. Manual for Track Maintenance, *Infrastructure Engineering*, Transnet.

Tutumluer, E., Qian, Y., Hashash, Y. M. A., Ghaboussi, J., and Davis, D. D. (2011) Field validated discrete element model for railroad ballast. *Proceedings of the Annual Conference of the American Railway Engineering and Maintenance-of-Way Association*, pp. 18-21.

UIC (2004a). Technical specification for the supply track support and classification of line-resulting load limit for wagons. *Union Internationale des Chemins de Fer (UIC)*, Paris, France. Leaflet No. 700.

Yang, L. A., Powrie, W., and Priest, J. A. (2009). Dynamic stress analysis of a ballasted railway track bed during train passage. *Journal of Geotechnical and Geoenvironmental Engineering*, *135*(5), 680-689.

Yoo, T. S., Chen, H., and Selig, E., (1978). Railroad ballast density measurements, *Geotechnical Testing Journal, American Society for Testing and Materials (ASTM)*, Vol. 1, No. 1, 41–54.

Zakeri, J. and Sadeghi, J. (2007) Field investigation on load distribution and deflection of railway track sleepers, *Journal of Mechanical Science and Technology*, 21, pp 1948-1956.